Modeling of Everted Tubes for Medical Applications

Andrew Lewis

A dissertation
submitted in partial fulfillment of the
requirements for the degree of

Doctor of Philosophy

University of Washington

2024

Reading Committee:
Blake Hannaford, Chair
Eric J. Seibel
Sawyer Fuller
Anne Goodchild, GSR

Program Authorized to Offer Degree:
Mechanical Engineering

University of Washington

Abstract

Modeling of Everted Tubes for Medical Applications

Andrew Lewis

Chair of the Supervisory Committee:
Professor Blake Hannaford
Electrical and Computer Engineering

Everting tube robots are a type of growing soft robot that easily navigate arbitrary and constricted environments. Since they grow from the tip, everting tube robots are also called vine robots, and this tip-wise growth means that the body of the robot does not slide against the environment during growth. Since they can grow into constricted areas without sliding, they are very promising as for medical applications where they can gain access to the body through natural orifices, which can often be sensitive to sliding and may require extensive expertise to access with traditional methods. This dissertation investigates two major challenges encountered during the design of everting tube robots and details the design process of an everting tube robot for emergency scenarios. Chapter one introduces a simple mechanism for improving the estimation accuracy of dynamic tube growth. The second chapter proposes a method for understanding the friction forces between an everting tube and a tool placed through its central channel, such as a flexible endoscope. The final chapter delves into the development of an everting Emergency Airway Device (EAD). This devices leverages me-

chanical intelligence to allow for minimally trained bystanders to establish an airway, which is critical for survival in emergencies like cardiac arrest and trauma.

TABLE OF CONTENTS

Page

List of Figures iii

List of Tables xi

Chapter 1: Introduction 1
1.1 Motivation 1
1.2 Dissertation Focus 3
1.3 Literature Review 4
1.4 Case Study: Application of Everting Tubes for Teleoperation of Medical Robots 10
1.5 Summary 15

Chapter 2: Using Friction to Improve Growth Estimation of Reel-Mounted Everting Robots 16
2.1 Introduction 16
2.2 Experimental System 20
2.3 Physical Characterization 24
2.4 Position Sensing 30
2.5 Reel-Based Estimation Experiment Methods 36
2.6 Reel-Based Estimation Results 39
2.7 Discussion 43
2.8 Conclusion 51

Chapter 3: Characterizing an Everting Tube's Working Channel Friction 53
3.1 Introduction 53
3.2 Methods 60
3.3 Experiment Model 67
3.4 Experiments 71

3.5 Experimental Results 79
3.6 Discussion 87
3.7 Future Work 90
3.8 Conclusion 90

Chapter 4: Design Evolution of an Emergency Airway Device 92
4.1 Introduction 92
4.2 Device Concept 97
4.3 Prototype EAD-1 100
4.4 Prototype EAD-2 105
4.5 Prototype EAD-3 112
4.6 Discussion 119
4.7 Conclusion 123

Chapter 5: Conclusion 124
5.1 Published Work 125

Appendix A: Pressure Control Circuit and Software 147
A.1 Pressure Control Circuit 147
A.2 Pressure Increment Code 149
A.3 Autonomous Eversion State Machine Code 156

LIST OF FIGURES

Figure Number — Page

1.1 The eversion process uses pressure within an inelastic tube to pull new material from a reel so that the inflated tube grows at the tip. Note that once the material (purple shapes) has been pulled to the outside, that section of material remains in place. . . . 2

1.2 A proposed method for classifying the ways that the bodies of everting tube robots are stored prior to growth. . . . 8

1.3 A flexible cystoscopy procedure being performed on a male (left) and female (right). The screens at the top show the video feed from the tip of the endoscope and are showing a bladder tumor. Note that the male urethra is much longer and more curved than the female urethra. The male urethra also passes through the prostate, which can be enlarged, especially in older patients. (Image ©the Mayo Clinic) . . . 12

1.4 The TelCys platform designed to allow safe teleoperation of routine urological diagnostic exams. *Left*: A - The flexible cystoscope control module, B - the linear everting tube control module, and C - the flexible cystoscope tip within the everting tube introducer. *Right*: A nurse supervising the deployed TelCys robot. . . . 14

2.1 Slack between the tip of an everted tube and its material reel will cause inaccurate estimations of tube tip position from an encoder at the reel. ***Top***: When the growing tube's velocity, v, matches the linear velocity of its material reel, ωr, the material remains taut and there is a predictable relationship between reel angle and tube tip position. ***Center***: When the tube growth slows down, inertia of the reel will cause extra material to unroll, causing a discrepancy between the reel position and tube tip position. ***Bottom***: Friction torque on the reel, τ_f, will slow growth while preventing over-spin, making tube tip position more predictable during dynamic growth. . . . 17

2.2 Nine eversion growth trajectories from 3 tubes under similar conditions as measured by Time of Flight (ToF) position sensor. ***Top***: Position of tube tip during growth. ***Bottom***: Tube tip velocity. . . . 19

2.3 The eversion system used for these experiments. ***Top***: A Time of Flight sensor mounted to the left end of a clear growth pipe measures the tip position of the everting tube during its growth from the everter base on the right. ***Bottom***: A white PTFE plumbers tape ribbon (indicated by arrow) within the LDPE everting tube increases the accuracy of the Time of Flight sensor, as described in section 2.4. 21

2.4 ***Left***: The eversion system with an LDPE tube everting into a clear pipe. **A** - 3" (75mm) polycarbonate pressure vessel. **B** - "Eversion snout" where the everting material is sealed to the pressure vessel. **C** - Guide funnel leading into the clear polycarbonate pipe. **D** - 1/4" (6mm) pneumatic pressure inlet. **E** - Gripper plug end cap for quick access. ***Right***: CAD of the removable eversion reel mechanism. The stainless steel axle is supported by ball bearings. **I** - Differential quadrature encoder. **II** - Eversion reel with removable piece (red) for clamp ing the end of the eversion material. **III** - Friction drum. **VI** Torsion spring pressing against the groove in the friction drum. **IV** - Winder knob aids rewinding the eversion material between trials. **V** - The inertia wheel increases the rotational inertia of the reel. 22

2.5 Reel acceleration experiment. ***Left***: Hardware setup for reel acceleration experiment. ***Right Top***: Free body diagram of acceleration experiment showing the gravity force (mg) at the reel radius (r), reel inertia torque ($I\alpha$), and reel friction torque (τ_f). ***Right Bottom***: Velocity of dropping mass recorded during high inertia drops with average linear fit compared to acceleration due to gravity. 26

2.6 ***Left***: Medium Friction configuration with PLA friction pad held against steel axle. ***Right***: High Friction configuration with bare arm of spring held against PLA friction drum. The low friction configuration, not shown, removed the spring from the assembly. 27

2.7 Tube adjunct testing. ***Left Top***: Diagram of everting tube with adjunct growing towards Time of Flight sensor (**i**) inside rigid growth pipe (**ii**). (**iii**) - Tube adjunct material. (**iv**) - Grounding point for tube material and adjunct. (**v**) - Tube material. ***Left Bottom***: A pink string everted within an LDPE tube to test improvements of ToF position sensing. The ground truth inch scale can be seen drawn on the polycarbonate pipe. ***Right***: Quadratic fit errors for combined trials compared between plain tubes, tubes that have been crumpled before mounting, and tubes that have added materials to improve reflectivity. 33

2.8 ***Left***: RMS Error of group fits compared to the presence of PTFE and the order within each set of trials (p=0.0065). The intersections of the trends of the medians indicate interaction. ***Right***: RMS Error of group fits with no PTFE and with PTFE (p=0.0001). 35

2.9 Sensor data from each test showing position and temporal difference between ToF- and reel-based estimation for better-than-average trials. The RMS position errors for the trials shown are: 36.5, 17.3, and 19 mm. The velocity RMSE values are: 108.1, 69.6, and 59.4 mm/sec. 40

2.10 Test 1 (increasing reel inertia with low friction) error and growth results with statistical significance. 41

2.11 Error metric results for tests 2 & 3 - increasing friction with high and low reel inertia. 41

2.12 Average velocity growth metric results for tests 2 & 3 - increasing friction with high and low reel inertia. Results for the remaining growth metrics are similar to the velocity results. 42

3.1 Components of the general friction model. This illustration ignores the Stribeck effect, which models a smooth transition from static to Coulomb (dynamic) friction. 59

3.2 Comparison of linear eversion robot with working channel and the experimental setup. ***Above***: A simple linear eversion robot where the central working channel is fed forward at half the rate as the everting tube material. This disparity in velocity causes sliding of the tube material along the working channel. ***Below***: In the experimental setup, the working channel is mounted to a force sensor in order to measure the interaction forces. This setup allows for observation of the overlap length, l_o. 61

3.3 Schematic of the eversion robot and data collection system. 63

3.4 Force sensing end of experimental setup. Seen in the foreground (left to right) are the high pressure source gauge, digital pressure regulator, eversion system gauge, and the on/off valve. In the middle ground is the force sensor with $\frac{1}{4}$ inch (6 mm) steel working channel inserted into the growing tunnel. 64

3.5 State transition diagram for automated growth behavior. 66

3.6 Free body diagrams of the abstracted experiment system at zero velocity. ***Top***: The full experimental system, including the force at the front of the tube, the pressure-dependent P-block sliding along the working channel, and the E-block that represents the force required to evert the tube under normal growth. ***Middle***: A diagram of the P-block showing the forces acting on the working channel section of the tubing at the moment when the limit of static friction is reached. F_E is the sum of eversion forces acting on the E-block. ***Bottom***: The forces acting along the working channel by the everting tube. 68

3.7 Close-up of growth stopper and everting tube growing over working channel. ***Above***: Growth stopper mounted to force sensor. This stops the growth of the everting tube at a repeatable location for every trial. ***Below***: The working channel after it has been inserted into the central lumen of the everting tube. 74

3.8 Characteristic static friction trial. This trial is a 1/4" working channel without lubrication. The shaded area is the swapping phase between initial growth and growth over the working channel. The position data are relative to the tip of the working channel, thus representing overlap length. The second position graph from the top is a magnification of the overlap growth phase of the experiment. This trial required 2 pressure increments to evert to the stopping block. During the 3rd phase, the pressure just before each drop to nominal pressure (1 psi) is the pressure that was able to initiate growth. This pressure was held until movement stopped. 75

3.9 Characteristic dynamic friction trial. This trial is a 1/4" working channel without lubrication. The shaded area is the swapping phase between initial growth and growth over the working channel. The position data are relative to the tip of the working channel, thus representing overlap length. The second position graph from the top is a magnification of the overlap growth phase of the experiment. 78

3.10 Force required to initiate eversion growth across three trials of one tube with automated pressure increments. ***Top***: Eversion force data and linear fits for each trial and a fit for all data. ***Bottom***: Residual distribution for each trial's fit and the residuals of all data from the overall fit. 80

3.11 Comparison of all measured minimum eversion forces and the minimum eversion forces calculated from static friction threshold data. 81

3.12 Comparison of calculated coefficients of static friction by method of estimating minimum eversion force. This data only includes tests with 1/4" working channel. 82

3.13 Static friction results. ***Top***: Threshold pressure per tube overlap over a working channel for working channels of different radii and with the presence of lubrication. ***Bottom***: The distribution of calculated coefficients of static friction. 83

3.14 Coulomb friction results. ***Top***: Calculated coefficient of Coulomb friction over the length of each trial with dry and lubricated working channel. ***Middle***: Distribution of Coulomb coefficients. ***Bottom***: Instantaneous Coulomb coefficients with their corresponding instantaneous velocity. 85

3.15 Maximum length achieved during dynamic friction trials with and without lubrication. 85

3.16 Comparison of static and dynamic coefficients of friction with and without lubricant. 86

3.17 Theoretical maximum length for a working channel within a 1 inch (25.4 mm) diameter everting tube in the tested experimental setup. This model assumes a minimum eversion force of 2N, which was shown to be roughly the force required to evert at the distal working channel in this setup. 87

4.1 Everting Airway Device deployment concept. *Left*: Select anatomy of the airway: (**A**)- soft palate, (**B**)- uvula, (**C**)- oropharynx, (**D**)- hypopharynx, (**E**)- esophagus, (**F**)- trachea, (**G**)- larynx, (**H**)- epiglottis, and (**I**)- tongue. *Center*: Tracheal deployment of the Airway Device. Air pressure within the device (**J**) has grown the tube through the throat and deployed the *distal sealing cuff* (**K**). Once the device tip is deployed into the trachea at (**L**), the distal cuff inflates to allow for breathing air from the *central air line* (**M**) to inflate the lungs (**N**). *Right*: In the case of esophageal deployment, the distal cuff and the *proximal sealing cuff* (**O**) are inflated before providing breathing air through the *side air line* (**Q**). 93

4.2 *Left*: Commercial Airway Management Trainer from Laerdal Medical (Norway). *Right*: Advanced Joint Airway Management System (AJAMS) components from the University of Washington. 96

4.3 Eversion process for tracheal deployment. *Above*: An example of eversion growth from left to right. Pressure (**P**) within the base of the device causes material from the reel to travel to the front and evert to the outside of the growing tube. *Left*: The airway device has grown into the mouth. The proximal sealing cuff (**R**) is still within the device body and will be everted from the growing tip (**S**) before the end of the side air channel, which will remain on the outside of the device body (**T**) for possible connection to the breathing circuit. All of the everting body material passes from the pressurized device vessel at the exit point (**U**). *Center*: The proximal sealing cuff has been everted (**V**) and the end of the side air channel is about to evert. *Right*: The tube has grown into the trachea and everted the distal sealing cuff while the central air channel is about to evert (**W**). 99

4.4 *Above*: Deployment of EAD-1. (**A**) Tube in trachea. (**B**) Tube in esophagus. *Below*: Motor controlled rotary eversion assembly with rotary union for external access to internal lumen. The spindle is mounted on bearings and also referred to as a reel. 101

4.5 Scaled (2X) airway phantom with key anatomical areas highlighted. Hollow pockets in the silicone are included to simulate highly compliant areas of soft palate and tongue. A hinged flap simulates the epiglottis that covers the trachea during eating and drinking. 103

4.6 Free eversion and seal evaluation of EAD-1 within a clear, rigid tube. *Above*: Schematic of EAD-1 evaluation. *Below*: Clear rigid tube with EAD-1 deployed. The red tubes within the clear tube are the central and side breathing air channels. For EAD-2 testing, breathing pressure was introduced through the pressure transducer connections. 105

4.7 Sealing pressure of balloon configurations. Vertical bars indicate key mucosal pressure thresholds: **A**- optimal cuff pressure[92]; **B**- tracheal capillary perfusion pressures[95]; **C**- mucosal pressure at which pharyngeal capillaries collapse-[92]; **D**- advisable cuff pressure for LMA/ILMA-; and **E**- mucosal pressure at which pharyngeal mucosal perfusion stops, the patient is now at risk of ischemia. Horizontal lines represent performance of manual devices[90, 96]. **I**- peak AWP supplied by Bag-Valve-Mask. **II**- peak Airway Pressure (AWP) supplied through a ventilator. 106

4.8 Representative time series pressure data of an everting tube. **A**- tube pressurizing (L = 0). **B**- static friction in spindle (L = 0), **C**- eversion begins, tube lengthens at constant pressure. **D**- tube is fully deployed and re-pressurizes to set point. 106

4.9 Tube construction methods. (***i***): Example fin seal (left) and lap seal (right). (***ii***): Front and side views of 3-piece sealing cuff. Each section is an identical circle. The material at the center opening is lap sealed to the main tube body, as seen in ***v***. (***iii***): Heated roller sealing of a lap seal. TPU is wrapped around an insulated core of parchment paper and silicone rubber (purple). The heated roller (black) is rolled along the length of the seal. (***iv***): Configuration 3 with thin TPU and lap seal. (***v***): Configuration 5 with thicker TPU body and thin TPU cuffs. The body sections are connected with narrow material to prevent elongation of the body during cuff inflation. (This paper considers Config. 6 with thin TPU body and cuffs.) 108

4.10 Bisected, patient-specific airway phantom used to test the everting emergency airway device. *Left*: Isolation of the essential anatomy from design models of the male AJAMS model. *Center*: Rigid printed airway phantom used in airway tests with clinical endotracheal intubation tube. *Right*: Phantom with plain tube everting past the uvula. 110

4.11 Straight airway sealing setup for EAD-2. Unlike EAD-1, EAD-2 did not include breathing channels, and simulated breathing pressure was supplied externally. Note: EAD-2 was not everted from a reel, and does not have the "tail" seen between the tube tip and the reel as in the top of Figure 4.3. . . 111

4.12 EAD-3 manufacturing process. **A**: Outline of desired seam in CAD. **B**: STL file of outline imported into PrusaSlicer. **C**: Sheets of TPU sandwiched between parchment paper on Pruska MKS3+. **D**: Sealing path of tube shape. **E**: Sealed tube before cutting. **F**: New tube after excess material is cut away. 113

4.13 Deployment of a straight tube into the esophagus (left) and a curved tube deployed into the trachea (right) in the EAD-3 airway phantom. The phantom is mounted to the XY plane of an ATI force sensor and the assembly is capable of rotating ±30∘ about a point near the center of the mouth with the Z axis pointed towards the reader. 115

4.14 EAD-3 straight control tube (above) and curved tube (below) designed to deploy to the trachea. 116

4.15 Maximum everting pressure (*left*) and normalized max force (*right*) during phantom deployment. The everting pressure is the pressure that was required to fully deploy a tube within the airway phantom. The magnitude of force is represented by the net area of contact between the tube and the anatomy. A higher area will apply more force per unit pressure. 117

4.16 Norm of XY force during everting forces trials at constant pressure. 119

A.1 Schematic for arduino-based current control of variable pressure regulator. . 148

A.2 Protoboard layout for current-controlled pressure regulator, digital reset button, and flow sensor interface. 149

LIST OF TABLES

Table Number		Page
2.1	Moment of Inertia Characterization of Reel	30
2.2	Characterization of Friction Torques	30
2.3	Number of Reel-Based Position Estimation Trials	37
2.4	Test 1 - Rising Inertia Results	40
2.5	Tests 2 & 3 - Increasing Friction Results	42
2.6	Reel Stopping Time and Distance From 600 mm/s (9.5 rev/s)	48
2.7	Inertia and Friction Force During Trials	50
3.1	Trials and Conditions for Eversion and Friction Characterization	72
3.2	Average (Std. Dev.) Coefficient of Friction Results	84
4.1	Evaluation Tests for EAD Prototypes	98
4.2	Instances of Tracheal Deployment During Everting Pressure Trials	120
4.3	Comparison of Commercial and EAD Devices	120
A.1	Component Values for Pressure Control Circuit	149

ACKNOWLEDGMENTS

This dissertation would not be possible with the yearslong mentorship of Blake Hannaford and Eric Seibel: their wide ranging expertise and interests have allowed me to feel supported in all of my academic and professional pursuits. I would like to thank the members of the UW BioRobotics Lab for their camaraderie, curiosity, and infectious enthusiasm for medical robotics. I greatly appreciate all of the discussions and input from the surgeons and physicians that have joined in collaboration with my work. Thanks to Professor Greg Fischer at WPI for inspiring my interest in surgical robotics and for encouraging me to pursue graduate school at the UW. Much of the financial support through this process has been provided by UW CoMotion, and their belief in my projects has been encouraging. I am grateful to the tireless efforts of the World Ventilator Foundation for pulling together during the pandemic to try to solve a world-scale problem, and for giving me the trust, space, and expert advice to learn and grow. I am likewise indebted to my colleagues during my internship at Meta Reality Labs Research for the opportunity to contribute to the cutting edge of virtual reality experiences. I am deeply indebted to Brenda McKenzie at Hall Health for guiding me through recovery after a back injury and giving me the tools to stay healthy and walking upright. My friends and family have been endlessly inspirational and supportive throughout my academic and professional career. Finally, thanks to Katie and George for their constant companionship and support through the long trials of striving for a PhD.

DEDICATION

To my family for getting me here,

To my friends for leading the way,

And to Katie, my constant sunshine

Chapter 1

INTRODUCTION

1.1 Motivation

Medical robots have gained significant commercial traction since the regulatory approval of the da Vinci surgical robot in 1999 [1, 2]. The da Vinci and many of the medical robots introduced in the decades since have relied on rigid robot arms and tools in order to provide greater access for surgeons and improved outcomes for patients. While these platforms can increase the abilities of surgeons over traditional manual and endoscopic methods, access to many areas of the body still require incisions in order to be reached with rigid tools, and some sensitive organs and tissues are at great risk of accidental damage from rigid tools. There have been a myriad of proposed robots that seek to overcome the limitations of rigid robot design by leveraging flexible materials or designs for surgical, diagnostic, and therapeutic applications [3]. These flexible or soft robots often seek to reduce recovery time by gaining access to desired anatomy through natural orifices.

A promising type of soft robot for medical applications is an everting tube robot. An everting tube robot, also called a vine robot, is a soft robot that uses pressure within the body to pull new material forward and out through the tip [4]. Since new material travels though the center of the tubular body, there is no sliding against the environment (Fig. 1.1) and the robot can easily navigate tortuous or constricted areas. The bodies of everted tubes are generally made of thin, inelastic sheets of plastic or coated fabric. One of the key characteristics of an everting tube robot is that it can passively navigate a complicated environment without feedback control, which can be considered a type of mechanical intelligence.

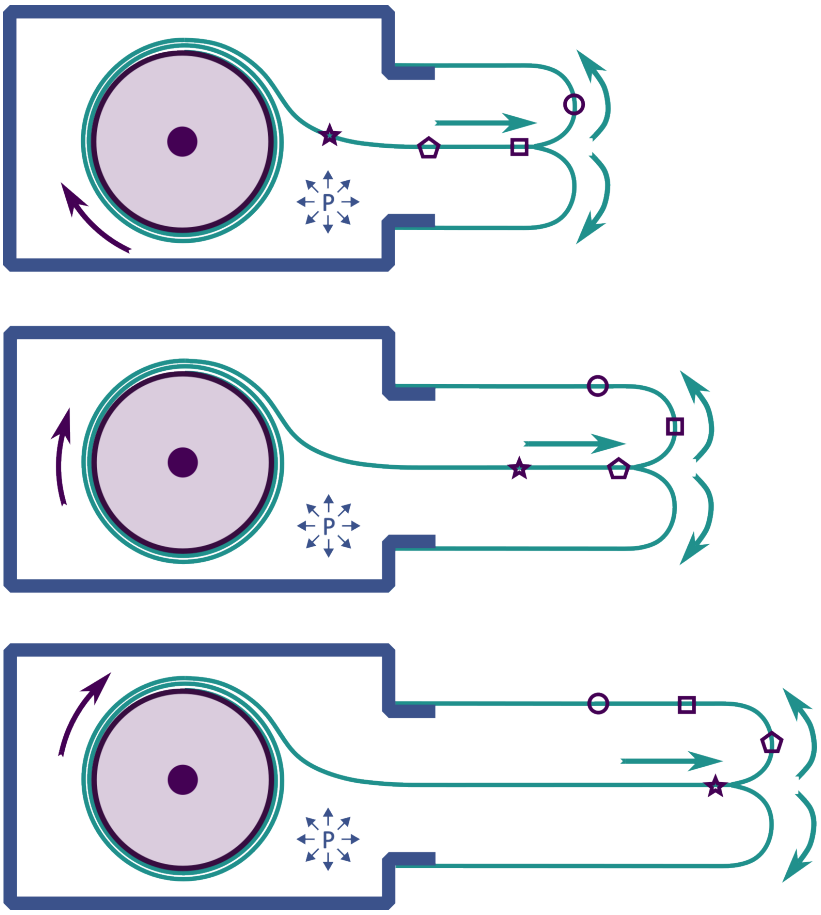

Figure 1.1: The eversion process uses pressure within an inelastic tube to pull new material from a reel so that the inflated tube grows at the tip. Note that once the material (purple shapes) has been pulled to the outside, that section of material remains in place.

1.2 Dissertation Focus

This dissertation will focus on the modeling of everting tube robot growth and applying these models to the design of an emergency medical device.

1.2.1 1 - Dynamic Effects of Everting Tube Robots

There has been significant interest in predicting and exploiting the passive behaviors of everting tubes, but few studies have investigated methods for accurate, real-time estimation of the length of the everting tube during growth in arbitrary environments. Improved estimation of tube growth could help in feedback control of tube position or actuation, environmental characterization through analysis of growth behavior, or finer understanding of eversion mechanics and interaction, which can lead to insights for designing everting systems for difficult applications.

Research Aim 1: Investigate the effects of friction and rotational inertia on the accuracy of reel-based position estimation of everting tube robots.

1.2.2 2 - Friction Effects of Everting Tube Robots with Central Working Channels

Several proposed applications for everting tube robots include the deployment of sensors or tools through the central passageway of the everting tube. A rigid or flexible pipe through which these sensors or tools could pass is called a working channel. In order to advance the working channel at the same rate as the growing tube, the tube material needs to slide along the outer diameter of the working channel. Understanding the friction interaction between the working channel and the everting tube is key to designing everting tube systems with working channels.

Research Aim 2: Demonstrate a method for estimating the static and dynamic friction between an everting tube and a working channel with the central lumen of the tube.

1.2.3 3 - Designing an Everting Tube Robot for Establishing Airways in Emergencies

Airway management is critical to patient survival in cases of cardiac arrest, drug overdose, and trauma. In 2021, there were nearly 150,000 reported cases of out of hospital cardiac arrest with over 90% leading to death. Current methods of establishing airways in response to cardiac arrest require a high level of expertise, and improper use can result in serious side-effects and death. This poses a need for a safer emergency airway device that can be used by minimally trained bystanders. Since everting tube robots can guide themselves through narrow, curving areas without sliding, they are an ideal candidate for gaining access to the airway with minimal user input.

Research Aim 3: Design an emergency airway device that can reliably deploy into the airway and provide a channel for rescue breaths.

1.3 Literature Review

1.3.1 Soft Robots

As a field, soft robotics has gained significant momentum in the last 10-15 years with the manufacturing and sensing capabilities driven by 3D printing[5] and smart phone ubiquity [6]. Polygerinos et al. review the wide range of benefits and applications of soft robots in the field of human interaction [5]. Soft robots easily take inspiration from nature by integrating compliant muscle-like actuation with, rigid or semi-rigid bones and flexible skins. This not only inspires designs, but makes soft robots naturally compatible with interacting with humans either as separate agents acting in the same space or as intrinsically safe wearable or assistive devices.

In [7], Runciman et al. directly compare 34 soft robots designed for minimally invasive surgery without significant rigid components. Only 3 of these robots were published before 2013 and the growth rate appears to be increasing. The soft, everting robot of [4] was likely excluded because it is not presented as a medical robot. However, many of the robots share properties with the vine robots and similar robots will likely be included in future soft medical

robot reviews.

1.3.2 Everting Tubes

In the few years since the publication of [4], the authors have authored over a dozen papers exploring the uses of apical robots and other researchers are beginning to utilize them as well. The research performed by Okamura and Hawkes have generally been focused on exploring new construction techniques, developing models for new application domains, and developing human interactions with haptics and teleoperation.

In the same year as [4], Blumenschein et al. presented the model and experiments from the supplemental material from [4] with a few more details and small tweaks to the model in [8]. Also in that year, Slade et al. published a description of apical extension robots as soft, patient-specific catheters for reaching sensitive areas in the brain and kidneys [9]. These soft catheters were shown to decrease normal force applied to tissues by an order of 100 and could also supply a stiffness range of 500x. However, description of the deployment of the catheter was not discussed.

Further descriptions of new applications include the use of a small, pre-formed helical robot that could be deployed from around a human's wrist to provide haptic force and directional cues to the forearm [10]. Achieving helically shaped robots with shape control and their applications for antenna deployment and grasping were discussed in [11]. Further research in antenna deployment led to [12], which describes a conductive path along the outside that is broken at the tip of the robot in order to allow for closed-loop control of resonant frequency in a field-deployable antenna. This work also introduced a branching structure that could individually control the length of each branch. An additional pneumatic line was added through the center of the robot body in [13] that split into two halves at the tip of the robot. This pneumatic tube introduced high-pressure flow out of the tip in order to fluidize dirt around the tip for easier burrowing (an area explored by earlier apical robot research [14, 15, 16] for use in planetary exploration).

A simple, non-steerable apical robot was used to model obstacle collisions and use obsta-

cle interactions to plan paths to endpoints without a straight solution [17]. While obstacle based navigation was shown to be useful in benchtop mazes, a controllable and reversible steering mechanism was introduced in [18] that utilizes lengthwise pneumatic actuators on three or four sides to bend the body of the robot. This steering mechanism is more similar to traditional soft actuators [19] than the permanent and semi-permanent steering introduced in [4] but is shown with everted growing for the first time. The turning of [18] trades reconfigurability for environmental interaction because it requires a counter force either at the base of the robot or at points that may be in contact with the body. While this may not be acceptable for sensitive areas in the body, this type of steering may be preferable for autonomous or teleoperated exploration of new areas, as described in [20]. A user study with simulated growth robots and a variety of human interfaces describes first person teleoperation of growing robots (published at almost the same times as this kinematics-based, flexible surgical robot teleoperation work from Imperial College London [21]) and includes the use of a puppet version of the robot tip with input for shape, growth rate, and indexing.

These lab-based exercises in exploring the design, control, and manufacturing of apical robots culminated in the design of a field-deployable robot that was used for a soft robot competition and an archaeological expedition in Peru [22] and the introduction of the term Vine Robot. The deployable vine robot was ruggedized for archaeology with a flexible nylon outer sheath which included a zippered section to manage the cable pulled along the outside of the body for a camera and lights mounted in a stiff cap at the tip of the robot. Teleoperation was controlled with a master device similar to [20]. The archaeological exploration was successful in capturing video of never-before-seen areas of Andean ruins at three sites. This experience uncovered several shortcomings of the robot control and design: slow growth speed due to pressure drop along the long length (compared to diameter); non-robust heat-sealing of the pneumatic steering actuators; loss of situational awareness from camera roll and first-person control; inability to squeeze smaller than the camera cap; and inability to reverse the growth of the robot due to buckling. The vine robot was one of the most adept robots at completing the challenges of the competition, but it was heavily penalized because

the entire robot body did not traverse the course. The buckling issue is characterized and an inverting mechanism is introduced in the recently submitted [23]. The mechanism is pushed along the tip of the robot until retraction (inversion) is desired, at which time it uses two small motorized rollers to apply direct inversion tension instead of applying tension from the base of the robot, which may cause curved sections of the body to buckle. This mechanism also has the advantage of significantly decreasing environmental interaction forces when retracting through constricted curves.

Classes of Everting Tubes

Everting tube robots can be classified by the means with which the everting material is stored before growth. Figure 1.2 illustrates the three main types within the literature.

Rotary Eversion describes the style of everting tube detailed in [4] where everting material is wrapped around a reel within the pressure vessel. The reel may be attached to a motor and/or rotary position sensor.

Bulk Eversion is a method generally used for everting complex shapes that do not fit neatly on a reel or require rate control or retraction. The everting tube is placed loosely inside the pressure vessel in an inverted configuration and allowed to evert without mechanical control.

Linear Eversion allows for access to the central lumen of an everting tube throughout its growth. With rotary eversion, access to the central lumen requires complicated winding of a flexible channel. Linear eversion uses a rigid pipe attached to the free end of the everting tube. The rigid pipe traverses a seal in the wall of the pressure vessel. Advancing the pipe allows the everting tube to grow and access to the everting tube's central lumen is available through the pipe.

Everting Tubes in Medicine

Everting tubes, sometimes referred to as toposcopic tubes, with manual control have been investigated in various medical fields for decades but have not yet been established in common

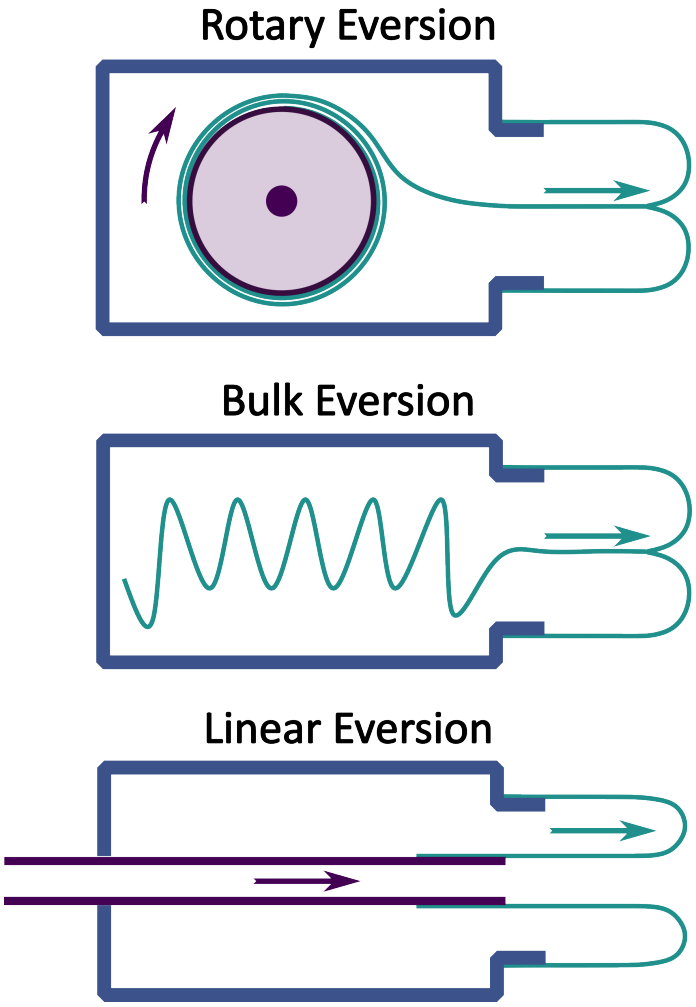

Figure 1.2: A proposed method for classifying the ways that the bodies of everting tube robots are stored prior to growth.

practice. An early everting endoscope was patented in 1982 [24], a colonoscope that used an everting balloon to enable access to the colon was presented in 1986 [25], and another patent for gaining access to fallopian tubes was awarded in 1994 [26]. These seem to have been used for a handful of clinical studies [27, 28, 29], but have not seen much commercial development. Keenan et al. recently described efforts to design everted tubes for gaining access to fallopian tubes in order to improve fallopian and ovarian cancer diagnosis. All of these developments utilize linear eversion in order to maintain a central lumen for passing tools, materials, and endoscopes. Pneumatic and hydraulic eversion is useful in these applications because there is no sliding against the anatomy, constricted anatomy can be opened with evenly distributed pressure, and the technology is easily scalable. These early attempts at medical everting tubes are not discussed in [4] or in related research by Okamura, Hawkes, *et al.*, however a combination between this new robotics research and established medical needs shows promise to be an impactful area of future research.

Everting Tubes as Introducers for Robotic Catheters

Researchers at King's College London recently published what could be the first robot with a controlled, flexible working channel and a co-deployed everting tube [30]. The application presented was that of navigation within mammary ducts to diagnose suspicious growths. Further details of MAMMOBOT will be described in future chapters.

1.3.3 Flexible Continuum Robots in Medicine

Soft medical robots are experiencing rapid exploration in academia while their predecessors are beginning their introduction to commercial sales. Rigid tools controlled by large robots have been the norm since the first clinical surgical robots in the late 1990s [31], and academics have been exploring the use of flexible tools to enable access to new areas of the body ever since [32, 33, 34]. Three new flexible, continuum surgical robots are being introduced in the near future: the Intuitive Surgical Ion [35], the Auris Monarch [36], and the MedRobotics Flex [37]. Each of these allows for natural access to the esophagus and lungs through the patient's

mouth. The Flex bears particular resemblance to [4] because it is based around technology that allows tip-wise growth and exploration while maintaining the shape of the proximal sections of the robot. The colonoscope in [38] uses an everting sheath that is purported to make colonoscopy more comfortable, but the sheath tip and scope tip do not seem to grow at the same rate. As these flexible robots become mainstream over the next decade, the current work on soft robots will likely lead to or inspire the next wave of commercial medical robotics.

1.4 Case Study: Application of Everting Tubes for Teleoperation of Medical Robots

Although not a primary focus of this dissertation, the following section explores the concept of teleoperated robotic diagnosis and the opportunity for everting tubes to act as an enabling technology. Everting tubes could likely improve adoption by both urologists and patients by improving the reliability of endoscopic insertion into the bladder and the comfort associated with insertion.

Safe and effective remote teleoperation of diagnostic and therapeutic procedures is likely to improve health outcomes in the general population by improving access to specialized care. A common clinical procedure for many specialties is flexible endoscopy, during which a doctor will insert a flexible endoscope into a natural orifice in order to inspect the anatomy, take samples, or deliver medication. In the case of teleoperated flexible endoscopy, the specialist will not be manually manipulating the endoscope and will therefore not be able to rely on the sense of touch to ensure safe insertion and navigation within the patient. A robotic introducer sheath may be able to mitigate the risks associated with poor remote control of endoscope insertion while also aiding the doctor with the insertion.

Everting tubes could act as an introducer mechanism that would not slide against the patient's anatomy while naturally following the shape of any constrained lumens. Everted tubes are a form of soft robot that is made from a tube of flexible, inelastic material. These tubes use inflation pressure at the tip to pull new material from the inside to the outside body

of the tube (Fig. 1.1). This means that the outside does not slide against its environment and the tip can open constrictions with even pressure. These tubes have been proposed for delivering medicine and endoscopes, but their use in robotic endoscopy is still relatively unexplored.

1.4.1 Flexible Cystoscopy

Flexible cystoscopy is an important diagnostic procedure performed by urologists in-office for procedures such as evaluating blood in urine (hematuria), removing stents after kidney stone surgery, and investigating urethral strictures [39]. A diagram of the procedure and the anatomical differences between male and female urinary systems can be seen in Figure 1.3. A diagnostic flexible cystoscopy usually begins with these steps: 1) insertion of the cystoscope into the urethra, 2) inflation and flushing of bladder with clear, sterile fluid pressurized through the working channel (throughout the procedure), 3) inspection of urethral wall during scope insertion, 4) insertion through bladder sphincters, 5) identification of common landmark (usually left or right ureteral orifice), and 6) inspection scan of the entire urothelium (bladder surface) with detailed inspection of areas of interest. Flexible cystoscopy is the gold standard for diagnosis and surveillance of bladder cancer, the 6^{th} most common and the most costly cancer in the US[40, 41]. Bladder cancer has a recurrence rate of over 50% [42], which requires that patients return to their urologists for followup cystoscopies up to 4 times per year for surveillance after initial treatment [43], and a delay in diagnosis of muscle-invasive tumors of 3-6 months can increase risk of death by bladder cancer by 34% [44]. Nearly 90% of urologists in the US practice in metropolitan areas [45], which can burden some patients with travel costs and time off work [41].

While we have focused on cystoscopy, there is a long history of using the body's natural orifices to access internal structures. These include transoral, transnasal, transanal, transotic, transvaginal, and transurethral approaches [9, 46, 47]. This method of access typically precludes the need for incisions with their associated pain and tissue damage, and in so doing lessens or obviates the need for anesthesia. This shortens procedure times, decreases

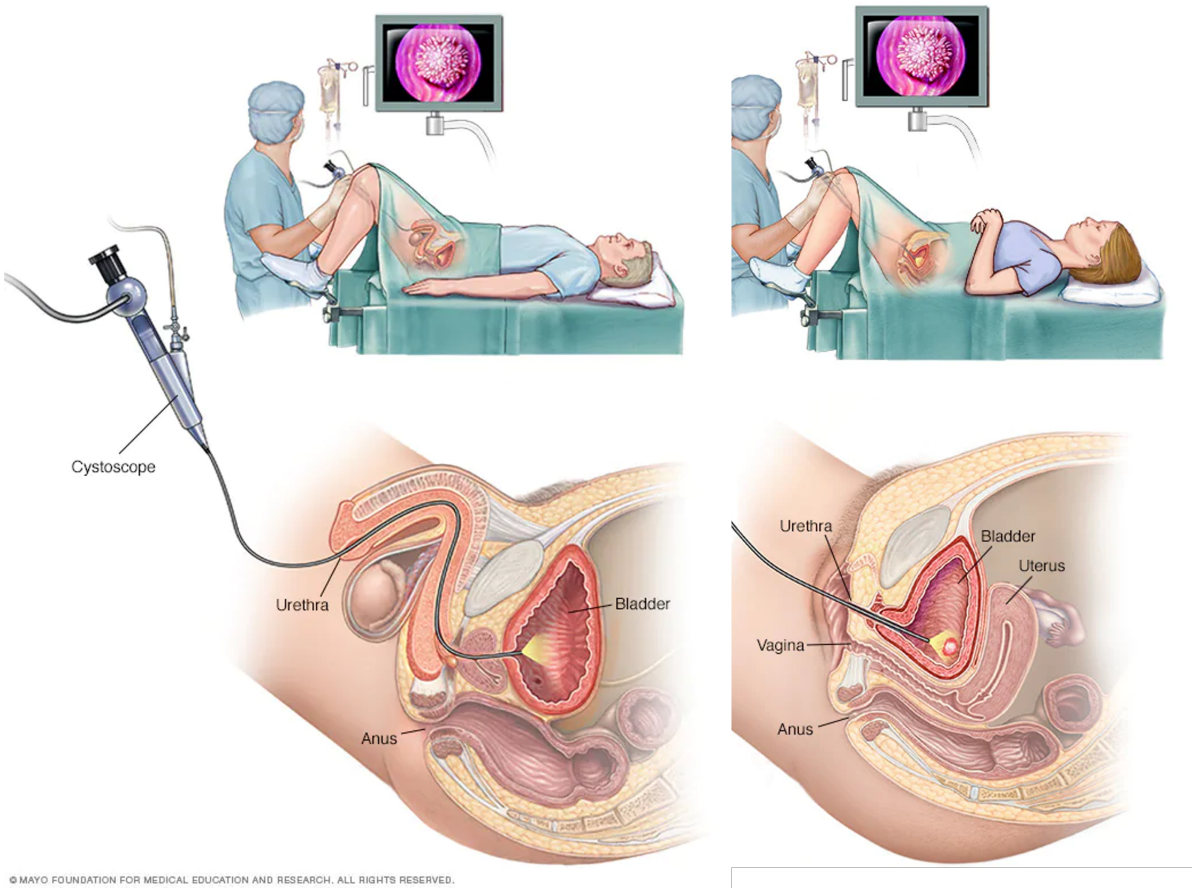

Figure 1.3: A flexible cystoscopy procedure being performed on a male (left) and female (right). The screens at the top show the video feed from the tip of the endoscope and are showing a bladder tumor. Note that the male urethra is much longer and more curved than the female urethra. The male urethra also passes through the prostate, which can be enlarged, especially in older patients. (Image ©the Mayo Clinic)

procedure costs, and increases the possible venues for said procedure. However, there can still be pain and discomfort with these approaches that is mitigated in a variety of ways. As the field of robotic surgery develops and the types of devices traversing natural orifices increases, additional research is needed into methods and technologies to alleviate discomfort and protect tissues. The approaches developed in this project may benefit other natural orifice platforms.

1.4.2 Teleoperation of Medical Robots

Bladder cancer patients in rural and underserved areas would benefit from a telerobotic cystoscopy system placed in geographically distributed clinics or urgent care facilities, set up and overseen by nurses, and operated by urologists located in their own office.

Although this vision of telecystoscopy is not yet in practice, the technologies required have already been demonstrated: the first transcontinental telesurgery was successfully completed two decades ago [48], telerobotic flexible endoscopes are being introduced commercially for use with surgeons in the room [36, 49], and researchers are developing transurethral surgery robots [50, 51, 52]. Introducing teleoperation for bladder inspection is logical because the organ is pliable and not close to critical life-sustaining functions and nurses are well experienced with insertion of urinary catheters. Widespread adoption of clinic-based telecystoscopy will likely begin with a telerobotic platform that can interface with off the shelf, and perhaps single-use cystoscopes [53] which reduces infrastructure overhead. Thus, flexible cystoscopy may serve well as a test case for long-distance teleoperation by urologists in major cities and patients in clinics with nursing and general practitioner support, reducing barriers to timely specialty care.

1.4.3 A Telecystoscopy Robot with Everting Tube Introducer

An everting tube introducer may be especially useful for inserting a flexible cystoscope during teleoperation of routine bladder surveillance and diagnostics. With a telerobotic cystoscopy platform (Fig. 1.4) distributed in rural and suburban areas that can be set up and monitored

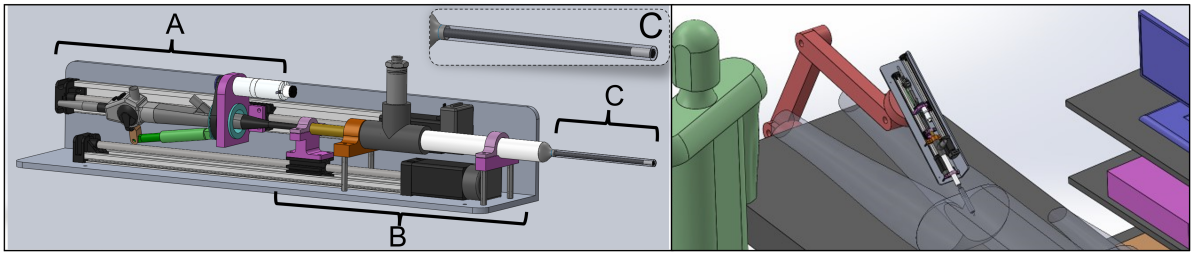

Figure 1.4: The TelCys platform designed to allow safe teleoperation of routine urological diagnostic exams. *Left*: A - The flexible cystoscope control module, B - the linear everting tube control module, and C - the flexible cystoscope tip within the everting tube introducer. *Right*: A nurse supervising the deployed TelCys robot.

by a nurse, patients can receive time-sensitive care without travelling long distances to get to urology offices. Insertion of the cystoscope into the bladder is a sensitive procedure that requires expertise, and performing it remotely may be done more safely and reliably with the aid of an everting introducer.

Desired Characteristics

We can identify desirable qualities in the operation of a telerobotic cystoscopy with everting introducer, based on providing safe cystoscopies of high diagnostic quality:

1 - Low sliding and interaction forces - The everted tube introducer is an element of this proposed system because of its ability to increase safety (and perhaps comfort) to the patient by reducing forces applied to the patient [54].

2 - Smooth insertion, rotation, and bending - While traveling through the urethra, the endoscope should be able to actuate smoothly. Once the endoscope enters the bladder neck, the everting introducer should stop advancing and not affect the operation of the endoscope during urothelium inspection. Static Friction (Stiction) against the everting tube could cause jerkiness in the video feed when motion is started or when the everted tube stops growing while the endoscope continues.

3 - Unobstructed views of all anatomy - Cystoscopy is a general diagnostic proce-

dure used by urologists for visualization of many different areas of urologic anatomy. Thus, control of the robot system must allow for unobstructed visualization of all anatomy without obstruction or distortion by the everting tube.

4 - Minimized applied pressure - High pressure applied within urethra has the potential to permanently damage the wall of the urethra and sustained pressures may cause immediate or prolonged discomfort.

1.5 Summary

The proceeding chapters cover a body of work that focuses on understanding the mechanics, dynamics, and applications of everting tubes. The simplicity of everting tubes, combined with their extraordinary abilities and endless opportunities for application-based customization, make them a very promising area for research and deeper understanding. Chapters 2 and 3 detail benchtop experiments with novel sensing and analysis that have not been applied to everting tubes. The experimental analysis and design guidelines that result from these experiments can be used by researchers and engineers to more deeply understand how everting tubes work and can be used for future robotic and medical applications. The 4^{th} chapter highlights the development strategy and incremental improvements of an everting medical device that can be used by minimally-trained users in the case of an airway emergency. The experimental results from this design process indicate significant potential for a commercial lifesaving device.

Chapter 2

USING FRICTION TO IMPROVE GROWTH ESTIMATION OF REEL-MOUNTED EVERTING ROBOTS

Research Aim 1: Investigate the effects of friction and rotational inertia on the accuracy of reel-based position estimation of everting tube robots.

2.1 Introduction

A common and simple method for sensing eversion growth is with an encoder mounted to the reel where the eversion material is stored. This sensing method works well during positive growth acceleration, but may lose its direct relationship with tip growth when the tip of the robot decelerates, as when it encounters an obstacle or constriction. When this happens, the material reel will continue to spin due to its rotational inertia, letting out extra slack material, and will not have an accurate estimation of the tip position until the robot grows enough to pull the slackened material taut (Fig. 2.1). Although a motor could be used prevent slack by applying a small torque in opposition to growth, such a solution would require sensitive design, sensing, and control in order to compensate for slack without affecting the dynamics of tube growth, as well as added system cost.

The aim of this chapter is to study a simple solution to these estimation challenges: a friction element to reduce the effects of over spinning. The primary experiment in this work investigates the effects of varying reel inertia and reel friction on the accuracy of the encoder-based estimation during growth. Additionally, this chapter introduces a method for empirically characterizing the physical characteristics of an experimental eversion reel, and investigates a novel tube-adjunct method (Fig. 2.3) for using of a Time of Flight (ToF) sensor for ground truth tip position sensing of an everting tube.

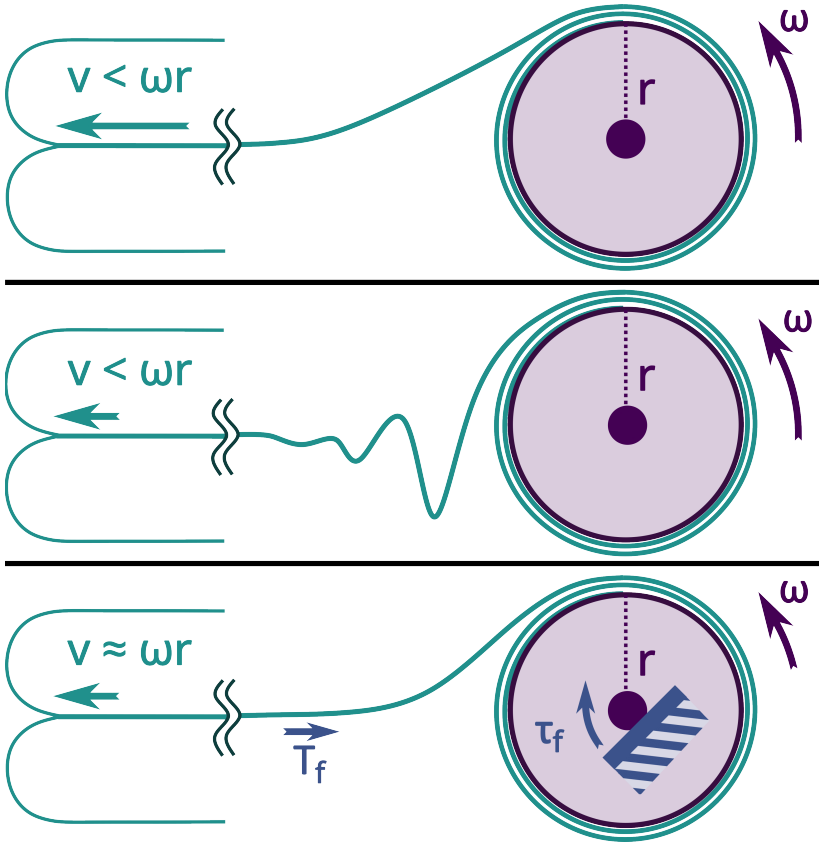

Figure 2.1: Slack between the tip of an everted tube and its material reel will cause inaccurate estimations of tube tip position from an encoder at the reel. ***Top***: When the growing tube's velocity, v, matches the linear velocity of its material reel, ωr, the material remains taut and there is a predictable relationship between reel angle and tube tip position. ***Center***: When the tube growth slows down, inertia of the reel will cause extra material to unroll, causing a discrepancy between the reel position and tube tip position. ***Bottom***: Friction torque on the reel, τ_f, will slow growth while preventing over-spin, making tube tip position more predictable during dynamic growth.

2.1.1 Related Work

There has been a wide array of proposed applications for everting tube robots, from exploration of coral reefs [55] and previously unseen archaeological sites [56], to medical diagnostics [21, 9] and emergency response [57, 58]. Many of these applications have been grouped by Mazzolai et al. into one or a combination of the following: deploying structures, applying forces, or navigating constrained environments [59]. The goals and specific requirements of each application tend to drive the overall tube construction and the sensing and modeling strategies available to each robot. Beyond the rotary encoder mounted on the reel or motor [56], everting tube robots have been fitted with: pressure sensors and microphones to understand their growth and environments [60]; cameras to allow for teleoperation [61, 56] and automation [62]; and environmental sensors to be deployed as payloads from the tip [62]. Experimental validation of everting tube tip position and body shape is generally performed using external camera systems and reel encoder based estimation, however video analysis is limited to laboratory setups.

An accepted model for the growth of everted tubes is a quasi-static force model based on the apical, or tipwise, growth of vines [8]:

$$\frac{1}{2}P_{grow}A = \frac{1}{2}P_{yield} * A + (\frac{1}{\varphi}v)^{\frac{1}{n}}A. \tag{2.1}$$

This model relates the driving pressure of the system, P_{grow}, and its frontal area, A, to the rate of tube growth, v, noting that a certain amount of pressure, P_{yield} must be overcome in order to initiate growth, known as yield pressure or the minimum eversion pressure. φ is the growing tubes viscoplastic extensibility and the $\frac{1}{n}$ exponent is a near unity power term fit to the growth rate. Only half of the system pressure acts towards growth because the other half acts on the static material that has already everted. Additional, path-dependent terms also restrict the growth rate by modeling friction of the tail material, but are skipped here for brevity. This model was extended by [63] to include considerations for a working channel within the new material in the robot body of a linear everting device, which attaches the

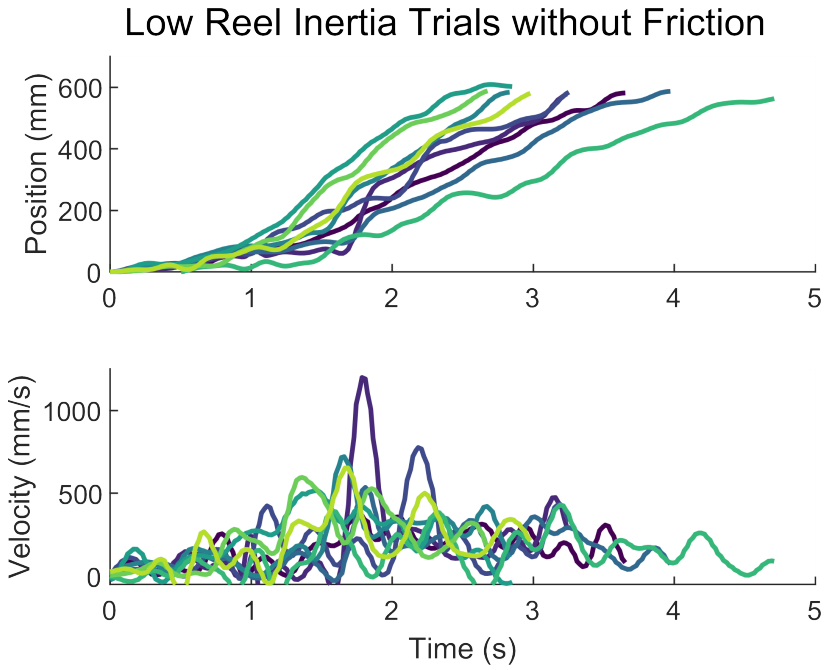

Figure 2.2: Nine eversion growth trajectories from 3 tubes under similar conditions as measured by Time of Flight (ToF) position sensor. ***Top***: Position of tube tip during growth. ***Bottom***: Tube tip velocity.

robot's tail to a sliding, rigid rod instead of a reel. Another extension of this model further investigated the potential limits of the size of the working channel with a linear eversion base [64]. Other work has focused on the buckling [65, 66], kinematics [67], and retraction [68] of the tube when in contact with external objects or forces.

As a general model of everting tube growth, the apical model in [8] does not consider the effects of a material reel on tube growth. Instead, the effects are likely to be lumped into the value of the minimum eversion pressure. When the new material inside the body, also referred to as the tail, is taut between the tip of the tube and the reel, the reel's moment of inertia and any friction within the reel system will resist the growth of the tube, thus increasing the pressure required to grow over a tube without a reel.

The primary contribution of this chapter is the experimental validation of the effects of a reel friction mechanism on the accuracy of reel-based estimation of eversion growth.

The experimental platform used for these studies is described in Section 2.2. In Section 2.3, several system measurements are performed in order to validate system performance and contextualize the results of the eversion accuracy experiment. Section 2.4 describes the development and performance of our novel everting tube position sensing system based on a Time of Flight sensor. The remaining sections detail the methods and results of the eversion accuracy experiment, followed by a discussion and conclusions.

2.2 Experimental System

The experimental system consists of the base from which the everting tube grows and which houses the material reel, the pneumatic system that powers eversion, and a data collection system for analysis. These subsystems will be described followed by a explanation of the configurations used during experimentation.

2.2.1 Everter Base

The eversion system consists of a pressure vessel, material reel, and "eversion snout" (Fig. 2.4). The system used for this experiment is based on that used in [66, 57], with an updated replaceable snout and gripper end plug for quick internal access between experiments. The snout piece is interchangeable for different diameter tubes and held to the pressure vessel with a sandwiched layer of silicone and two clamps. The cable for the reel encoder passes through a silicone sealed hole in the semi-permanent end cap.

The tubing material used for these eversion experiments was 2 mil, 1.5" flat width (~1" diameter) LDPE polytubing (Uline), and was chosen because of its common use in eversion research and because it does not require sealing or sewing in order to construct each tube. Although not determined empirically in this work, the minimum eversion pressure for this material without the reel was roughly 1 psi (7 kPa) and the burst pressure for this material was 6 psi (41 kPa) as measured by the digital pressure sensor on an unused new tube.

The material reel (Fig. 2.4) is made of 3D printed PLA and has a width just over the 1.5 inch flat width of the material. A set screw holds the reel to the axle and a countersunk

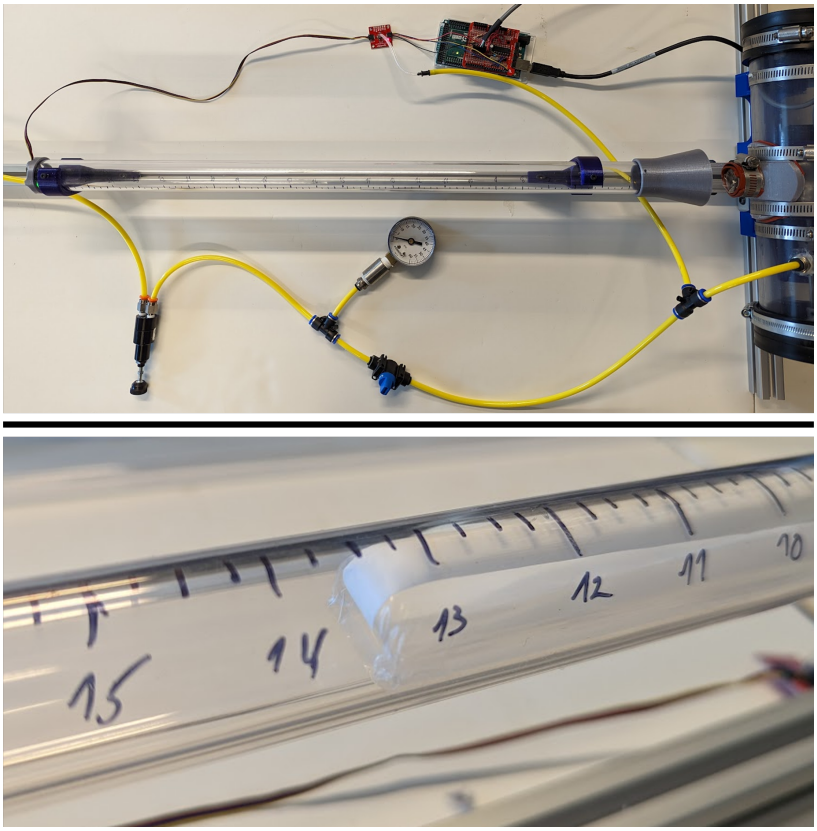

Figure 2.3: The eversion system used for these experiments. ***Top***: A Time of Flight sensor mounted to the left end of a clear growth pipe measures the tip position of the everting tube during its growth from the everter base on the right. ***Bottom***: A white PTFE plumbers tape ribbon (indicated by arrow) within the LDPE everting tube increases the accuracy of the Time of Flight sensor, as described in section 2.4.

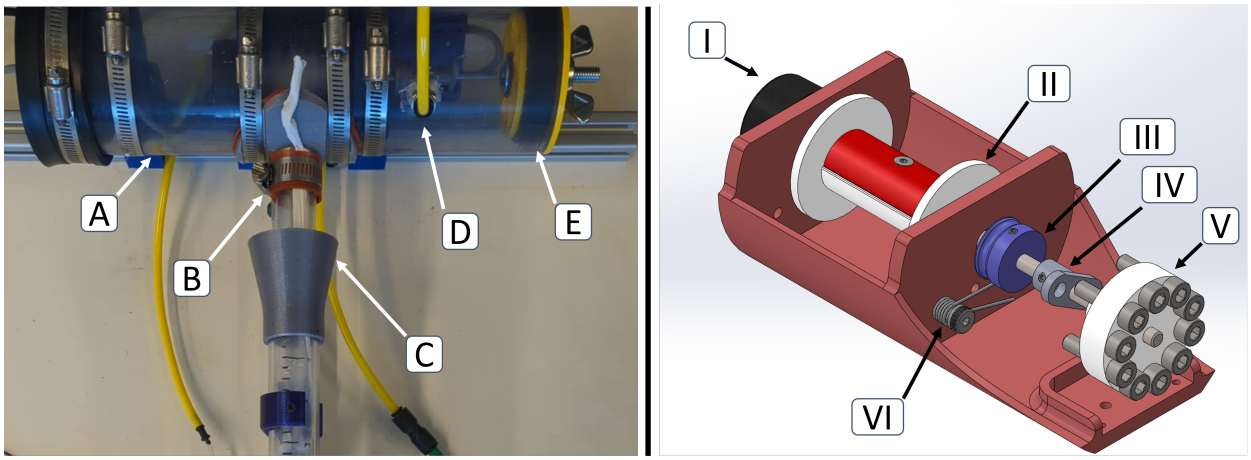

Figure 2.4: ***Left***: The eversion system with an LDPE tube everting into a clear pipe. **A** - 3" (75mm) polycarbonate pressure vessel. **B** - "Eversion snout" where the everting material is sealed to the pressure vessel. **C** - Guide funnel leading into the clear polycarbonate pipe. **D** - 1/4" (6mm) pneumatic pressure inlet. **E** - Gripper plug end cap for quick access. ***Right***: CAD of the removable eversion reel mechanism. The stainless steel axle is supported by ball bearings. **I** - Differential quadrature encoder. **II** - Eversion reel with removable piece (red) for clamp ing the end of the eversion material. **III** - Friction drum. **VI** Torsion spring pressing against the groove in the friction drum. **IV** - Winder knob aids rewinding the eversion material between trials. **V** - The inertia wheel increases the rotational inertia of the reel.

screw attaches the clamping plate to the reel. A hole is pierced near the end of the tube for this screw to pass through. Flanged ball bearings support the reel assembly with minimal internal drag.

The eversion snout leads directly to a growth pipe with the same inner diameter as the outer diameter of the everting tube material. The pipe is made of clear polycarbonate for observing tube growth and to aid with light-based sensing. A funnel at the entrance to the pipe helps to redirect the everting tube if it emerges off-axis from the snout. A quarter-inch scale was transferred to the pipe with the 0 inch position aligned with the distal end of the eversion snout.

2.2.2 Pneumatics

Supply pressure for these experiments was sourced from an 11 gallon air tank filled to 10-60 psi and regulated to experiment pressure by an adjustable low pressure regulator (Fig. 2.3). An On/Off ball valve was used to initiate eversion, and a gauge before the valve monitors system pressure before pressurizing the everter base. A needle valve with dial indicator regulated flow to a predictable rate (not shown in Fig. 2.3).

2.2.3 Data Collection

An Arduino Uno collected sensor data from a pressure sensor, differential encoder counter, and Time of Flight sensor. The pressure sensor (Sparkfun, SEN-16476) has a calibrated range of 1-25 psi and was connected in parallel with the everter base pressure inlet. The quadrature encoder counter (LSC/CSI, LS37366) and 20 MHz timing crystal kept track of the position of the 1000 count differential encoder (US Digital, E2-1000) mounted to the material reel axle without overloading the Arduino with interrupts. The Time of Flight distance sensor (Adafruit, VL53L0X) uses a 940 nm IR laser to determine distance within a range of 50-1200 mm. A python program on a laptop initiates data collection with a series of questions for the user to be recorded as metadata (`https://github.com/uw-biorobotics/brl_data`) and then requests sensor data from the Arduino via serial port at 50 Hz while saving the data into a CSV file.

2.2.4 Rotational Inertia Configurations

The rotational components of the three configurations tested in this work are:

1. Low - The everting tube material wrapped around the reel, a friction drum, a winder knob, and the encoder disc.

2. Medium - The Low configuration plus an inertia disc with five steel M5x10mm socket screws at a radius of 15 mm.

3. High - The Medium configuration plus five M5x20 screws on the same radius (seen in Fig.2.4).

All components are fixed to the axle with set screws. These configurations were chosen to provide distinguishable steps in rotational inertia without over-exaggerating a reasonable reel design. The relative changes in inertia can be seen in Table 2.1 and are calculated in Section 2.3.

2.2.5 Friction Configurations

The three friction configurations in these experiments (Fig. 2.6) are:

1. Low - No friction is added to the system beyond internal resistance within the ball bearings.

2. Medium - A 3D printed PLA cylinder is pushed against the steel axle with a torsion spring.

3. High - The arm of a torsion spring is placed within the groove of the PLA friction drum.

These configurations were also chosen to provide meaningful steps in system friction while providing predictable friction forces at the angular velocities expected in the eversion experiments. For instance, it was found that PLA on PLA friction configurations demonstrated irregular friction at high speeds, likely due to melting. Steel on PLA appeared to provide constant kinetic friction (i.e., Coulomb friction) during the tests in Section 2.3.

2.3 Physical Characterization

The physical values of each configuration of reel friction and rotational moment of inertia of the reel were experimentally characterized outside of the eversion system. Since these are two unknown properties that cannot easily be isolated, two experiments with overlapping

conditions were conducted: an acceleration test with constant gravity load, and a deceleration test with no external load.

2.3.1 Reel Acceleration Experiment

A constant acceleration was applied to the reel by subjecting it to a gravity loaded mass. The difference between the mass's free fall acceleration of 9.8 m/s^2 and the measured acceleration should be due to the acceleration of the reel's moment of inertia and the friction torque within the bearings.

The reel was fixed 1.7m above a padded box and a string was attached to a 406g mass. The string was fixed to the reel and neatly spooled onto the reel before being dropped (Fig. 2.5). It is assumed that the mass of the string is negligible in calculating the reel's moment of inertia. The encoder positions were recorded at 80Hz during the drop. Drops with each of the inertial configurations were recorded 3 times without any additional friction applied. Data windows from each drop were isolated and the angular acceleration and mass acceleration were calculated from the angular position of the reel.

2.3.2 Reel Deceleration Experiment

The reel was manually accelerated with a string that was freely wrapped around the reel, so that it would separate from the reel at the end of acceleration. This experiment isolates the deceleration properties of the friction configurations in pure opposition to the reel's inertial torque without any external forces. The reel was in the medium inertia configuration and accelerated 5 times to peak velocities ranging from 2-4 m/s for each friction configuration. Encoder data was recorded and the deceleration after peek velocity was used to calculate the average reel deceleration for each configuration.

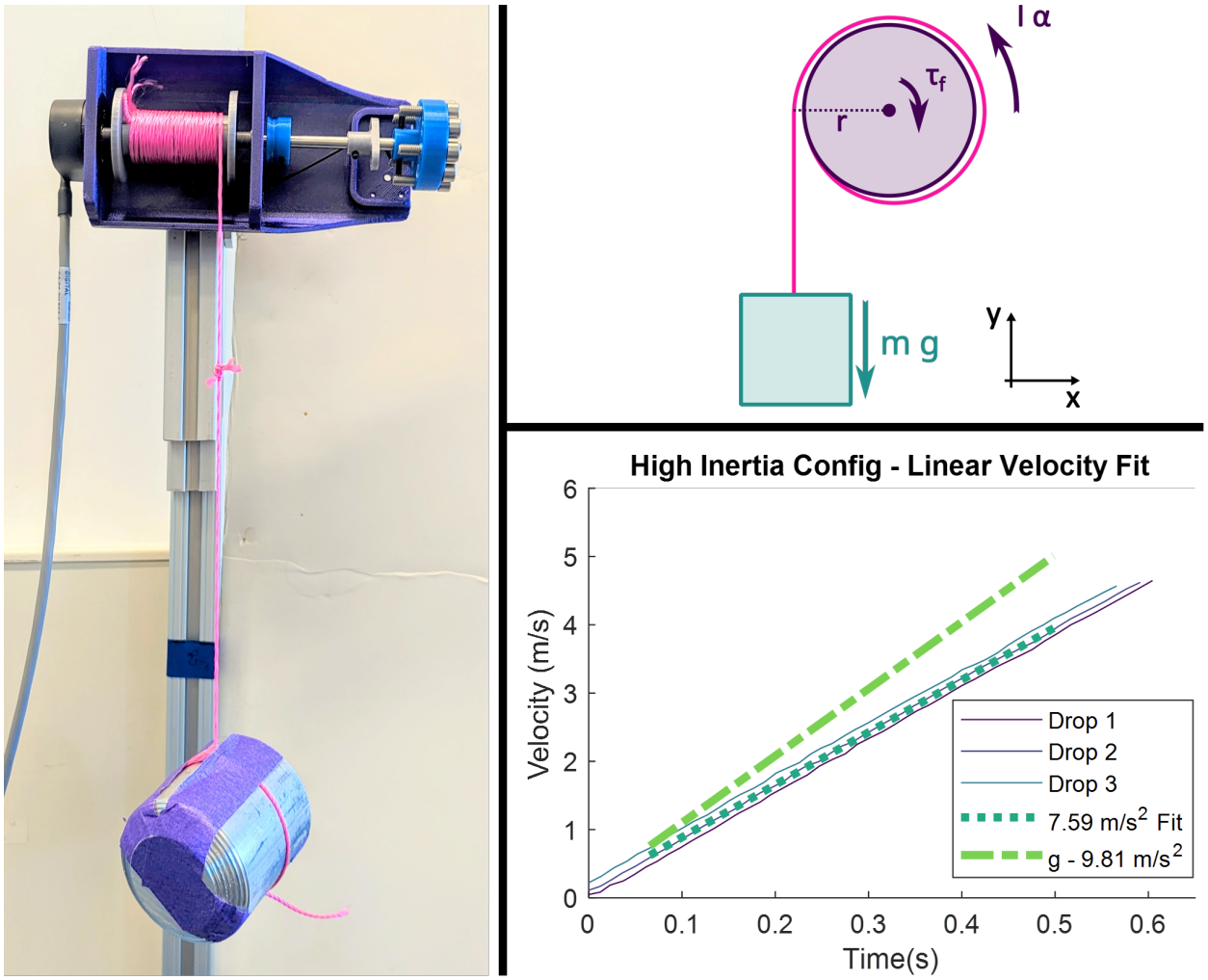

Figure 2.5: Reel acceleration experiment. ***Left***: Hardware setup for reel acceleration experiment. ***Right Top***: Free body diagram of acceleration experiment showing the gravity force (mg) at the reel radius (r), reel inertia torque ($I\alpha$), and reel friction torque (τ_f). ***Right Bottom***: Velocity of dropping mass recorded during high inertia drops with average linear fit compared to acceleration due to gravity.

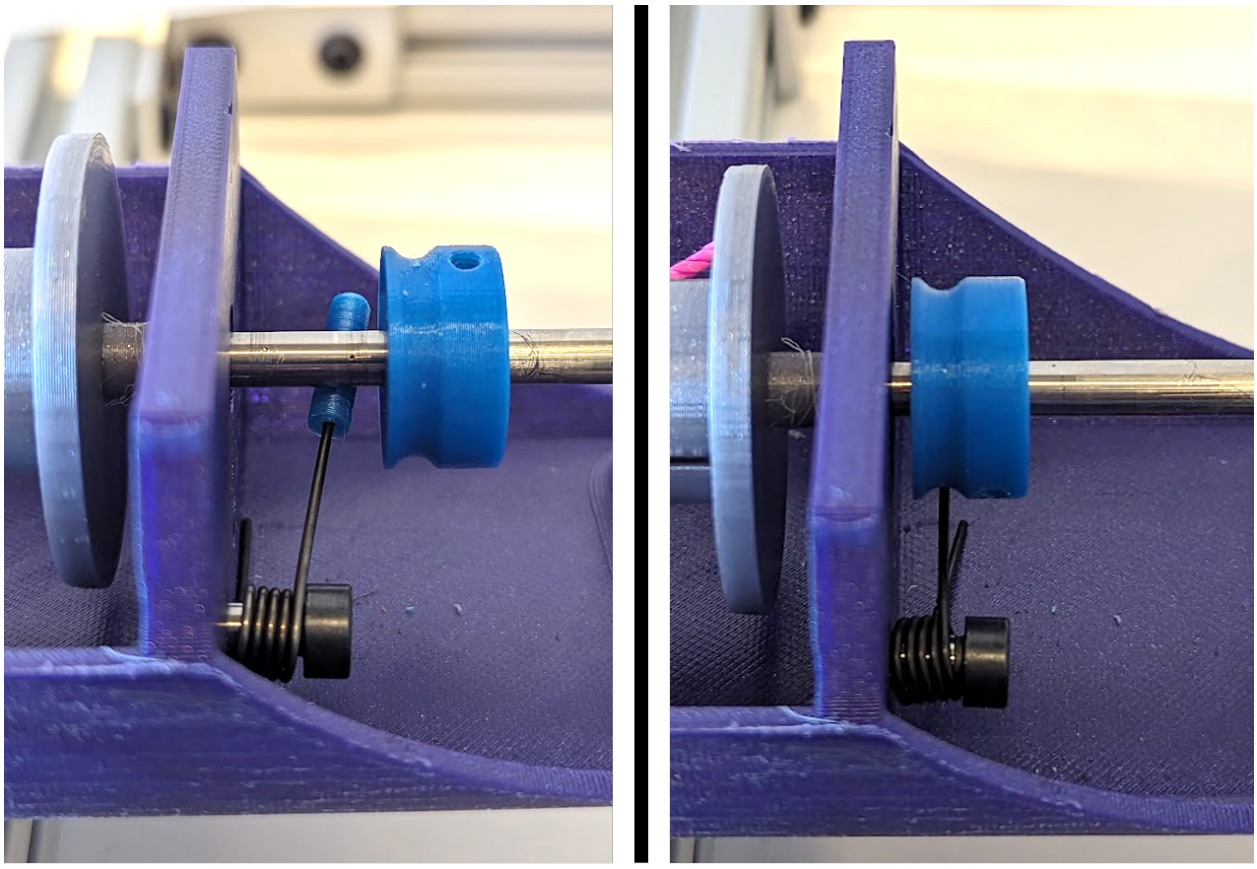

Figure 2.6: ***Left***: Medium Friction configuration with PLA friction pad held against steel axle. ***Right***: High Friction configuration with bare arm of spring held against PLA friction drum. The low friction configuration, not shown, removed the spring from the assembly.

2.3.3 Physical Constant Calculation

The system of can be describe where torque from the falling mass minus the constant friction torque is equal to the resultant acceleration of the rotational inertia of the reel:

$$I\alpha_a = mgr - \tau_f, \tag{2.2}$$

where m is the mass of the load, g is the acceleration due to gravity, r is the radius of the reel and string (10.9 mm), a_a is the linear acceleration of the mass during this experiment, and τ_f is the Coulomb friction torque. The deceleration experiment once the string has left the reel can also be described with (2.2) with the linear reel deceleration α_d and the external force term equal to 0:

$$I\alpha_d = \tau_f. \tag{2.3}$$

Since each experiment has a dataset with shared configurations of I and τ_f, (2.3) can be solved for I:

$$I = \frac{\tau_f}{\alpha_d}, \tag{2.4}$$

and substituted into (2.2):

$$\tau_f \frac{\alpha_a}{\alpha_d} = mgr - \tau_f. \tag{2.5}$$

This can now be solved for τ_f:

$$\tau_f + \tau_f \frac{\alpha_a}{\alpha_d} = mgr, \tag{2.6}$$

$$\tau_f = \frac{mgr}{1 + \frac{\alpha_a}{\alpha_d}}. \tag{2.7}$$

Since the reel conditions for the medium inertia configuration in the reel acceleration experiment were the same as in the low friction configuration of the reel deceleration experiment, these two datasets were used to find the value of low τ_f. The second derivative of the reel's angular position was calculated and averaged over the windows of interest in the acceleration and deceleration trials to find their average values, α_a and α_d for each trial. These

values were used in (2.7) to find the low friction torque: $\tau_f = 0.0029Nm$. The rotational inertia of each configuration could be determined from the average rotational acceleration of each set of trials and the calculated value of τ_f in:

$$I = \frac{mgr - \tau_f}{\alpha_a} \tag{2.8}$$

The average linear acceleration and calculated rotational inertia values for each configuration are in Table 2.1. The Medium and High inertia configurations are roughly 10 and 20% increases over the low inertia configuration. Since the major difference between the rotational components of the two higher configurations and the low inertia mechanism are the addition of steel bolts at a radius, we can compare the expected contribution of these bolts to the calculated differences between experimental values. Modeling the bolts as a thin cylinder with mass m around the rotational axis at a radius r gives an inertia equal to $m\ r^2$. The calculated values for the 22 and 47 gram sets of bolts at a 15 mm radius gives an expected difference of 0.05 and 0.106 x 10^{-4}kg m^2 over the low inertia reel for the medium and high configurations, respectively. These are less than 15% different than experimental differences of 0.043 and 0.097 x 10^{-4}kg m^2, thus giving credence to the overall moment of inertia estimations.

Finally, the Coulomb friction torques for the remaining friction configurations were calculated using the value of medium I and the average angular deceleration values α_d of each configuration in (2.3). These calculated values are shown in Table 2.2. The medium and high friction configurations represent a 6x and 24x multiple of the internal (low) friction. The angular deceleration signals appeared nearly constant during each trial, which indicates that the friction torque in each configuration is primarily Coulomb and does not have considerable velocity dependence.

2.3.4 Flow Characterization

The system flow was measured during free flow (i.e., no everting tube) with a gas flow multimeter (5300 Series, TSI) intended for testing ventilators. This sensor was not able to be

Table 2.1: Moment of Inertia Characterization of Reel

Inertia Config	**Mass Acceleration (m/s^2)**	**Moment of Inertia (10^{-4} kg m^2)**	**Difference From Low Inertia**
Low	9.17	4.67	
Medium	8.39	5.10	+9%
High	7.59	5.64	+19%

Table 2.2: Characterization of Friction Torques

Friction Config	**Avg Friction Torque (Nm)**	**Std Dev (Nm)**	**Multiple of Low**
Low	0.0029	0.0001	
Medium	0.0174	0.0019	x6
High	0.0694	0.0041	x24

robustly integrated into the system for real time sensing during eversion experiments. An adjustable needle valve with dial readout (SMC AS3002F) was set to 8, the highest flow setting with some evident constriction. A ventilation tube roughly 1 meter long with 25mm inner diameter was affixed to the everstion snout and the input side of the flow meter while the output side was left open. In order to determine the flow rate as a function of supply pressure, the supply pressure was adjusted to values between 1 and 11 psi (6 and 75 kPa) and measured while the on/off valve was closed. The closed system pressure was measured using the SparkFun digital pressure sensor. After opening the on/off valve, the steady state flow was read from the flow meter. This was repeated for 5 supply pressures and a linear relationship between flow and pressure was found to be 1.1 gal/min per psi (0.6 L/(min kPa)) with an open system. This flow setting was kept consistent for all eversion trials.

2.4 Position Sensing

In order to provide ground truth of the everting tube's real time position, several integrated position sensing boards were quickly evaluated for their ability to reliably report the position

of the tube tip. Each sensor was mounted in the center of one end of a clear, polycarbonate pipe and an everted tube was grown toward it to a series of known positions while samples were recorded from the sensor under test. The everted tube material was held in a static position for data collection by inserting a rod through a hole on the winding knob and a hole in the wall of the reel support. The material reel was unwound and jammed before reinflating the system. Data collection at each location lasted for 5 seconds once the tube stopped growing. Both the IR proximity sensor (GP2Y0A21YK, Sharp) and ultrasonic range finder (HRLV-MaxSonar-EZ4, MaxBotix) provided unreliable data under these conditions. However, the ToF Distance Sensor (VL53L0X, Adafruit) had an average error of just 14mm average error along 470 mm (3%) of tubing growth with a 50 Hz measurement rate. Since the ToF sensor provided decent preliminary results, further efforts were made to characterize and optimize its ability to reliably report the everting tube's position.

2.4.1 ToF Sensing Improvement

Although preliminary results showed good accuracy within a single run of data collection, when a polynomial fit was applied to a group of 3 runs with the same everting material, the RMSE error was 65 mm. Experiments repeated within a light-blocking box did not improve the sensor's reliability. The ToF sensor's sensitivity to the LDPE material was evaluated by stretching several strips along a rectangular cutout in a piece of poster board to suspend them within the sensing cone - thus providing a larger and flatter surface than the everted tube tip. The board with LDPE strips was placed at known positions from the ToF sensor so that fits could be evaluated. A quadratic fit of the plain LDPE's sensor reading to ground truth position had an RMS position error of 16.8 mm over 750 mm of testing. To make the material more reflective to the IR laser, Black sharpie applied to one side of the LDPE reduced this error to 9.4mm. A strip of white plumbers tape (PTFE) suspended in front of the LDPE further reduced the error to 6.6 mm. Since a strip of plumbers tape or similar reflective material could be easily added to each of the many everting tubes in the primary experiment, further experiments were conducted to characterize and validate the sensing

improvements of reflective tube adjuncts.

2.4.2 Tube Adjunct Testing

With the expectation that opaque materials added within the LDPE tube will improve IR reflectiveness, and thus improve the ToF signal, several widths of PTFE, an attached strip of white duct tape, and pink nylon string (Fig. 2.7) were tested for repeatable accuracy. These materials were chosen as easy to integrate lab materials that could improve the relfectiveness of the tube without significantly changing the dynamics of tube growth. Other methods, such as coloring or texturing the tube surface would be difficult and time-consuming to apply evenly on all of the tubes used in the subsequent experiments. Since the everted LDPE tube becomes observably more opaque from stress and compression during eversion and inversion during and between trials, we hypothesized that crumpling a tube before mounting to the reel would help the first run of a tube perform closer to the subsequent runs and thus improve consistency among the data. Each tube configuration was tested with one tube and three trials. Each trial consisted of at least 8 measurements between 2 and 22 inches from the tip of the snout with 250 sensor readings at each point. Each of these static positions was achieved by jamming the winding knob with a rod and re-pressurizing the to 2-3 PSI. The tube's foremost tip position was measured using the scale on the clear pipe. After each trial, the tube was wound back onto the reel through inversion by twisting the winding knob.

The search for the most promising adjunct found that adding a 1/2" strip of PTFE greatly outperformed a plain tube when fitting across all trials (Fig. 2.7). There is also reason to believe that the hypothesis about crumpling a tube before its first run may also be true: the overall fit error between the plain tube and the crumpled tube nearly halved without improving the best fit. Additionally, the average fit between 1/2" PTFE and the crumpled tube with PTFE was very similar. Thus, it was hypothesized that including a PTFE strip inside the tube before eversion could both improve overall ToF accuracy across trials and that crumpling a tube before its first run would represent the best control scenario.

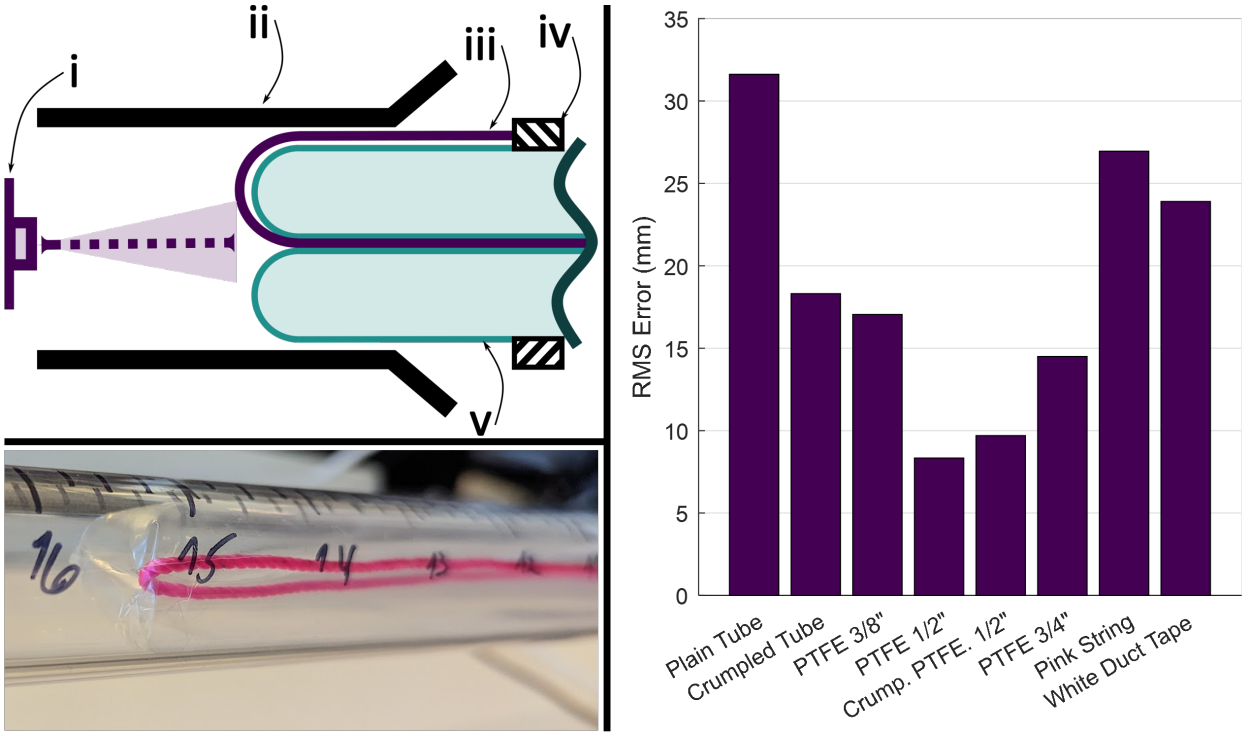

Figure 2.7: Tube adjunct testing. ***Left Top***: Diagram of everting tube with adjunct growing towards Time of Flight sensor (**i**) inside rigid growth pipe (**ii**). (**iii**) - Tube adjunct material. (**iv**) - Grounding point for tube material and adjunct. (**v**) - Tube material. ***Left Bottom***: A pink string everted within an LDPE tube to test improvements of ToF position sensing. The ground truth inch scale can be seen drawn on the polycarbonate pipe. ***Right***: Quadratic fit errors for combined trials compared between plain tubes, tubes that have been crumpled before mounting, and tubes that have added materials to improve reflectivity.

2.4.3 ToF Sensor Mapping and Statistical Analyses

A final comparison was performed between plain LDPE tubes and LDPE tubes with added 1/2" PTFE strips in order to statistically validate the effects of the addition and determine the sensor mapping to be used in the final eversion accuracy experiment. While we expect to see an effect from the presence of PTFE to reflect the ToF IR light, it could also be possible that the fit is more reliable closer or further from the sensor, or the final trial of each tube is more reliable because it is the most opaque from repeated use and therefore most reflective. This comparison included 3 plain, crumpled tubes and 3 crumpled tubes with 1/2" PTFE neatly placed within. The quasi-static measurement procedure from the initial adjunct testing was repeated for these tests. A quadratic fit of ToF readings vs manually observed tip positions was found for the collected trials of all the plain tubes and a second quadratic was found for the trials with PTFE. The RMS error for each trial from their respective fit was calculated over four even segments (142 mm) of the eversion length and used as the signal in a 2-way ANOVA test with three interactive variables: the presence of PTFE; tube length quarter; and the trial number of each run within the same tubing test sample (e.g, 1, 2, or 3).

The distributions for the RMS errors for each ToF sensor fit can be seen in Fig. 2.8. Statistical significance was found for the presence of PTFE ($p=0.0001$) and interaction between PTFE and trial order ($p=0.0065$). These results indicate that inclusion of PTFE strips not only increases overall accuracy of the ToF mapping, but they also mediate the influence of trial order on the applicability of the fit on early runs. Without the PTFE ribbon, the most reliable results may require several sacrificial trials before collecting test data. Since the distance quadrants were not found to significantly contribute to the error signal, it appears that the ToF data is accurate along the length of the tested sensing range.

The quadratic fit from the collected ToF sensor data and ground truth tube tip position from the PTFE trials group was used for sensor mapping in the primary experiment. The

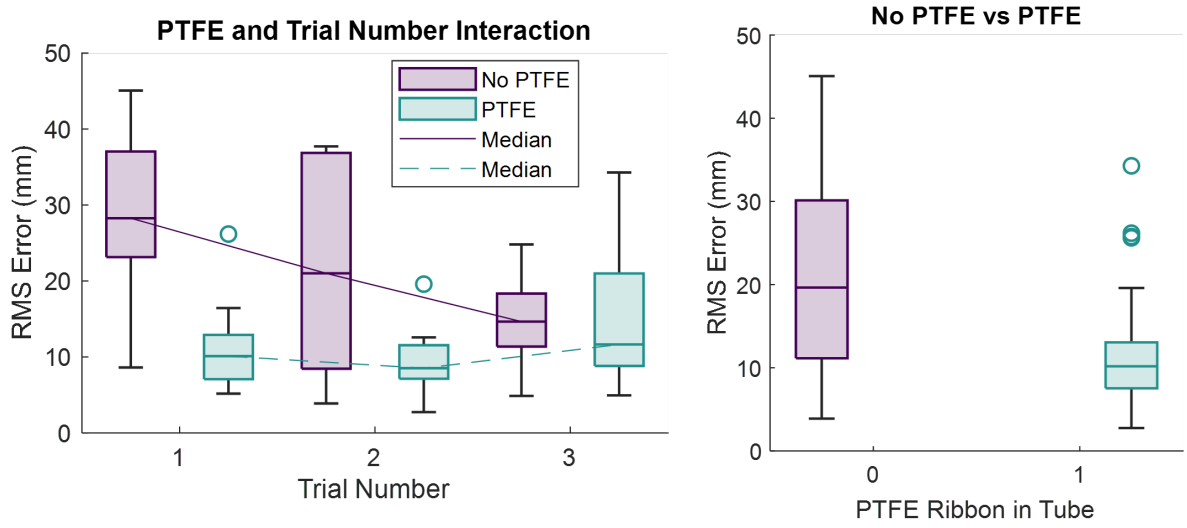

Figure 2.8: ***Left***: RMS Error of group fits compared to the presence of PTFE and the order within each set of trials (p=0.0065). The intersections of the trends of the medians indicate interaction. ***Right***: RMS Error of group fits with no PTFE and with PTFE (p=0.0001).

equation

$$x_{tof} = 3.9 * 10^{-5} {x_{tof,raw}}^2 - 0.93 x_{tof,raw} + 640 \tag{2.9}$$

maps the position of the tip, x_{tof}, growing from the everting base as a function of the raw Time of Flight signal in mm, $x_{tof,raw}$. Although the mapping is quadratic, the x^2 coefficient is only 4 orders of magnitude smaller than the x coefficient. Thus the sensor is nearly linear with a 7% slope correction. The RMS error for this fit is 13.7 mm.

2.4.4 Encoder Mapping

In order to most effectively use the reel encoder to estimate tube tip position, the changing effective radius of the material leaving the reel must be accounted for. As the material leaves the reel due to growth, the total thickness of the remaining material on top of the reel diminishes until all of the material has been removed. While the thickness of the material multiplied by the remaining number of wraps on the reel could be used to estimate the effective radius, it was observed that rewinding of the material between trials could cause

folding of the material leading to an unpredictability in the layer thickness along the length of the wrap. Thus an averaged quadratic model across different trials was calculated to encapsulate this variable diameter during trials. Encoder data collected with the ToF data was used to map the reel position to the manually observed tip position:

$$x_{encoder} = 8.1 * 10^{-3}\theta^2 + 6.4\theta - 49, \tag{2.10}$$

where the position of the tube estimated from the encoder, $x_{encoder}$, is a quadratic function of the reel angle in radians, θ. The quadratic term contributes roughly 70mm between the start and end of the tube growth. The RMS error for encoder to tip position mapping during the PTFE trials was 12.7 mm, compared to 14.1 mm with a linear fit.

2.5 Reel-Based Estimation Experiment Methods

With the goal of improving reel-based estimation of everting tube tip position during dynamic growth, the following questions were studied with three tests in this experiment:

1. Does increasing reel inertia with no additional friction affect the accuracy of the encoder estimate?

2. Does adding friction to a low inertia reel affect the reel encoder position estimate?

3. Does adding friction to a high inertia reel affect the reel encoder position estimate?

It was hypothesized that increasing the reel inertia may exacerbate the effects of reel over-spin because a reel with higher inertia will spin longer when decelerating from the same starting velocity and a higher reel inertia will require higher forces to begin spinning. By testing the friction mechanisms with reels of different inertia, we investigated whether there is a minimum friction value which minimizes reel-based estimation error for a particular reel design. Error is defined as the difference between the ToF-based position estimation and the

encoder-based estimation:

$$error = x_{tof} - x_{encoder}, \tag{2.11}$$

2.5.1 Data Collection

For each test listed above, three 54" pre-crumpled tubes were lined with flat strips of PTFE plumber's tape and wrapped onto the reel, which was then slid into the pressure vessel until aligned with the snout. The tube and PTFE were then inverted around the snout and sealed. The reel was then rewound until snug against the snout-sealed end, and the pressure vessel was closed with the end cap. After the data collection script was started and the gauge was set to 3 psi (21 kPa), the trial growth was started by quickly turning the On/Off valve. Once growth was stopped by hitting the attached end on the material reel, data collection was stopped, pressure was purged, and the material was rewound onto the reel. Each tube was tested up to four times. The number of trials and configurations for each test question are listed in Table 2.3.

Encoder and ToF position data were filtered with moving average filters (Matlab `movmean` function) of window widths 2.5 and 3 respectively. The widths of tube velocity filtering were 8 and 4, and pressure data was filtered with a window length of 7. At a sensing rate of 50 Hz, these windows range from 50ms to 160 ms. These values were determined empirically to smooth out high frequency transients without reducing the magnitude of meaningful spikes.

Table 2.3: Number of Reel-Based Position Estimation Trials

Friction Level	**Low Inertia (Test 2)**	**Medium Inertia**	**High Inertia (Test 3)**
Low (Test 1)	9	10	9
Medium	11		9
High	10		10

2.5.2 Data Analysis

In order to isolate major effects of reel inertia and applied friction, three error metrics and three growth behavior metrics were calculated for all trials. The growth behavior metrics calculated were the average pressure and average ToF-position-derived velocity during the tube growth of each trial in addition to the average growth rate during each trial. The growth rate was defined as the instantaneous velocity of the ToF-based position divided by the system pressure. Comparison of these metrics should inform the performance impacts of relative reel inertia and friction when designing an everting robot. The pressure after the growth phase of each trial was compared across trials to ensure that any effects in the growth or error metrics were not due to differences in supply pressure. After the end of tube growth in every trial, the pressure should have quickly stabilized to the overall supply pressure set at the beginning of the trial.

The steady state position error for each trial was compensated for by subtracting the average difference between the ToF signal and reel estimation at the end of each trial from the reel encoder data. This was done to offset the error introduced by not specifically controlling the initial reel position for each trial. The reel had a tendency to settle when the system was closed, especially in the low friction configuration. By minimizing this error, the effects of dynamic growth during each trial should be highlighted within the error metrics.

The error signals in each trial were calculated by subtracting the reel encoder estimation from the ToF sensor position during the growth phase of each trial. The Root Mean Square Error (RMSE) of both the tube tip position error and velocity error were calculated for each trial. The absolute maximum position error for each trial was also compared.

One-way ANOVA tests were computed with each of these metrics as continuous dependent variables and each step of inertia or friction as categorical variables. Comparisons were performed between low to medium, medium to high, and low to high to determine where statistically significant ($p < 0.05$) changes in performance were indicated.

2.6 Reel-Based Estimation Results

The issue of reel-misestimation can be seen in the representative test 1 results in Fig. 2.9. On the bottom left of Fig. 2.9, when the ToF senses the tube slowing down just before 1 second, the reel continues to accelerate to more than twice the speed of the ToF estimation. This results in a 75 mm estimation difference between the two estimations (upper left) that is corrected a second later before another spike in position mismatch due to reel overspin. The remaining trials in 2.9 demonstrate the closer alignment between position and velocity estimation with the addition of the friction mechanisms.

2.6.1 Test 1 - Increasing Inertia

The first test aimed to investigate the difference in estimation accuracy and growth characteristics with increasing reel inertia and no added reel friction. Increasing inertia demonstrated minimal effects on the estimation error between the reel-estimation and the ToF sensor and the growth metrics. Table 2.4 shows the detailed results for each metric with statistically significant ($p<0.05$) results highlighted. With an increase from 63.3 mm to 82.8 mm, there is statistically significant difference between the RMS position error of the low and medium inertia configuration, respectively. The maximum position error increased by 35% between the low and medium reel inertia trials. The low and medium supply pressures also showed a statistically significant difference of 7.6%. Neither the velocity nor growth rate were statistically different for any configurations in this test. Fig. 2.10 shows the the statistically significant error and growth metrics for test 1. The average maximum linear velocity during test 1 trials was 602 mm/s.

2.6.2 Tests 2 and 3 - Low and High Inertia Reel with Increasing Friction

The second and third test conditions added friction mechanisms to the low and high inertia reels, respectively, in order to determine the effects on estimation accuracy and tube growth. For nearly all metrics and inertia conditions, all errors decreased with increased friction. All

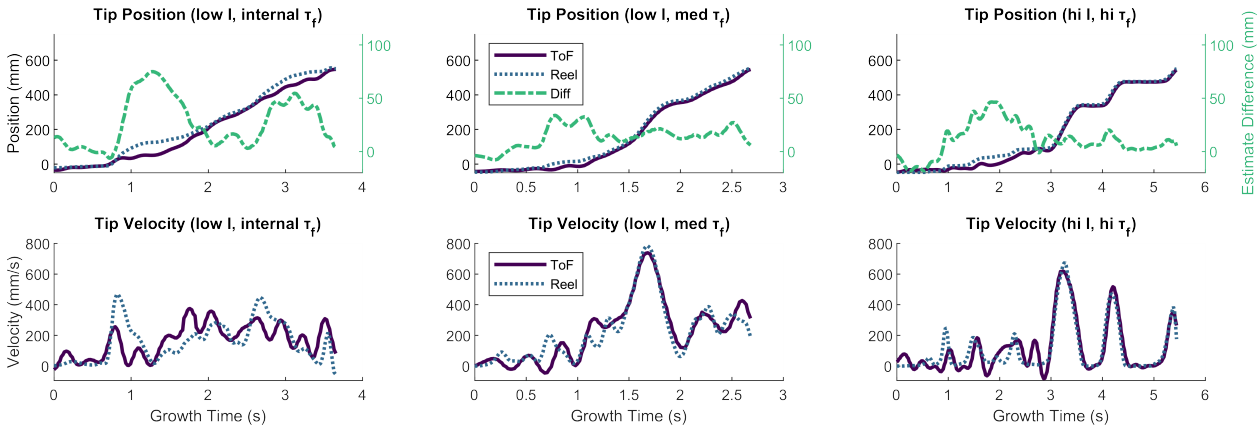

Figure 2.9: Sensor data from each test showing position and temporal difference between ToF- and reel-based estimation for better-than-average trials. The RMS position errors for the trials shown are: 36.5, 17.3, and 19 mm. The velocity RMSE values are: 108.1, 69.6, and 59.4 mm/sec.

Table 2.4: Test 1 - Rising Inertia Results

		Inertia Level						p-value (ANOVA)		
		Low (avg, std)		Med (avg, std)		High (avg, std)		L v M	M v H	L v H
Error	**Pos RMS (mm)**	63.3	23.1	82.8	22.5	62.4	47.9	**0.014**	0.240	0.9594
	Velocity RMS (mm/s)	131.6	42.2	172.0	50.9	138.8	73.6	0.269	0.257	0.7983
	Pos Max (mm)	106.5	38.6	143.9	32.0	111.5	71.5	**0.034**	0.206	0.8557
Growth	**Pressure Avg (psi)**	1.4	0.2	1.7	0.2	1.5	0.2	**0.014**	0.068	0.2867
	Velocity Avg (mm/s)	184.2	33.5	167.3	31.1	165.7	25.8	0.269	0.904	0.1926
	Growth Rate Avg (mm/s / psi)	130.11	36.62	103.05	28.58	111.25	24.30	0.089	0.498	0.1991
Condition	**Supply Pressure (psi)**	2.89	0.28	3.11	0.07	3.02	0.23	**0.023**	0.257	0.2597

error and growth metrics for tests 2 and 3 demonstrated statistical significance between the low and high friction configurations (Table 2.5). The medium friction level improved each error metric in the low inertia trials, but did not significantly impact error metrics in the high inertia tests. The medium friction mechanism reduced RMS position error by 67%, velocity error by 30%, and maximum position error by 55%. The only significant difference in error metrics between the medium and high friction trials were the velocity error in the high inertia test, where the high friction level improved velocity estimation by 39% over the medium level. Otherwise the medium and high level error metrics were statistically similar.

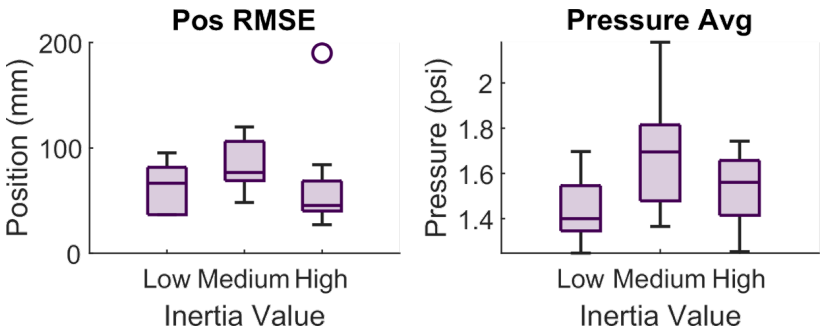

Figure 2.10: Test 1 (increasing reel inertia with low friction) error and growth results with statistical significance.

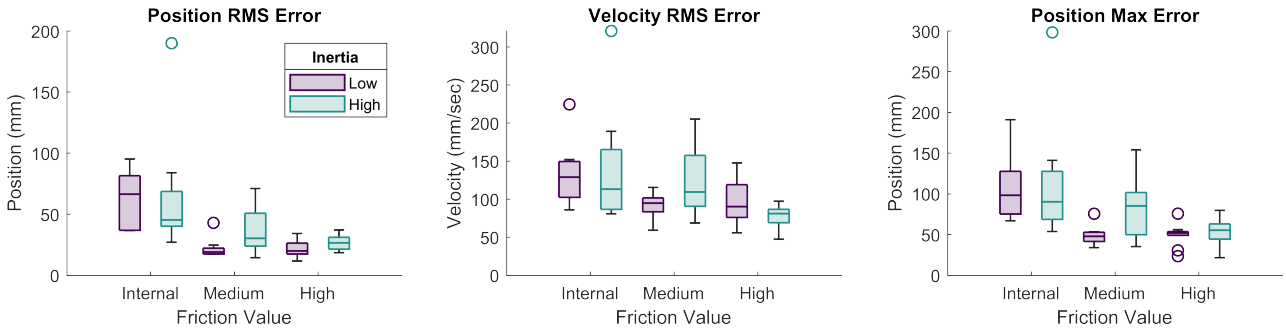

Figure 2.11: Error metric results for tests 2 & 3 - increasing friction with high and low reel inertia.

Table 2.5: Tests 2 & 3 - Increasing Friction Results

		Inertia Level	Friction Level						p-value (ANOVA)		
			Low (avg, std)		Med (avg, std)		High (avg, std)		L v M	M v H	L v H
Error	**Pos RMSE (mm)**	Low	63.3	23.1	21.7	7.5	21.7	6.6	**<0.001**	0.990	**<0.001**
		High	62.4	47.9	37.4	18.8	26.5	6.5	0.161	0.120	**0.040**
	Velocity RMSE (mm/sec)	Low	131.6	42.2	90.2	16.2	94.6	28.7	**0.008**	0.665	**0.038**
		High	138.8	73.6	126.5	47.7	77.5	15.6	0.674	**0.010**	**0.026**
	Pos Max (mm)	Low	106.5	38.6	47.8	11.5	49.5	14.2	**<0.001**	0.774	**<0.001**
		High	111.5	71.5	80.8	37.9	53.1	16.8	0.267	0.062	**0.029**
Growth	**Pressure Avg (psi)**	Low	1.4	0.2	1.5	0.1	2.1	0.3	0.640	**<0.001**	**<0.001**
		High	1.5	0.2	1.5	0.2	2.1	0.2	0.832	**<0.001**	**<0.001**
	Velocity Avg (mm/sec)	Low	184.2	33.5	197.4	23.4	100.4	35.4	0.320	**<0.001**	**<0.001**
		High	165.7	25.8	194.8	34.0	108.3	26.6	**0.049**	**<0.001**	**<0.001**
	Growth Rate Avg (mm/s / psi)	Low	130.11	36.62	133.09	26.29	52.56	24.79	0.835	**<0.001**	**<0.001**
		High	111.25	24.30	134.19	35.94	53.00	18.09	0.118	**<0.001**	**<0.001**
Condition	**Source Pressure (psi)**	Low	2.89	0.28	3.13	0.08	3.14	0.05	**0.012**	0.755	**0.011**
		High	3.02	0.23	3.05	0.12	3.13	0.07	0.801	0.083	0.189

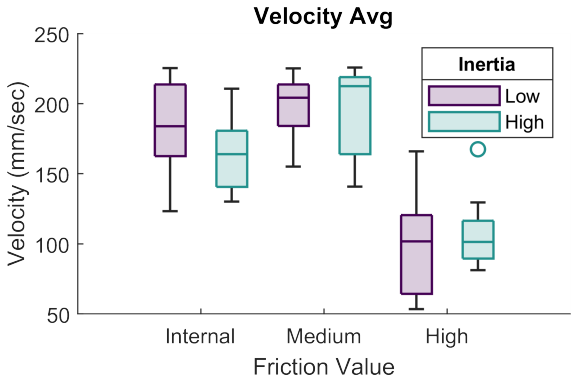

Figure 2.12: Average velocity growth metric results for tests 2 & 3 - increasing friction with high and low reel inertia. Results for the remaining growth metrics are similar to the velocity results.

Fig. 2.11 compares the error metric results between friction levels and reel inertia.

Nearly all growth metrics were statistically indistinct between low friction and the medium friction device. In the high inertia scenario, the average velocity increased by 17% (Fig. 2.12) without a significant change in source pressure. The high friction device increased the required pressure by 50% in both inertia configurations and reduced average velocity of the medium friction device trials by the same amount. The source pressure for the medium and high friction configurations of the low inertia trials was 8% higher than the low friction trials.

2.7 Discussion

2.7.1 Reel Characterization

The system characterizations of the eversion reel and its experimental configurations demonstrate a straightforward method of evaluating expected behavior of the system and relative changes between the configurations. This is especially useful for estimating the inertia of 3D printed components where the exact printing output may not be available for mass property simulation in CAD software.

Coulomb friction may not describe the full contributions of the applied reel friction on the dynamics of the reel under all conditions At zero or extreme velocities, static or viscous friction may present different friction magnitudes. However, the evaluated Coulomb friction was seen to be fairly constant in the range of angular speeds in the growth experiments, and any unmodeled friction effects are not obvious in the position estimation results. These tests were also sufficient to indicate the relative difference between each applied friction level and these levels were distinct enough to draw conclusions about the effects of increased friction on eversion growth and position estimation. More detailed description of the reel dynamics would require analysis of the static friction of the reel and the effects of wear on the friction surfaces.

2.7.2 Pneumatic System

Even though the system's no-load air flow was observed to have a linear response to supply pressure, further analysis of the flow rate's stability in response to changes in resistance would be needed to accurately estimate the flow conditions during eversion trials. If the flow rate during eversion were similar to the open circuit flow tested, the rough average of 3 psi measured supply pressure at the end of each trial would correspond to 1.8 L/min flow. This sustained flow would correspond to a growth rate of roughly 60 mm/sec for the 25 mm tube as a function of changing volume. This is about 30% of the average velocity seen in the eversion trials without high friction. Thus, the system appears to be flow limited,

partially explaining why the observed velocities tend to spike and fall. Once the pressure in the system grows above the minimum eversion pressure, the tube starts to grow and the system pressure begins to fall as the flow is insufficient to compensate for the increasing tube volume. Growth slows down and stops when pressure falls below a minimum required to sustain growth. This cycle is especially evident in the Test 3 high friction example of Fig. 2.12 (right), where growth velocity quickly spikes and stops several times. The high friction requires a higher minimum eversion pressure to overcome, leading to a higher initial velocity once overcome, with a peak velocity corresponding to an increase in volume ten times greater than the supply flow.

2.7.3 Position Sensing System

Results Summary

The optical ToF based tube tip sensing system was significantly improved by the addition of PTFE tape into the everting tube. This increase in sensitivity may be limited to LDPE as a tube material, and may not be needed for other common everting tube materials, such as nylon or TPU, as these materials IR reflectance may be better than LDPE for accurate sensing.

Limitations

The accuracy of the Time of Flight sensing during the growth estimation experiment may have been limited by two experimental factors: the method used to fit the sensor data to tube position and the effects of the PTFE tape on tube growth. The ToF-position fit is based on data collected while the position of the tube tip was static and the pressure was fairly constant at the level of the supply pressure. During growth, however, the tube would rarely be at the full supply pressure and would have a constantly changing shape at the front as new material is everted to the outside. The shape of the PTFE tape may also change during growth and may cause the tube to bunch up on one side by partially constricting growth

when the tape's length is shorter than the tube's length.

Both of these potentially confounding conditions, quasi-static modeling and the influence of the PTFE tape, are not likely to affect the results of the growth estimation experiment as described. If the quasi-static fit for the ToF data were inappropriate for the dynamic growth, we would not expect to see such robust minimization of the error between the reel encoder and the ToF data caused by the friction devices, especially with peak velocities approaching 1 meter per second. Moreover, the primary results for this work are based on relative calculations between tests where the sensing conditions are the same. Any systematic error introduced by these conditions should be present in all tests and does not prevent statistical significance for many of the tests. Even so, the quasi-static fit for the ToF with the PTFE adjunct had an RMS error of 13.7 mm, which limits the ability to assess the absolute accuracy of the reel estimation beyond this amount, and it may be true that the fit has worse performance with dynamic tube growth at lower pressures. The best RMS error during test 2 was 21.7 mm and this may be close to the expected accuracy of the ToF sensor during these experiments. It would take a more accurate ground truth measurement to determine the true accuracy of the reel-based estimation with the friction pads.

The PTFE tape likely affected the dynamics of tube growth. It was noted that tension from the tape could limit growth for part of the tube. This tension certainly could have slowed the growth when encountered and may have caused more instances of deceleration or stopping than would normally be seen with a plain tube (i.e., no tube adjunct). Thus, in addition to improving the accuracy of the ToF estimation, the PTFE tape may have helped to simulate more irregular conditions that everted tubes may be used in, such as environments with irregular widths or obstacles that may cause growth to slow momentarily.

2.7.4 Eversion Accuracy Experiment

Test 1

As laid out in Section 2.5, the guiding question for the first test is whether the reel inertia changes the accuracy of the reel encoder estimate. If this were so, we would expect a significant accuracy difference between the low and high inertia configurations, but see none. While there is a significant position accuracy difference between the low and medium inertia reels, there is also a significant difference in average pressure and supply pressure in only these conditions. It is reasonable to believe that the increase in error for the medium inertia reel is due to the nearly 10% increase in supply pressure and 20% increase in average growth pressure leading to dynamics not seen in the low or high configuration. It is interesting that the increased pressure in the medium configuration did not lead to higher average velocity. The 20% increase in reel inertia from the low to high configurations does not seem to have any effect on accuracy of the reel encoder estimate or any of the other error or growth metrics. A larger difference in inertia or different metrics may be necessary to evaluate the effects of reel inertia on eversion.

Tests 2 and 3

The guiding question for tests 2 and 3 are whether friction pads are able to significantly increase the accuracy of the reel-based estimation of the tube tip for the low and high inertia reels configurations. Not only do the friction pads increase tip position accuracy by up to 67%, they also reduce velocity error and maximum position error by up to 44% and 52% respectively.

From the results of tests 2 and 3, it seems that there is a minimum amount of friction that must be applied based on the inertia of the reel. While the medium friction level was able to significantly improve estimation accuracy with the low inertia reel, it did not significantly improve accuracy with the high inertia reel. The high friction level was able to significantly improve the estimation with both levels of reel inertia, but this level of friction also signifi-

cantly impacted the growth of the tube. The high friction level lowered the average velocity of the tube by 46% and increased the average pressure by 50%. If it is desired to increase estimation accuracy while minimally affecting tube growth, the medium level of friction is a good amount for the low inertia reel, but a level of friction between medium and high would be preferable for the high inertia reel.

2.7.5 Relative Deceleration

The theoretical effects of inertia and friction can also be demonstrated by calculating the amount of time that it takes the reel to come to a stop after the tip comes to a stop. This stopping time and the associated length of material unreeled can indicate the scope of the issue when applied to a new reel design with a desired linear velocity. Following Section 2.3.3, the time it takes to reach zero angular velocity, t_{stop}, due to Coulomb friction can be described by:

$$\omega = 0 = \omega_0 - \alpha_d t_{stop}, \tag{2.12}$$

where ω_0 is the reel's angular velocity when it starts to slow down and α_d is the deceleration, which remains the same as described in (2.3):

$$\alpha_d = \frac{\tau_f}{I}. \tag{2.13}$$

Therefore, the time that the reel takes to slow down from ω_0 to zero is:

$$t_{stop} = \frac{\omega_0}{\alpha_d} = \frac{\omega_0 I}{\tau_f}. \tag{2.14}$$

The rotational change, $\Delta\theta$, in that time is:

$$\Delta\theta = \frac{1}{2}\alpha_d t_{stop}^2. \tag{2.15}$$

Multiplying $\Delta\theta$ by the reel radius gives a theoretical length of unreeled material after eversion stops. Table 2.6 shows the calculated time required for the reel to stop spinning and the length unspooled in that time for the average maximum velocity of the test 1 trials among all friction and inertia configurations. This estimate does not include the inertia of the material on the reel or any resisting torque from the material during deceleration. Instead, these estimates highlight a method for understanding and designing a reel and friction mechanism for an eversion system where real-time tip position may be important.

Table 2.6: Reel Stopping Time and Distance From 600 mm/s (9.5 rev/s)

		Reel Inertia Configuration					
		Low (s, mm)		**Med (s, mm)**		**High (s, mm)**	
Friction	**Low**	0.910	273	0.993	298	1.101	330
	Medium	0.152	45	0.166	50	0.183	55
	High	0.038	11	0.042	12	0.046	14

As expected from the relative friction values, the time to stop the reel with the medium friction mechanism is six times less than without it. In Table 2.6 the reel stopping times for this mechanism in tests 2 and 3 are 0.152 s and 0.183 s, respectively. The stopping distances of 24 and 55 mm are slightly less than one full rotation of the 63 mm reel circumference. The medium friction level did not improve the estimation accuracy of the high inertia reel but the high friction level did, thus the necessary stopping time for improving estimation must be between 0.183 and 0.046 seconds. This friction level between medium and high should be able to decrease the estimation errors while exerting less of an effect on the growth behavior. It is reasonable to believe that achieving a stopping time close to 0.152 sec may be sufficient to significantly decrease positional estimation error, as this stopping time was sufficient for improving the low inertia reel estimation accuracy. This would be a decrease of 17% in stopping time, requiring a similar increase in friction torque.

2.7.6 Implications for Tube Growth Model

The accepted model for tube growth balances the growing force at the front of the tube against the yield force of the system, the rate dependent losses, and path dependent friction terms. In reel dependent devices that have been modeled in the literature, the effects of reel inertia and reel friction have most likely been lumped into the effects of yield pressure and growth rate losses, to the extent that they have impacted growth. Static friction occurs at zero velocity and would be required to be overcome before eversion could start, much like the yield pressure required to overcome material losses at the tip. Inertial acceleration of the reel and Coulomb friction could be grouped into the viscoplastic losses, even though they are not technically velocity-dependent. An extended version of (2.1) could account for reel inertia and friction:

$$\frac{1}{2}P_{grow}A = \frac{1}{2}P_{yield} * A + (\frac{1}{\varphi}v)^{\frac{1}{n}}A + \frac{(I\alpha + \tau_f)}{R_{reel}}, \tag{2.16}$$

where R_{reel} is the radius of the reel plus the effective thickness of the remaining reeled material. The new terms in parentheses are conditional on the tail being taut between the tip of the tube and the reel. Additionally, the friction torque would depend on whether the reel is static or in motion.

We can investigate the relative magnitudes of the inertia and friction terms in the accuracy experiments. The average acceleration of the reel during test 1 trials was $3.5\frac{rad}{s^2}$, and the average pressures during low and medium friction trials was 1.4 psi (9.7 kPa), while the average pressure during high friction trials was 2.1 psi (14.5 kPa). The resulting reel acceleration and friction forces on the growing tip during these conditions are shown in Table 2.7. The reel provides a small load on the supplied growing force at 6% and a 20% increase in reel inertia in the high configuration would lead to a 7% load. This indicates that a larger increase in inertia would be needed to see a significant impact on tube growth. However, the friction loads grow from 11% and 66% of the growing force in low and medium configurations to well over 100% with high friction. Even with roller bearings, the low friction design has

more of an impact on growth than the reel inertia.

Table 2.7: Inertia and Friction Force During Trials

		Force Term in eq. (2.16) **(N)**				
Avg Pressure (psi, kPa)		**Growth Force**	**Low Inertia**	**Low Fric.**	**Med Fric.**	**High Fric.**
1.4	9.7	2.5	0.15	0.27	1.66	
2.1	14.5	3.7				6.6
% of Growth Force			6%	11%	66%	178%

The high values of the medium and high friction forces compared to the growing force likely indicates that calculated friction torques are overestimated. An increased load of 50% from low to medium should elicit a significant change in growth behavior, but none was seen in tests 2 and 3 between low and medium friction. Inaccurate estimation of the reel deceleration could be due to the estimation of reel deceleration, and this would cause inaccurate estimation of the absolute friction torque values. Calculations of the average reel deceleration were highly sensitive to length of the filter window due to low sensing frequency and noise introduced by double derivation of the encoder data. Higher frequency testing of reel deceleration would decrease the analysis's sensitivity to filtering.

2.7.7 Implications for Future Designs

The results of this work have implications for the design of everting tube systems in terms of tube growth and estimation accuracy. The growth of everting tubes is affected by the mechanical design of the material reel and by the capabilities of the pressure system. Some friction can be beneficial to increase the accuracy of reel-based estimation, especially if there is an expectation of velocity variation in the application. If the flow is insufficient to sustain the volume growth of the everting tube, then there is a greater chance of slowing and stopping during growth, although additional experimentation is still required to characterize this effect.

As mentioned in the introduction, a slight growth-resisting torque could be applied with a motor in order to decrease the difference between reel position and tip position. If the goal of the design is to allow for eversion with as little resistance as possible, a motor with low internal friction and low inertia would be desirable. A motor that increases the reel system inertia by 20% is unlikely to affect growth during conditions similar to those of this work, but special care should be taken to minimize the increase in internal friction. A lower reel friction gives more of an envelope for controlling the resisting torque to a level that can increase accuracy without affecting growth.

2.8 Conclusion

Inertia of the material reel during dynamic everting tube growth can cause overestimation of the tube's position when measured with a reel mounted encoder. This effect can be overcome with a friction device that limits reel over spin when tube growth slows down. While the inertia levels used in these experiments did not show an effect in the growth or estimation metrics evaluated, it was shown that the friction necessary to improve estimation accuracy increases with reel inertia. It was also shown that increased reel friction requires higher system pressure and decreases average growth velocity. Furthermore, we suspect that the pneumatic flow of our system limited tube growth and exacerbated the tendency for tube growth to slow down and stop during the experiments.

The experiments and analysis in this chapter contribute the following:

1. A description of reel-based position error during dynamic tube growth and experimentally proven solution for reducing this error,

2. Real time, mm-scale position sensing for tube tip estimation using a Time of Flight sensor and PTFE adjunct, and

3. A method for characterizing everting tube rotational inertia and friction.

4. An extended everting tube growth model that accounts for physical reel characteristics.

Further investigations into everting tube behavior and design could focus on: simulating and validating an improved everting tube growth model; more accurate ground truth position sensing; or a thoroughly characterized reel torque system. An improved everting tube model would include terms for mechanism-specific characteristics, such as reel inertia and friction. Depending on the system, a flow-based model may be necessary to accurately estimate the growth behavior of an everted tube. Time of Flight sensing was shown to be useful as an external, real-time position sensor, especially for a system without a reel encoder, but it required the addition of a PTFE strip in order to improve sensing performance with the LDPE material. ToF may be more effective with other tube materials and may be more accurate during growth than described if compared to a camera-based ground truth. The friction mechanisms used in these experiments achieved the goal of reducing reel-estimation error, but could benefit from a redesign that prioritizes frictional consistency and robustness to wear.

Chapter 3

CHARACTERIZING AN EVERTING TUBE'S WORKING CHANNEL FRICTION

Research Aim 2: Demonstrate a method for estimating the static and dynamic friction between an everting tube and a working channel with the central lumen of the tube.

3.1 Introduction

A desirable feature of an everting introducer is the ability to insert a working channel concurrently with the leading edge. However, since the tip of an everting tube moves forward at half the rate of the inside material, a channel locked to the inside of the tube would move at twice the rate of the everting tip, quickly rendering it useless as an introduction sheath. Thus, sliding must occur between the inside of the everting tube and the working channel to maintain equivalent tip rates. The minimum pressure required to slip along a core depends on the friction between the everting tube and the working channel as well as the cross-sectional tip-area lost to the core (reducing net eversion force).

This work will focus on modeling the interactions between an everted tube and a flexible robot that is independently co-deployed within the inner lumen of the everted tube. Such a robot will be able to take advantage of the everted tube's ability to navigate constricted environments with minimal disruption while also allowing for protected delivery of active or passive tools through a lumen of the everted tube. The physical variables of interest will be the frictional forces and the corresponding increase in Minimum Eversion Pressure (MEP) required to initiate or continue eversion. While the recent works of [64] and [69] present a significant step forward in understanding and modeling the interactions between an everting tube and an inner working ch, this chapter focuses on a novel method for determining the

coefficients of friction and validating the physical modeling of this interaction.

Most everted robots shown in the literature deploy sensors or actuators that are built into the tube or pushed along at the tip of the tube. While this method of sensor deployment has many uses, it tends to sacrifice two major advantages inherent in everted growth: 1) non-sliding contact with the environment during growth, and 2) the ability to grow into areas that are narrower than the nominal diameter of the everting body.

The modeling of everted tube interactions with a flexible catheter in the MAMMOBOT robot [30] was limited to a description of the extra "grip" that the everted tube exerts on the internal catheter when trying to deploy each at the same relative velocity. This friction was overcome by quickly switching between four modes during insertion: 1) increase pressure in the everting tube, 2) advance the everting tube and catheter at the same rate for a small distance, 3) depressurize the everting tube, and finally, 4) retract the catheter by half the inserted distance. This method takes advantage of the additional friction on the working channel when pressurized and decreases the effective friction when retracting. A reverse of this method is used while retracting the catheter. While the authors were able to use this control scheme for teleoperation of MAMMOBOT, a deeper understanding of the physical phenomena may allow for more elegant control methods or state estimation of the everted tube.

Another method to use an everting tube to advance a camera tethered through the working channel is presented in [70]. In this method, the new everting material is folded along its main axis so that it can be efficiently bunched along a hollow tube, which is where the teher for the camera enters into the working channel. The folded material is then fed forward to allow tube growth. Air pressure within the working channel serves to limit the contact area between the camera tether and the working channel. The folding method presents a very interesting alternative to the linear actuator required for linear eversion robots such as MAMMOBOT, where the linear actuator length may be a limiting factor.

In [64], Girerd et al. expand on the origami folding idea of [70] by placing the folded new material on a short tube that travels at the front of the everting tube. This method allows

for much longer everting tubes with working channels at the expense of a rigid cap at the growing edge of the everting tube. Girerd et al. also continue the work of Larrea et al. [63] to highlight design limits of everting tubes with working channels. Their extension of the Larrea modelling is combined with reasonable estimations of engineering values, but does not specifically seek to determine these experimentally.

3.1.1 Hawkes' Model of Everted Tube Growth

The extending response of the everting tube robot due to pressure is very similar to plant root growth [71, 72] where a minimum internal cell pressure is necessary to initiate tip-wise growth, after which the growth rate increases exponentially. Inspired by this plant analogy, Hawkes et al. [4, 8] propose a growth rate model of a simple everting robot consisting of a pressure vessel, pump, and reel of tubing as a function of pressure:

$$r = \varphi(P - Y)^n \tag{3.1}$$

where φ is the extensibility (viscosity^{-1}), P is the pressure, Y is the yield pressure, and n is a power term close to 1. Rate measurements of a robot taken at various pressures allow for these terms to be determined [4].

The quasi-static model that governs a general everting robot, as presented in [4, 8] is:

$$\frac{1}{2}PA = F_y + (\frac{1}{\varphi}r)^{1/n}A + \mu_L L_s + \sum_{L_c} Ce^{\mu_\kappa \kappa L_c} \tag{3.2}$$

where P is the applied pressure, A is the area at the tip, F_y is the yield force, r is the rate of growth, μ_L is the coefficient of friction per unit length, L_s is the length of all straight sections, L_c is the length of a curved section, C is a fitting term, κ is the section's curvature (radius^{-1}), and μ_κ is the coefficient of friction due to curvature. The applied pressure force, PA, is divided by two because only half of the applied force applies tension to the tail of the tube, while the other half applies tension to the static outer material of the tube grounded

to the pressure vessel base. The terms of this tip-force model are described below.

F_y - Yield Force Dependence

An everting tube will only start to grow when the pressure force at the front rises above a certain level, known as the yield force. Below this force, the tube will not grow.

The experiments of [4] showed that this dependency remains constant over extension and is independent of the environment. First, a robot body was extended through a gap lined with a variety of materials (Fig. S1A [4]), with pressure sufficient for minimal speed. There was no relationship between material and pressure, thus yield pressure is independent of environment. Second, bodies of varying diameters were grown into a slanted gap at just over yield pressure. The robot stopped due to the decreasing size and this gap was measured and the pressure was increased to restart motion. The pressure was proportional to the inverse of the stopping area (Fig. S2A), thus $P = F_y * \frac{2}{A}$ when rate, length, and curvature approach zero.

r - Rate Dependence

Hawkes et al. determine that achieving a higher growth rate requires additional pressure, as represented by the viscosity term, $1/\varphi$, multiplied by the growth rate, r. The exponential term, $1/n$ is a small correction term near 1.

The authors hypothesize that the pressure loss due to velocity is caused by material deformation at the tip and not due to fluid flow. Changes in diameter had no effect on rate and it was calculated that significant pressure drops in the robot body would require extraordinary lengths and extension rates.

L_s - Length Dependence

It was discovered that the length of the growing tube, L_s, had an effect on the force-balance of (3.2), which was deemed to be linear with a length coefficient μ_L.

To determine if there was a maximum length achievable at a certain pressure, a 10cm spool of tubing was extended at 20 kPa to a length of 70m. This experiment was repeated at the same pressure while the robot passed through a small gap at the beginning of growth and it still achieved max length. Thus, even with an expansion factor of 7000 there is little effect of length on pressure required. However, another experiment was conducted to determine the internal friction contributions along the length of the body. The inner diameter of a rigid tube was lined with robot material and the tube was mounted to a force sensor. A motor was used to pull another piece of robot material through the tube at a constant rate while the shear force reaction was measured. A linear relationship was found between the shear force and the length of the body material in the rigid tube.

C, L_c - Curvature Dependence

The curvature dependence was modeled as a sum of of individual capstan losses, which relate cable tension to friction around a capstan or drum as a function of the number of wraps, L_c, at a given curvature, κ. The constant C is a coefficient to fit the exponential term, and μ_κ is the coefficient of friction due to curvature.

To determine the coefficient values, an experiment similar to yield pressure dependency was conducted. A robot was extended at a minimal pressure into a constant width, constant radius path until it was unable to continue moving. Three curvature values were tested and the pressure to length relationship was found to be exponential with the exponent increasing with the curvature.

3.1.2 Classical Friction Model

The classical model for friction between two materials in contact described in [73] is:

$$F_f(v) = F_C + (F_s - F_C)e^{-|v/v_\sigma|^{\delta\sigma}} + F_v(v), \tag{3.3}$$

where total friction, F_f, is velocity (v) dependent and a sum of: Coulomb friction, F_C,

also known as dynamic or sliding friction; static friction, F_s; and the velocity dependent viscous friction, F_v. The exponential term is a smoothing term, known as the Stribeck effect, between Static and Coulomb friction levels. For simplicity, the Stribeck effect will be ignored in this chapter. The contributions of each term can be seen in Figure 3.1. Coulomb friction, also known as kinetic or dynamic friction, is linearly related to the applied (normal) force, F_N, by the Coulomb coefficient, μ_c:

$$F_C = F_N \mu_C. \tag{3.4}$$

Static friction occurs at zero velocity and its coefficient often has a higher value than Coulomb friction:

$$F_s = F_N \mu_s. \tag{3.5}$$

This equation describes the limit of the static friction force, as any force greater than this limit will cause relative motion and the friction in opposition to the applied force will decrease to the level of the Coulomb friction. When the applied force is less than the static limit for a given normal force, the friction force will be equal and opposite to the applied force.

Viscous friction models the resistance to motion similar to an object traveling through fluid, where drag increases with velocity:

$$F_v = F_N \mu_v v. \tag{3.6}$$

Both μ_s and μ_C are dimensionless, but μ_v is the inverse of velocity.

A simplified version of this model where the Stribeck effect is ignored, can be split into static and dynamic conditions:

$$F_f(v) = \begin{cases} F_s, & \text{if } v = 0, \\ F_C + F_v(v), & \text{if } |v| > 0, \end{cases} \tag{3.7}$$

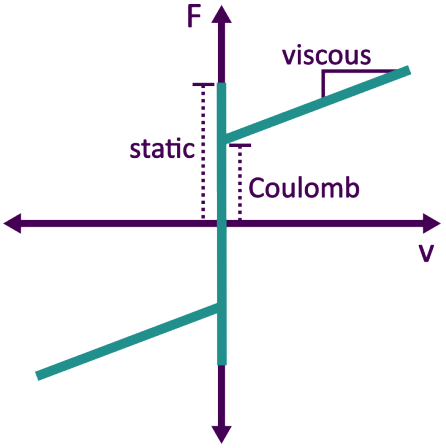

Figure 3.1: Components of the general friction model. This illustration ignores the Stribeck effect, which models a smooth transition from static to Coulomb (dynamic) friction.

3.1.3 Contributions

In order to inform the eventual design of an everting tube with a working channel, engineering values for physical phenomena must be determined. In this chapter, experimental models and procedures for understanding tube-channel interactions and determining coefficients of friction will be presented to aid in future design work. The experiments and analysis in this chapter present the following:

1. measuring length dependence of minimum eversion pressure

2. estimating static friction of an everting tube over a working channel without a force sensor

3. measuring minimum eversion force with a force sensor

4. estimating dynamic friction of an everting tube over a working channel with a force sensor

5. demonstration of the effects of lubricant on the static and dynamic friction between an

everting tube and a working channel

3.2 Methods

In order to investigate the friction properties of an everting tube growing over a working channel, three experiments were conducted to evaluate the behavior of an everting tube's

1. minimum eversion pressure,

2. coefficient of static friction, and

3. coefficient of dynamic friction.

These experiments specifically investigate the interaction between LDPE tubes and stainless steel working channels with and without water-based lubricant.

3.2.1 System

The eversion system used for these experiments is similar to that of Chapter 2 with an updated digital pressure regulator and a force sensor. A schmetic of the robotic system, with pneumatic, mechanical, electrical, and software components, can be seein in Figure 3.3. Although a working channel is more easily integrated into the design of a linear eversion base, like that of [30], a reel-based eversion system is used in this work to isolate the effects of adding a working channel to a previously studied experimental system. An analog of a working channel mounted on a force sensor is placed in the growing path of the everting tube, which is constrained by a clear pipe. When growing over the channel, the force sensor measures the interactions between the channel and the everting tube material. The conceptual equivalence of the linear eversion over a working channel and the experimental setup is demonstrated in Figure 3.2.

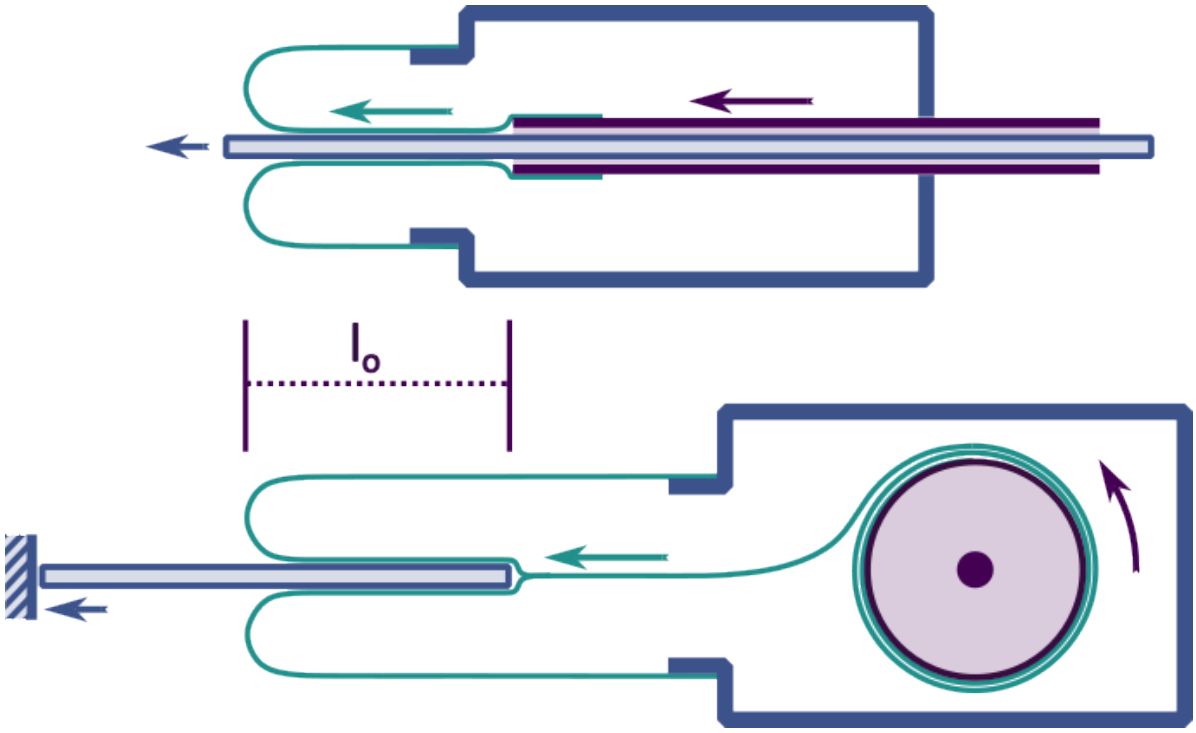

Figure 3.2: Comparison of linear eversion robot with working channel and the experimental setup. ***Above***: A simple linear eversion robot where the central working channel is fed forward at half the rate as the everting tube material. This disparity in velocity causes sliding of the tube material along the working channel. ***Below***: In the experimental setup, the working channel is mounted to a force sensor in order to measure the interaction forces. This setup allows for observation of the overlap length, l_o.

Eversion System

The low inertia reel with medium friction mechanism characterized in Chapter 2 was chosen for these experiments in order to maximize position estimation accuracy with a known load. The contents of the eversion pressure vessel are as described previously. The 1" LDPE material in these experiments was used without pre-stressing and without an opaque adjunct, as the optical ToF sensor was not used for position feedback.

Pneumatic System

An electro-pneumatic digital air pressure regulator (SMC ITV2010-04N2N4) was used in order to provide consistent air pressure with small, digitally controlled increments. This regulator provides closed-loop digital pressure regulation, which can quickly adjust for the changing volume of the everting tube. Controlling the pressure via analog output from the Arduino allows for temporal correlation of tube behavior with changes in control pressure. A transistor circuit was designed to provide the 4-20 mA control current from a Pulse Width Modulated (PWM) analog output from the Arduino, details of this circuit and associated code can be found in Appendix A. The pressure range for the regulator was set from below the expected minimum eversion pressure to just below the average burst pressure of the everting tubes: 1 psi to 5.8 psi (6.8 to 40 kPa). Another pressure regulator was placed between the high pressure tank and the digital pressure regulator in order to prevent damage to the digital pressure regulator by limiting it's source pressure to 30 psi. When this source pressure dipped, the tank was refilled to roughly 60 psi.

The working channels studied in these experiments are 6" long (150 mm), solid cylinders made of 303 Stainless Steel with a rounded tip. Steel was chosen for its rigidity and because stainless steel is a common material for rigid medical tools that may be inserted through everting tubes. Since the everting tube is pushing on the working channel in this configuration, buckling of a more flexible material was a concern. The working channels are mounted in 3D printed PLA blocks which allowed for quick swapping onto the force sensor

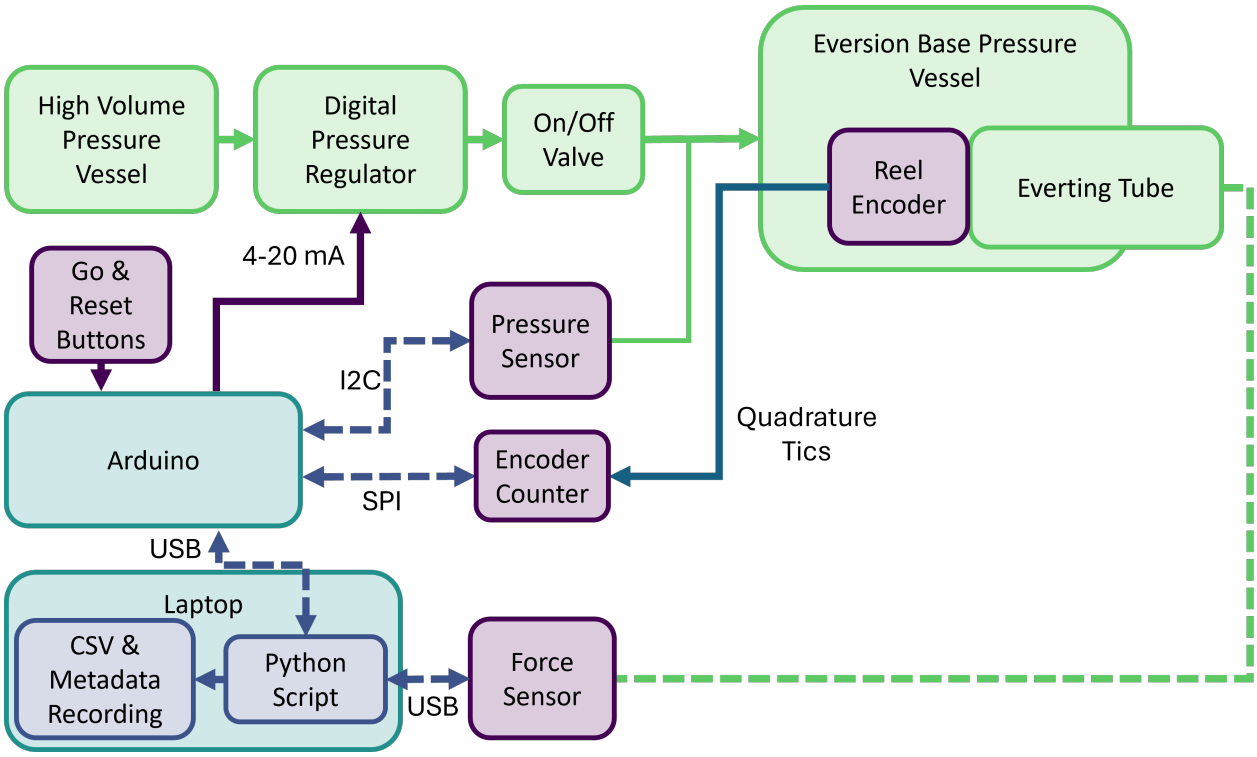

Figure 3.3: Schematic of the eversion robot and data collection system.

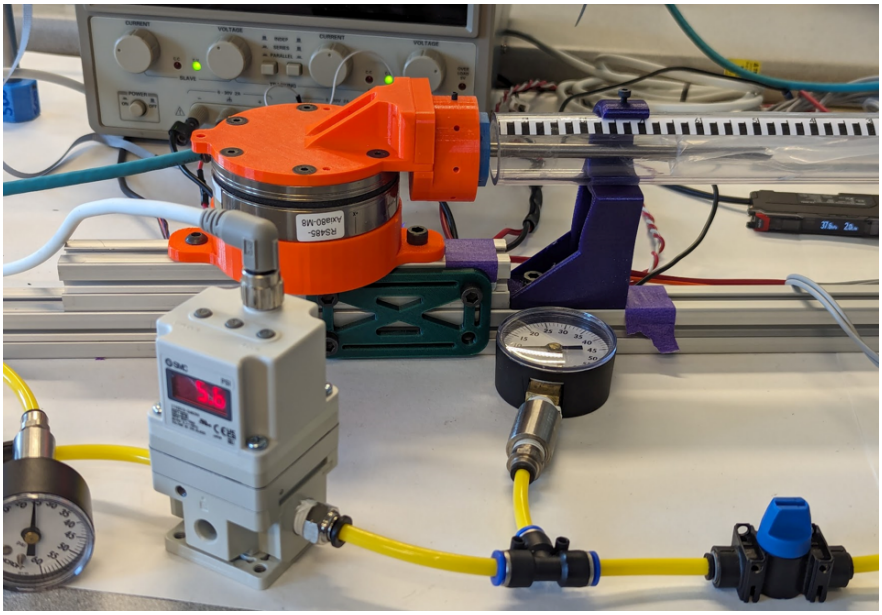

Figure 3.4: Force sensing end of experimental setup. Seen in the foreground (left to right) are the high pressure source gauge, digital pressure regulator, eversion system gauge, and the on/off valve. In the middle ground is the force sensor with $\frac{1}{4}$ inch (6 mm) steel working channel inserted into the growing tunnel.

adapter. The force sensor is mounted to the 8020 experiment frame and can be loosened to slide the working channel out of the growth pipe. Sliding the force sensor mounting rail against the growth pipe support ensured a consistent tip position for the working channel when swapped. The working channel and force sensor setup can be see in Figure 3.4, along with the air pressure regulator.

Data Collection

A python script was used to label data files and collect concurrent USB serial data from the Arduino and force sensor. The collection rate was 50 Hz and was stored in CSV files with metadata describing the conditions for each trial.

Force data from the working channel was collected with an ATI Axia80-M8 6-axis force/-torque sensor designed for lightweight industrial robots. The X and Z axes (along the plane of

the mounting plate) have a calibrated range of ± 75 N and the Z axis has a range of ± 245 N. The USB serial interface provided 16 bit data. Initial testing found that the Z axis had significant, difficult to model drift over the time scale of an experiment, and the larger range of the axis meant less resolution. The X-Y axes did not exhibit noticeable drift over the time scale of the experiments. Thus, the force sensor was mounted horizontally. The sensor was placed in 'robot' mode, where up-to-date data could be requested at regular intervals in response to an 'r' character from the python script. The design of the working channel interface plate was iterated in order to optimize stiffness. The custom python class that allows for collection of serial data is available publicly (`https://github.com/awlewi/ati_m8_serial`).

A positioning scale was taped to the force sensing end of the growth pipe so that overlap positions could be visually measured using high contrast markings at 1/8" (3.2 mm) intervals.

A Keyence air flow sensor (FD-EPH7) was included in the system, but this data was not used in the analysis within this chapter. Analog current output from the flow sensor was measured by the Arduino.

Autonomous Eversion Control Software

In addition to supplying consistent source pressure during eversion experiments, the digital pressure regulator also allowed for automation of static-to-dynamic threshold searching during experiments. This was generally achieved by autonomously increasing the control signal for the pressure regulator at regular time intervals until a change in the reel encoder position exceeded a certain threshold. A 3-state state machine was designed that allowed for different behavior depending on the phase of the experiment. A flowchart of the state machine can be seen in Figure 3.5.

The three states are: `Waiting`, `Initial Growth`, and `Auto Step`. No action was taken during `Waiting` and pressure was kept at the minimum control value. `Initial Growth` refers to the initial growth of the tube from the pressure vessel to the working channel. During this state, the aim is to evert to the distal end with the minimum possible pressure and no manual data observation is required. Static and Coulomb data was collected during the

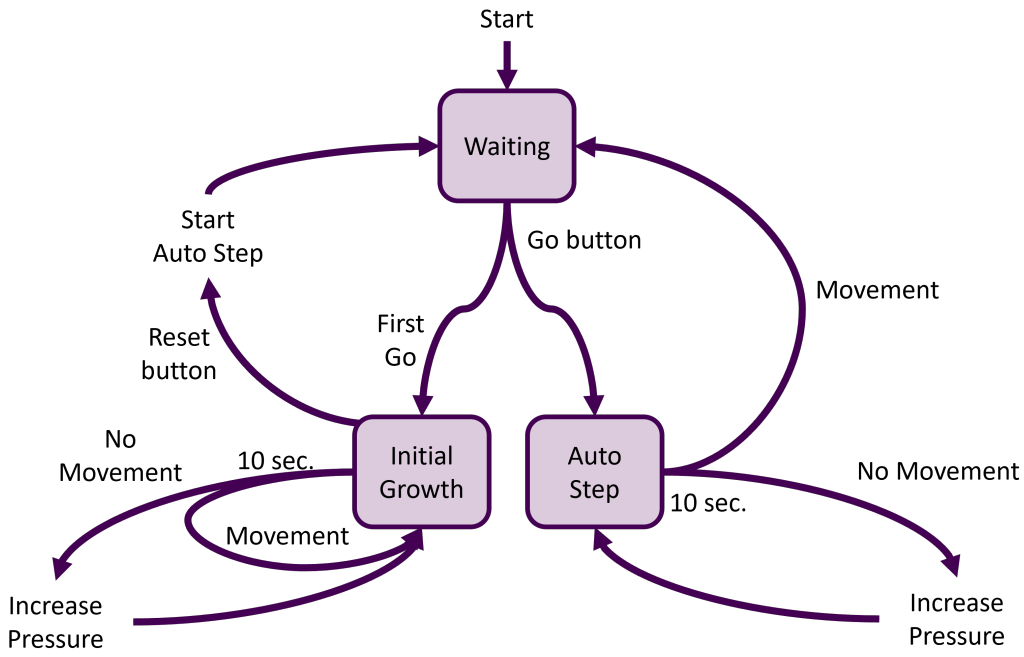

Figure 3.5: State transition diagram for automated growth behavior.

`Auto Step` state, which required manual data observation.

All experiments started in the `Waiting` state and would transition to `Initial Growth` when the go button is pressed. Within the `Initial Growth` state, the software would check the encoder position for movement and would increment the pressure if no growth was seen. If growth was observed, the pressure would be held constant. This growth would continue until the observer hit the reset button (not the Arduino reset button). When restarted with the go button, `Auto Step` would start increasing the pressure until movement was seen. Growth was allowed to continue at this pressure, but the pressure was released after a time interval without growth. At this point, the software would wait for manually input of the observed lengths of overlap of the everting tube over the working channel for each growth phase. The go button would then restart the `Auto Step` state at the final pressure of the previous cycle. This nominal state machine describes the operation during static friction testing, where the other tests make slight changes to this process.

3.3 Experiment Model

A quasi-static free body equivalent of the eversion system under test can be seen in Figure 3.6. The plain eversion equivalent uses the metaphor of a mass, E, hanging from a cable that is pulled forward by a force applied to a pulley, F_{FA}. Since the force is acting on the pulley, half of the force is applied to the cable attached to ground, and half is applied to lifting E. Thus, F_{FA} acts like the growing force at the front area of the everting tube to pull new material to the front and overcome the minimum eversion force required for growth, F_E. Lifting the mass E requires a constant minimum force, F_{ME}, and a length dependent force, F_{LE}, represented by a spring. This metaphor is limited to positive growth, as F_E resists growth, but does not cause retraction. In plain eversion, initiation of growth occurs when the tension in the cable just exceeds the equilibrium with F_E:

$$\frac{1}{2}F_{FA} = F_E, \tag{3.8}$$

$$F_{FA} = \pi r_T^2 p, \tag{3.9}$$

$$F_E = F_{ME} + F_{LE}, \tag{3.10}$$

$$F_{LE} = l_T * k_E, \tag{3.11}$$

where r_T is the radius at the front of the everting tube, p is the pressure within the tube, l_T is the length of the everting tube, and k_E is the length dependent eversion force coefficient.

3.3.1 Static Friction

When the tube is growing over a working channel, the metaphor can be extended by adding a block, P, pulled by the cable along a surface with friction, F_{CF}. In this scenario, the

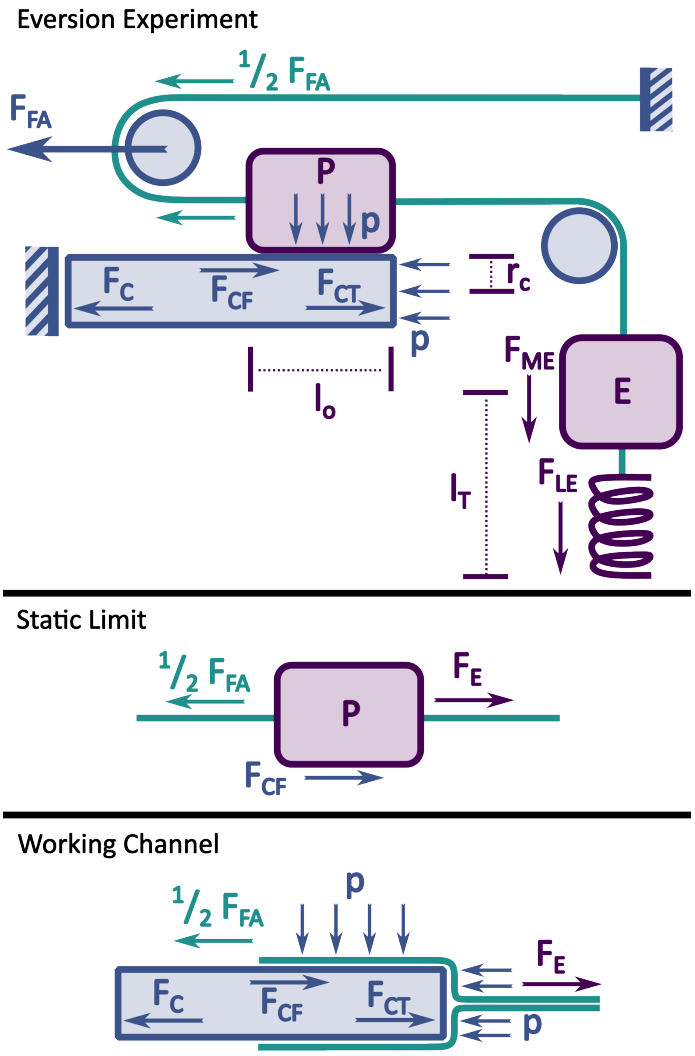

Figure 3.6: Free body diagrams of the abstracted experiment system at zero velocity. ***Top***: The full experimental system, including the force at the front of the tube, the pressure-dependent P-block sliding along the working channel, and the E-block that represents the force required to evert the tube under normal growth. ***Middle***: A diagram of the P-block showing the forces acting on the working channel section of the tubing at the moment when the limit of static friction is reached. F_E is the sum of eversion forces acting on the E-block. ***Bottom***: The forces acting along the working channel by the everting tube.

effective P mass increases with the length of the overlap with the working channel, l_o. In the experimental setup, the pressure also applies force, F_{CT}, to the vertical face at the tip of the channel. The equilibrium point for block P at the limit of static friction is therefore:

$$\frac{1}{2}F_{FA} = F_E + F_{CF}, \tag{3.12}$$

$$F_{CF} = pA_o\mu_s, \tag{3.13}$$

$$A_o = 2\pi r_C l_o, \tag{3.14}$$

where F_{CF} is the static friction force of the tube travelling over the channel, A_o is the area of the material overlap over the channel, r_C is the outer radius of the working channel, and μ_s is the static friction coefficient between the tubing material and the channel. Since the front area of the tube is reduced by the area of the working channel, F_{FA} is reduced to:

$$F_{FA} = \pi(r_T^2 - r_C^2)p. \tag{3.15}$$

In our system, F_{FA} at the point of growth can be estimated using the measured pressure and (3.15), and the eversion force, F_E, can be estimated from plain eversion data. Thus, solving (3.15) for F_{CF} and equating it to (3.13) gives a means of estimating μ_s:

$$F_{CF} = \frac{1}{2}F_{FA} - F_E = pA_o\mu_s, \tag{3.16}$$

$$\mu_s = \frac{\frac{1}{2}F_{FA} - F_E}{pA_o}, \tag{3.17}$$

$$\mu_s = \frac{\frac{1}{2}\pi(r_T^2 - r_C^2)p - F_E}{2\pi r_C l_o}. \tag{3.18}$$

This formulation for estimating μ_s is not dependent on the force applied to the working

channel, F_C, and thus can be performed without a force sensor.

3.3.2 Minimum Eversion Force

However, since the minimum eversion force may be difficult to characterize without fine pressure control and motion sensing, force sensor data from the working channel reaction forces can be used to estimate the eversion forces at the moment of slippage. Figure 3.6 shows the forces acting along the axis of the working channel: the friction force, F_{CF}, and the pressure applied to the tip of the channel, F_{CT}:

$$F_C = F_{CF} + F_{CT}, \tag{3.19}$$

$$F_{CT} = p\pi r_C^2. \tag{3.20}$$

By substituting (3.16) into (3.19), the eversion force can be related to the measured force at the time of slippage:

$$F_C = \frac{1}{2}F_{FA} - F_E + F_{CT}, \tag{3.21}$$

$$F_E = \frac{1}{2}F_{FA} + F_{CT} - F_C, \tag{3.22}$$

Since the growing force and force at the channel tip are based on the pressure and the reaction force of the channel is measured with a force sensor, F_E can be estimated at the moment of slippage. This formulation does not directly depend on the overlap area over the working channel and thus does not require accurate measurement of the tube's position.

3.3.3 Dynamic Friction

During dynamic growth of the tube over a working channel, the force sensor data allows us to ignore the details of dynamic tube growth by using (3.19) and recognizing that the friction

force has shifted into a dynamic regime:

$$F_C = F_{CF,dyn} + F_{CT}, \tag{3.23}$$

$$F_{CF,dyn} = pA_o(\mu_C + \dot{x}_{tail}\mu_v), \tag{3.24}$$

where μ_C is the Coulomb friction coefficient, $\dot{x}_{tail}$ is the tube tail velocity (twice the tube tip velocity), and μ_v is the viscous friction coefficient.

3.4 Experiments

Since the estimation of the static coefficient of friction relies on the estimation of minimum eversion force, the minimum eversion pressure was measured along the length of its path. Given the eversion system's autonomous growth capabilities, characterization of minimum eversion force as a lumped system was used rather than the fine characterization of individual terms methods of [4]. To achieve an understanding of the eversion system's minimum eversion force, the eversion controller was allowed to increase pressure until motion was achieved during a number of positions along the length of the growth pipe.

The static friction trials focused on matching overlap lengths with the pressures required to initiate motion at those positions. These trials were performed with different core diameters and with the addition of lubrication. It was expected that different core diameters would exhibit identical static threshold pressures when compared by the area of overlap. Since the coefficient of friction is primarily dependent on the material in contact, it was expected that the coefficient of friction calculated for each core diameter would be the same. It was hypothesized that the addition of lubricant would lower the coefficient of static friction.

The dynamic friction trials used position, pressure, and force data during a single growth phase along the working channel. This was achieved by setting the growth pressure to the maximum value at the start of the `Auto Step` phase.

All experiments of this work were undertaken with the same eversion system. The static

Table 3.1: Trials and Conditions for Eversion and Friction Characterization

Test	**Core Size**	**Tubes**	**Trials**
Minimum Eversion - Autonomous Search	x	1	3
Static Friction	1/4”	4	10
	1/8”	4	14
Static Friction - Lubricated	1/4”	3	12
Dynamic Friction	1/4”	5	14
Dynamic Friction - Lubricated	1/4”	3	13

friction experiments were performed with minimal experimental variables: core size and lubrication. The dynamic friction experiment only varied the presence of lubrication. Each everting tube was used up to 4 times under a single condition with retraction between trials and replacement after the fourth trial. Trial data were thrown out during friction experiments if the tubes were obviously caught on the tip of the working channel.

3.4.1 Minimum Eversion Force

Minimum eversion pressure for the tubes under test was measured using the `Auto Step` functionality of the eversion control software with fine pressure steps. Starting with a fully inverted tube (all material rolled onto reel), pressure would increase at 0.05 psi (0.34 kPa) every ten seconds until motion of roughly 3/8” (10 mm) was sensed, at which point the pressure would drop back to the starting point of 0.5 psi (3.4 kPa). The cycle would then continue in this way until the tube hit the growth stopper. Each of the three trials had between 33 and 38 data points along this length. The automatic process took roughly 40 minutes per trial.

The pressure that was able to achieve motion was paired with the encoder-based position at the beginning of that cycle. With this data, a model could be fit to determine the minimum eversion pressure for a plain tube without obstacles with the specific eversion system of this experiment. Data from each trial was fit in addition to a model of all data combined. The model of the combined minimum eversion data could then be used in the calculation of the

coefficient of static friction using (3.17).

This model can also be compared to the minimum eversion force calculated from force sensor data collected during static friction trials. Equation (3.22) relates the minimum eversion force to the applied pressure and the force measured along the axis of the working channel. If the searching-based model of minimum eversion pressure is close to the force-sensor-based data, this gives credence to the modeling approaches detailed in this work.

3.4.2 Static Friction

Each tube was fully wound onto the reel and then grown in the `Initial Grow` state using the minimum effective pressure. It was observed that placing the working channel directly in the path of the growing tube often resulted in the tube growing to the side of the channel instead of around. Thus, a wide stopper block was mounted to the force sensor during the growth phase so that the tube would stop growing just past where the tip of the working channel would be, as seen in Figure 3.7. The `Initial Growth` state was stopped with the reset button when it the tube hit the stopping block. At this point, the on/off pressure valve was closed to prevent further tube growth, and the force sensor rail was loosened and slid back to gain access to the working channel adapter.

Care was taken while inserting the tip of the working channel into the center of the everting tube to avoid material scrunching of the everting tube. Then the force sensor was returned to the hard stop and tightened into place. After recording the initial overlap position, the on/off valve was opened and the `Auto Step` phase was begun. At the end of each growth, the overlap length was noted and the `Auto Step` cycle was restarted from the new overlap position. The initial pressure for `Auto Step` was 1 psi (6.9 kPA) and each increment about 0.5 psi (3.4 kPa). When the pressure limit was reached, the final position was noted and the experiment stopped. All overlap positions were then recorded into the trial metadata. Data from a characteristic trial are shown in Figure 3.8.

To investigate the ability of lubricant to decrease the coefficient of static friction, and thus increase the maximum overlap length, a water soluble lubricant was applied to the 1/4”

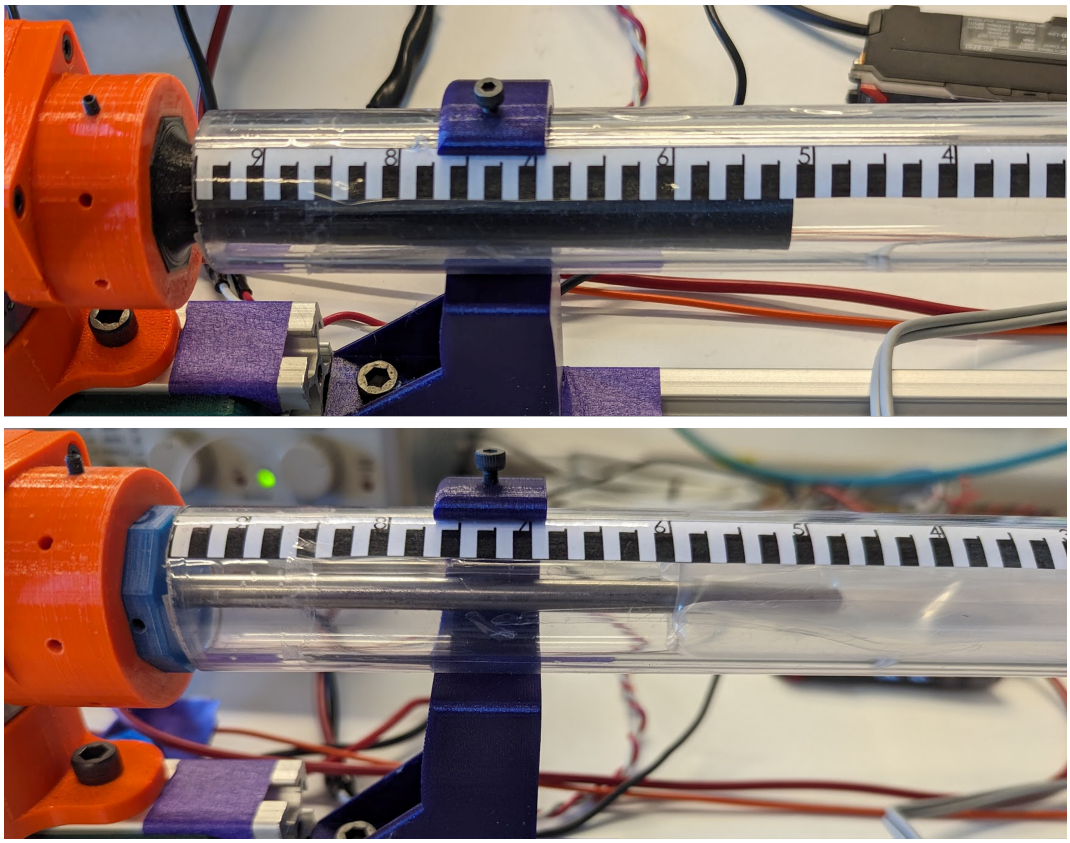

Figure 3.7: Close-up of growth stopper and everting tube growing over working channel. ***Above***: Growth stopper mounted to force sensor. This stops the growth of the everting tube at a repeatable location for every trial. ***Below***: The working channel after it has been inserted into the central lumen of the everting tube.

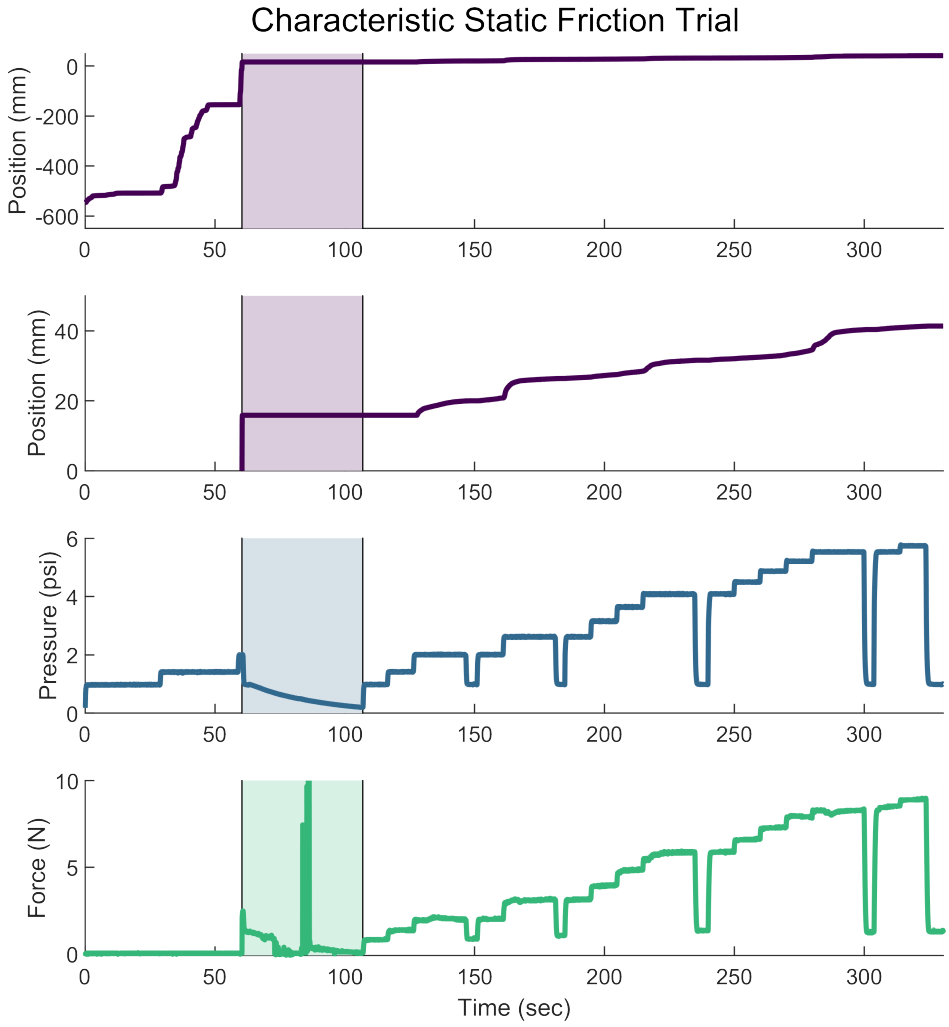

Figure 3.8: Characteristic static friction trial. This trial is a 1/4" working channel without lubrication. The shaded area is the swapping phase between initial growth and growth over the working channel. The position data are relative to the tip of the working channel, thus representing overlap length. The second position graph from the top is a magnification of the overlap growth phase of the experiment. This trial required 2 pressure increments to evert to the stopping block. During the 3rd phase, the pressure just before each drop to nominal pressure (1 psi) is the pressure that was able to initiate growth. This pressure was held until movement stopped.

working channel after removing the stopping block from the force sensor assembly. EZ-Jelly by Athena Medical Products was chosen for these tests due to its primary use as a lubricant for insertion of medical devices into the body. The amount of lubricant added to the working channel was not measured.

The minimum eversion force, F_E, needed to solve for the coefficient of static friction in (3.17) can be estimated from the model determined in the first test or from the force sensor data as in (3.22). The minimum eversion force model, (3.10), merely requires using the position of the tip before growth in the model. To use the force sensor data, it was necessary to find the moment of peak applied force near the time that the tube started to move. For each growth phase, the maximum force within 1.2 seconds of the final pressure increase was found. The force and pressure at this time were used in (3.22) to calculate F_E for that growth phase. The coefficients calculated with these two methods were compared using ANOVA to determine if the method of determining F_E affected the outcome. All ANOVA tests in this work consider a p-value less than 0.05 to be statistically significant.

The pressure required to initiate growth for each growth phase among all trials was compared between each working channel radius and lubrication status. Comparison of the threshold pressure as a function of the overlap area of the working channel instead of length should normalize the effect of radius and allow for comparison across working channels. According to (3.17), if the coefficient of friction is constant, the change in the static threshold pressure should be a function of area, A_o, and any length dependence in F_E.

Finally, all calculated coefficients of static friction were compared with ANOVA to determine the effects of working channel radius and lubrication. One-way tests were used to compare coefficients from radius change without lubrication and lubrication change with the 1/4" working channel data.

3.4.3 Dynamic Friction

In order to investigate time series data of fully dynamic growth, the `Auto Step` state was altered for this experiment to immediately set the growing pressure to the maximum of 5.8

psi. The experiment was otherwise identical to the static friction experiment. The conditions tested were the 1/4" working channel and with and without lubrication. Data from a characteristic trial can be seen in Figure 3.9.

Unlike the static friction trial, time series data from the duration of dynamic growth of each trial was used to calculate the coefficient of dynamic friction. A constant offset was used to match the tube tip position at the end of growth to the observed position along the visual scale. End of growth was determined to be the point at which tube velocity dropped below 1 mm/sec. The dynamic coefficient of friction during growth was then calculated using (3.23) for each time step.

The collected coefficients were compared with a 1-way ANOVA test to determine if lubricant significantly effected the coefficient. An additional effect of lubrication could be ability to achieve a greater overlap length at the same growth pressure. Another 1-way ANOVA test was used to determine the significance of lubrication on the final overlap position of the growing tubes.

The calculated coefficients were also plotted against the tube velocity at the time of each calculation. Any trend in the coefficients with increasing velocity could be used to model the viscous friction in (3.24). An interaction model ANOVA test was used to determine the significant effects of lubrication and velocity on the coefficient of dynamic friction.

3.4.4 General Evaluation

Evaluation Hypothesis I: The coefficient of dynamic friction is lower than the coefficient of static friction.

According to the classic friction model, it is expected that the coefficient of dynamic friction is less than the coefficient of static friction. If this is the case, it is an indication that our modeling and methods have merit. If the dynamic friction coefficient is higher, then the measurements or the model are improperly used for this application.

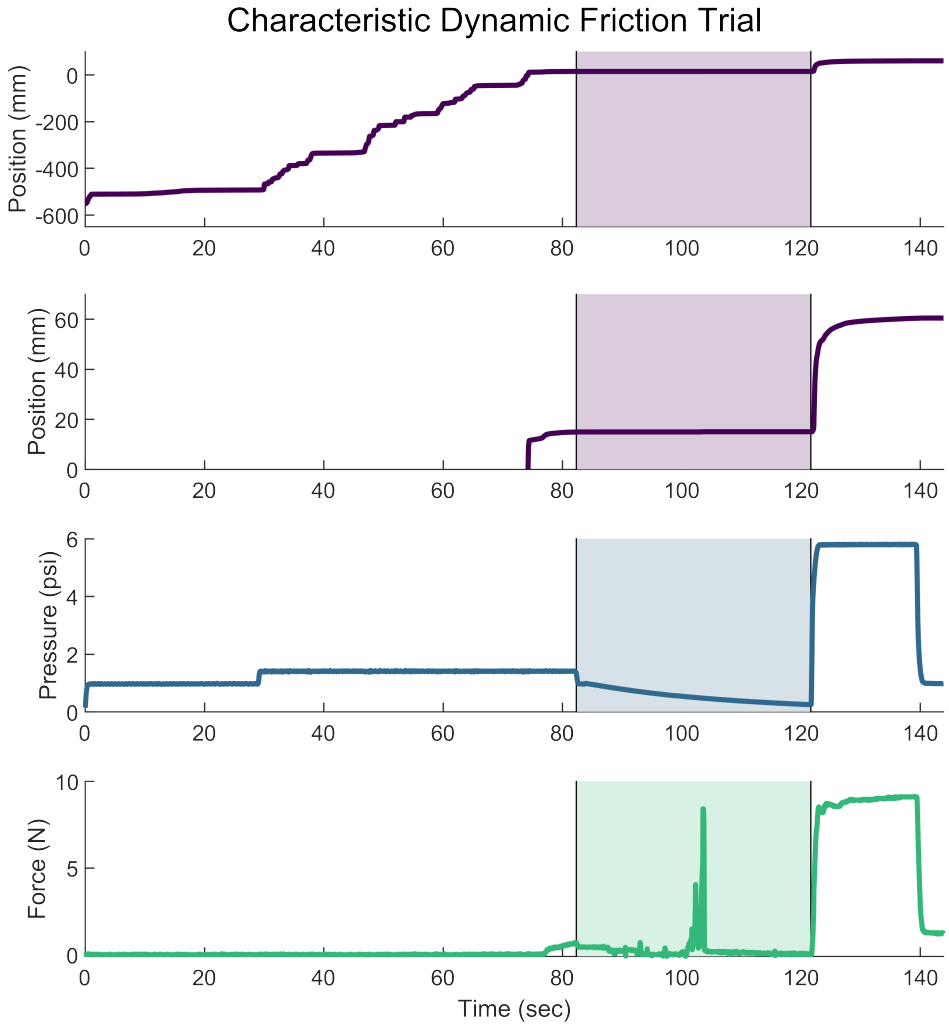

Figure 3.9: Characteristic dynamic friction trial. This trial is a 1/4" working channel without lubrication. The shaded area is the swapping phase between initial growth and growth over the working channel. The position data are relative to the tip of the working channel, thus representing overlap length. The second position graph from the top is a magnification of the overlap growth phase of the experiment.

Evaluation II: The maximum overlap as calculated from the engineering values matches the maximum overlap lengths seen in the static and dynamic friction trials.

The results from these experiments can be used to predict performance of similar experimental setups with the same materials. One useful model from these data is the theoretical maximum that an everted tube can evert over a working channel. After solving (3.18) for the overlap length, l_o:

$$l_{max} = \frac{1}{\mu}\frac{\frac{1}{2}P_{burst}(R^2 - r^2)\pi - F_E}{P2r\pi}, \tag{3.25}$$

the value of the working channel radius, r, can be treated as the independent variable in a model of maximum overlap length. The value of P can be set to the tube's burst pressure (or a safety factor thereof) to find the maximum overlap length for any channel radius.

This maximum-length model was used to evaluate the modelling of this work by setting μ to the average calculated values of static and dynamic coefficients, both with and without lubrication, and comparing the expected maximum length to those seen in the experiments. The value of minimum eversion pressure was set to a constant value calculated at the top of the working channel's position in the experimental F_E fit, 2N.

3.5 Experimental Results

3.5.1 Minimum Eversion Force

What force is required to begin growth of the tube at any given length?

The minimum force required to evert along the length of the experimental setup can be seen in Figure 3.10. The first trial required an initial force of roughly 2 N to evert near the starting position, and the subsequent trials required closer to 1 N to start growing. All trials showed an increasing trend in required force with increasing length. The fits for each trial and for all trials combined, in addition to the residual distribution for each fit, can also be seen in Figure 3.10. The minimum eversion force fit for all data is $1.26xN/m + 1.48N$. Most data fall within ± 0.5 N of this fit.

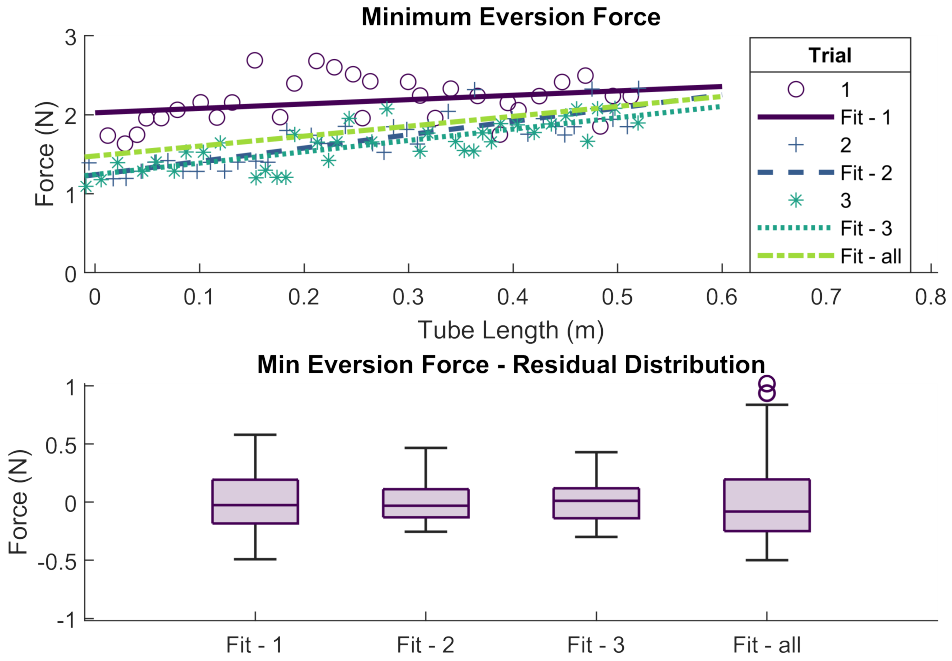

Figure 3.10: Force required to initiate eversion growth across three trials of one tube with automated pressure increments. ***Top***: Eversion force data and linear fits for each trial and a fit for all data. ***Bottom***: Residual distribution for each trial's fit and the residuals of all data from the overall fit.

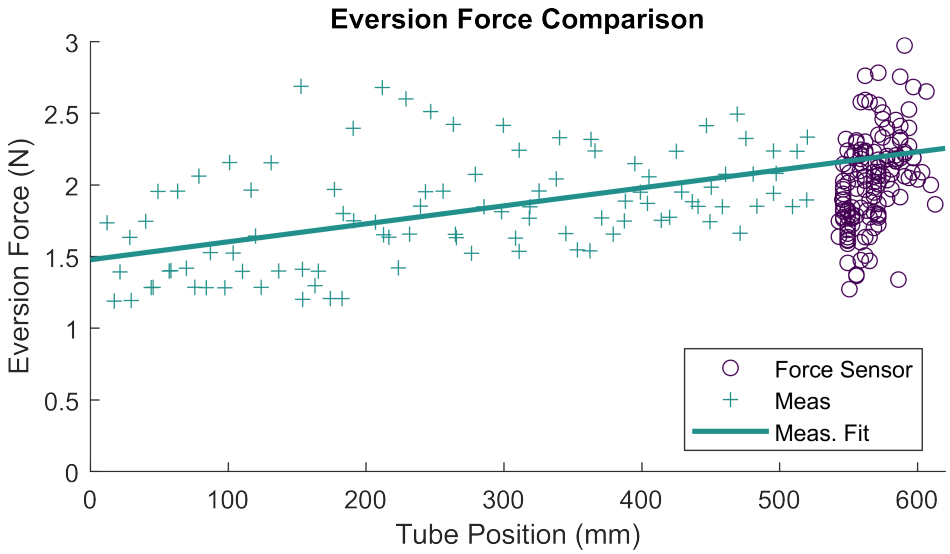

Figure 3.11: Comparison of all measured minimum eversion forces and the minimum eversion forces calculated from static friction threshold data.

Is the searching method eversion force, F_E, similar to the eversion force calculated from the force sensor during static friction trials?

The comparison of F_E as measured during the minimum force experiment and during the static friction trials can be seen in Figure 3.11. The fit for the measured minimum force intersects the force-sensor-based calculations and the range of values for both sets of data are similar.

3.5.2 Static Friction

Does the data source of eversion force, F_E, make an impact on the calculation of to coefficient of static friction?

Calculation of the coefficient of static friction between the LDPE tube and steel working channel by different F_E estimation methods has a statistical difference on the resulting coefficients for non-lubricated working channels. This comparison has a p-value of 0.001. Figure 3.12 shows the decrease in the calculated static coefficient when using the searching-

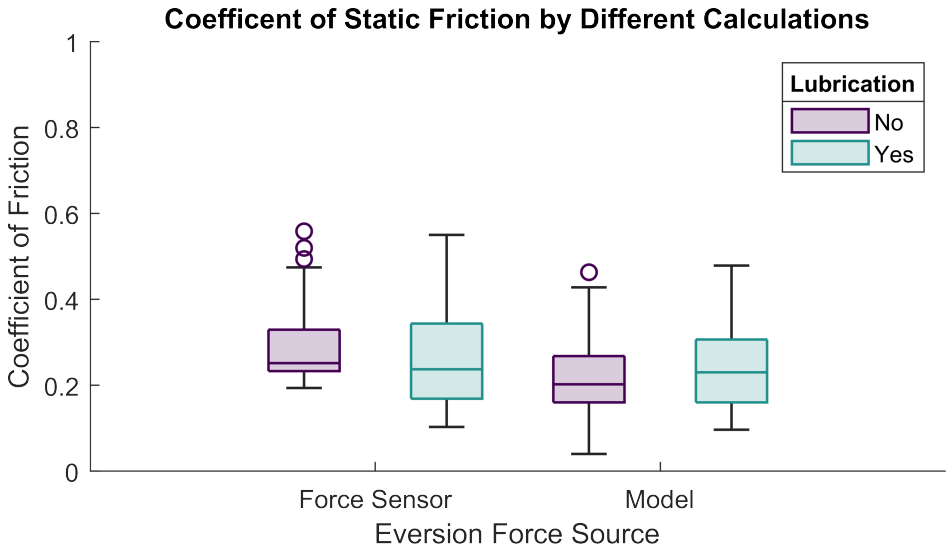

Figure 3.12: Comparison of calculated coefficients of static friction by method of estimating minimum eversion force. This data only includes tests with 1/4" working channel.

based model fit rather than the force sensor data collected with each static friction data point. The average coefficient for non-lubricated trials based on the force sensor data is 0.29, while the model results in a value of 0.20, a decrease of 31%. The values for lubricated trials do not change significantly, with a p-value of 0.2.

What is the static threshold pressure for an everting tube growing over a working channel?

The static threshold pressure compared to overlap area for all trials can be seen in Figure 3.13. The non-lubricated trials have very similar threshold pressures when normalized by overlap area, as evidenced by nearly overlapping fit lines. The lubricated trials exhibited a shallower fit, but a higher y-intercept. The lubricated trials also achieved larger overlap areas than the non-lubricated trials.

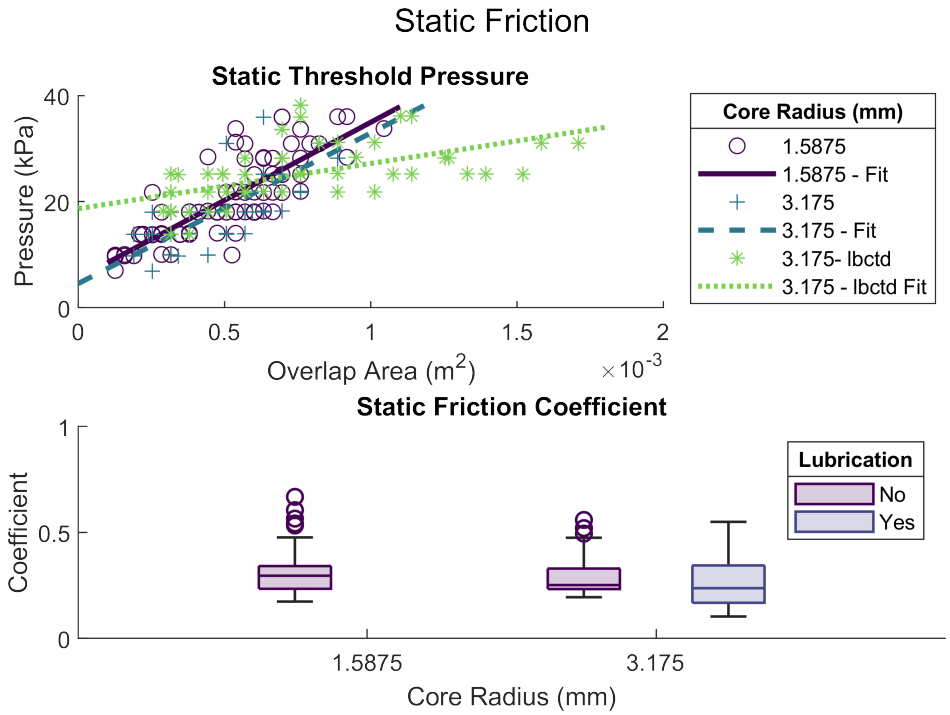

Figure 3.13: Static friction results. ***Top***: Threshold pressure per tube overlap over a working channel for working channels of different radii and with the presence of lubrication. ***Bottom***: The distribution of calculated coefficients of static friction.

What is the coefficient of static friction for the everting tube growing over a working channel?

Figure 3.13 also show the distribution of coefficient of static friction for all trials. These values are calculated with force sensor data instead of the modeled fit from the previous experiment because the force sensor data is more closely associated with the conditions of each specific trial. There is no significant difference between the coefficients measured with different working channel radii or when using lubrication. Table 3.2 details the average coefficients and the ANOVA results.

Table 3.2: Average (Std. Dev.) Coefficient of Friction Results

	Working Channel Diameter			**lubrication difference**	**radius change p-value**	**dry vs lubrication p-value**
	1/8 inch (3.2 mm)	**1/4 inch (6.4 mm)**	**1/4 inch lubricated**			
Static	0.3111 (±0.096)	0.293 (±0.094)	0.271 (±0.129)	7.50%	0.35	0.38
Dynamic		0.211 (±0.039)	0.116 (±0.045)	45%		**<0.001**

3.5.3 Dynamic Friction

What is the coefficient of dynamic friction for the everting tube growing over a working channel?

Coefficients of dynamic friction calculated during each of the dynamic growth trials can be seen in in Figure 3.14. The non-lubricated trials tend to cluster at higher coefficients and achieve shorter overlap lengths than the lubricated trials. During dynamics friction trials, lubrication exhibits a statistically significant impact on the coefficient of friction, reducing the average coefficient from 0.21 by 45% to 0.12 with a p-value less than 0.001.

Is there a viscous component of dynamic friction while the everting tube grows over a working channel?

The instantaneous coefficient of dynamic friction does not exhibit significant dependence on tube velocity. This can be seen in Figure 3.14, where the linear fits for the lubricated and plain trials are nearly horizontal. The interaction ANOVA results in a p-value of 0.14 for velocity as a continuous factor, and 0.405 with the interaction of lubrication and velocity as a factor.

Does lubrication affect the final overlap position of a dynamic growth trial?

The final overlap length as a factor of lubrication resulted in a significant p-value of 0.023, increasing average overlap from 4.8 cm by 28% to 6.4 cm. The distributions for this data can be seen in Figure 3.15.

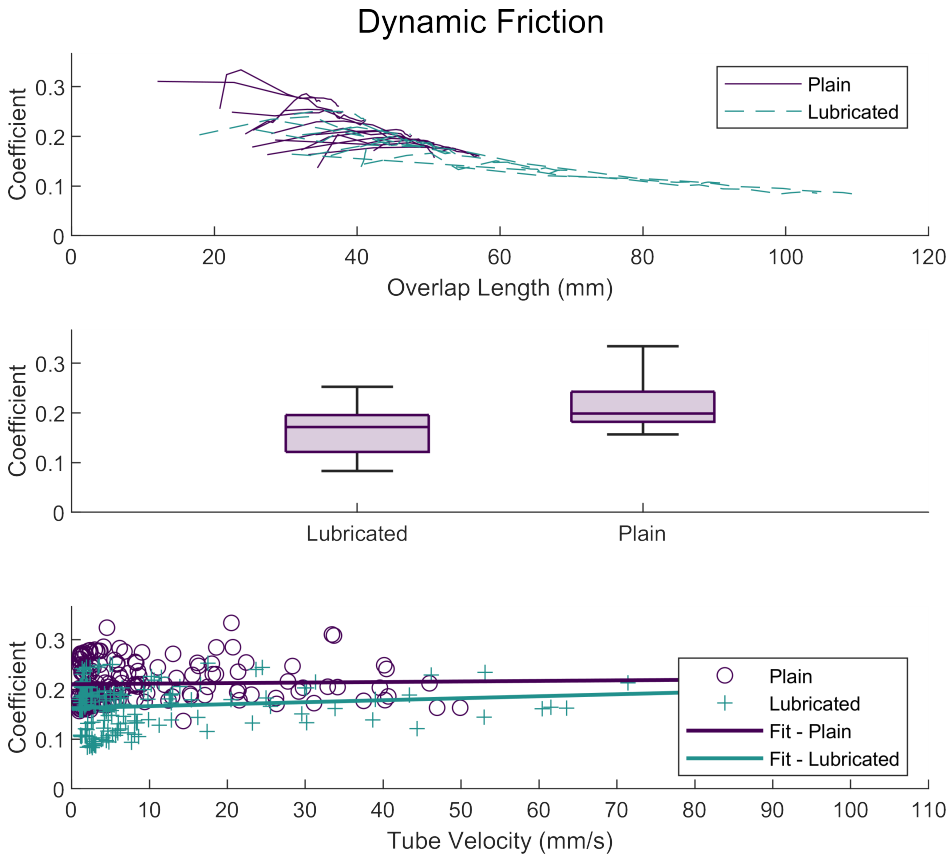

Figure 3.14: Coulomb friction results. ***Top***: Calculated coefficient of Coulomb friction over the length of each trial with dry and lubricated working channel. ***Middle***: Distribution of Coulomb coefficients. ***Bottom***: Instantaneous Coulomb coefficients with their corresponding instantaneous velocity.

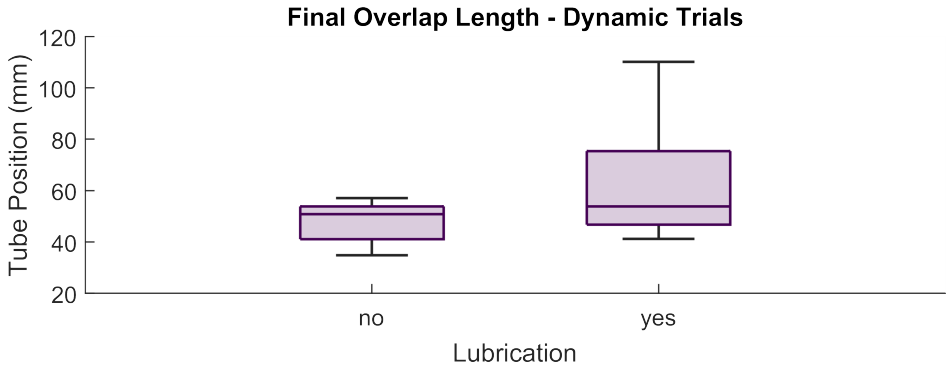

Figure 3.15: Maximum length achieved during dynamic friction trials with and without lubrication.

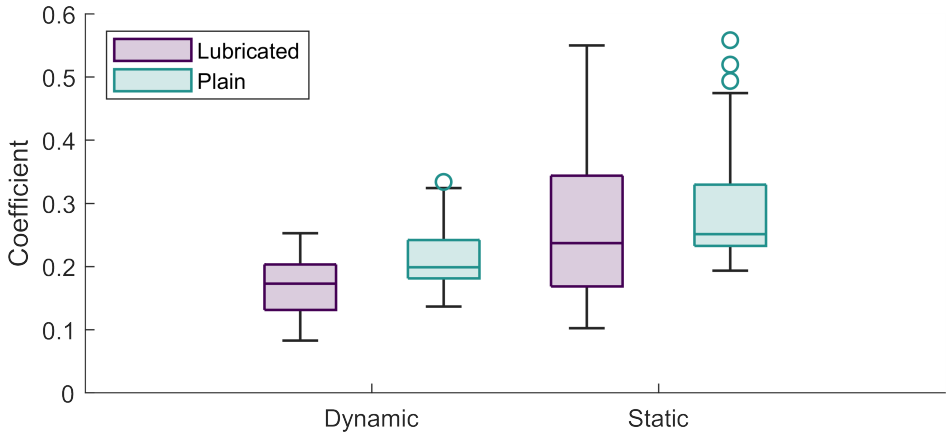

Figure 3.16: Comparison of static and dynamic coefficients of friction with and without lubricant.

3.5.4 Evaluation

Evaluation Hypothesis I: The coefficient of dynamic friction is lower than the coefficient of static friction.

A comparison of the coefficient of friction results can be seen in Figure 3.16. A comparison of the non-lubricated trials with the 1/4" working channel resulted in a p-value of less than 0.001, indicating that the values of static and dynamic friction are distinct.

Evaluation Hypothesis II: The maximum overlap as calculated from the engineering values matches the maximum overlap lengths seen in the static and dynamic friction trials.

The theoretical relationship between the maximum overlap of the tested tube and a working channel of 1 to 7 mm in radius is shown in Figure 3.17. This model shows the maximum length relationship for the coefficients measured during the experiments of this chapter. It can be seen that the 1/r dominates the model and the tested tube would be unable to meaningfully grow over a working channel with a radius much larger than 7 mm, or roughly 50% of the tube radius. The average final overlap positions for the trials are also plotted, and are fairly close to the predicted values at the intersections of the tested working channel

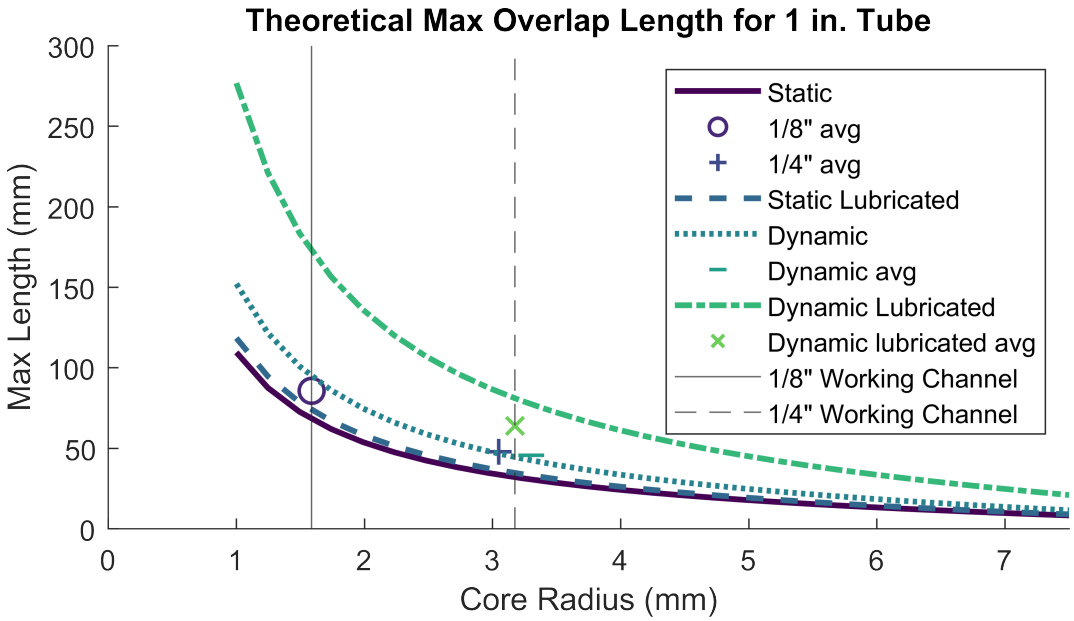

Figure 3.17: Theoretical maximum length for a working channel within a 1 inch (25.4 mm) diameter everting tube in the tested experimental setup. This model assumes a minimum eversion force of 2N, which was shown to be roughly the force required to evert at the distal working channel in this setup.

radii.

3.6 Discussion

3.6.1 Minimum Eversion Force

The autonomous searching method for determining the minimum eversion force as a function of length was a very effective method. As seen in Chapter 2, the performance of the first eversion trial differed from the subsequent trials, likely to due to material wear. A limitation of the experiments in this Chapter is that only one tube was tested, and there were no accommodations made to model the variability between or within tubes. This may likely be the reason that coefficient of friction results were different when calculated with the minimum eversion force fit from only 3 tubes when compared to coefficients calculated from force sensor data (Figure 3.12).

As discussed in Chapter 2, two contributions to the minimum eversion force are the reel inertia and friction on the reel. The act of everting new material at the tip of the growing tube should require some force in addition to the reel loads. At low accelerations the reel inertia is unlikely to contribute much the the eversion force. The medium friction torque, as measured in Chapter 2, was 0.017 Nm and corresponds to a force of 1.65 N at a radius of 0.01 m. This force is slightly above the minimum eversion fit of all trials at zero length. This could be due to a decrease in friction characteristics with nearly a year between experiments, or it could indicate that everting of material is a fairly efficient process compared to reel friction. Further reel-less eversion force testing with the ToF sensor of Chapter 2, or manually observed position recording, would shed more light on this relationship.

The comparison of the searching-based minimum eversion force and the force-sensor-based calculation in Figure 3.11 show that the modeling and experimental procedures in this work have merit. The measured fit of minimum eversion force predicts a higher eversion force than the average force-sensor calculations, but this could perhaps be improved with a more robust modeling of minimum eversion force with some of the methods described above. Although the model-based calculations of static friction coefficients were lower than those derived from force sensor data, they were still close and did not rely on a relatively expensive sensor.

Extrapolating the fit of minimum eversion pressure to the force at the tube's burst pressure gives an estimate of the maximum length for an everting tube in this setup. With a burst pressure of 6 psi (41.3 kPa) converted to the force applied to the tail ($\frac{1}{2}F_{FA}$), leads to a force of 10.1 N. Solving the average fit of minimum eversion force for length gives a maximum eversion length of 6.9 m.

3.6.2 Static Friction

Since the calculated values of the coefficient of static friction statistically differ depending on the source of the eversion force value, it may be difficult to rely on an averaged model of a tube's eversion force to accurately determine the static friction limit. Figures 3.10 and

3.11 show a clear trend in the eversion force data, but they also show a range of ±50% of the linear fit along the length of the experiment. Thus, pairing the instantaneous threshold pressure with the force recorded at that point in time instead of an averaged model is likely to calculate more accurate coefficients.

The statistically similar coefficients calculated between the working channels of different radii help to validate the modeling and methods of this work. Since the materials in contact did not change, the coefficient of friction should not have changed. The comparison between static threshold pressures as a function of overlap area were nearly identical across radii. The agreement of results across experimental variables indicates robust modelling and experimental measurement.

It is unclear why lubrication had no statistical effect on the static coefficient of friction as tested. Figure 3.13 does appear to show some effect of lubrication: the lubricated trials are able to achieve larger overlap areas at the same threshold pressures, and the distribution of lubricated friction has a lower bottom range. It could be that a more controlled method of lubricant application or a different formulation could lower the friction in certain scenarios.

3.6.3 Dynamic Friction

In Figure 3.14, the trajectories appear to hit a barrier in the shape of a parabolic function. This is likely the shape of the maximum possible overlap as a function of the coefficient of dynamic friction. As the coefficient approaches zero, the potential for overlap grows significantly. This Figure highlights the utility of adding lubrication to the working channel to reduce the coefficient of friction. This figure also demonstrates that lubrication allows the tube to achieve higher velocities at the same pressure. Although there was no indication of viscous friction in this data, higher ranges of velocity may exhibit viscous tendencies.

3.6.4 Maximum Working Channel Length

The close match of the average maximum overlap lengths with the predicted models predicted is a promising sign for this research. However, Figure 3.17 also illustrates the difficult trade-

off when designing an everting tube robot with concentric working channel: the radius of the working channel should be as small as possible in order to achieve sufficient overlap lengths.

3.7 Future Work

A key limitation emphasized by the results of this work is the limitation on the maximum length that an everting tube can grow over a working channel. Future work may focus on investigation of the effects and proper application of lubrication or combinations of materials that exhibit naturally low friction. Additionally, as seen in [13], the use of flowing gas between the everting tube and the working channel may greatly reduce contact and therefore reduce the effective friction caused by the working channel. This is an especially promising area of research for everting cystoscopy introducers, as the standard cystoscopy procedure relies on the constant flow of saline into the bladder through the cystoscope. If the saline is pumped through the space between the cystoscope and the everting tube, the maximum overlap length may be greatly improved.

Further work could also investigate the mechanics behind the length-dependence of minimum eversion pressure. In [4], it is put forward that length dependence is due to increasing contact area and normal force of the new material rubbing against the outside material. It could also be that the lengthening tail of the everting tube could require more force to achieve the same effective force at the reel. As the tube lengthens, the compliance of the lengthening tail should act like a longer spring, while the force required to pull new material from the reel should stay relatively constant. Thus, a longer displacement of the spring at longer lengths is required to achieve the same unreeling force. This higher displacement would be achieved with a higher pressure within the tube, resulting in a length-dependent minimum eversion pressure profile.

3.8 Conclusion

This chapter has detailed the modeling and experimental methods for determining the static and dynamic friction characteristics of an everting tube growing over a working channel.

Understanding these interactions and being able to estimate the coefficients of friction is an important step in being able to engineer everting tube robots that can transport sensors and actuators through their central lumen. The specific contributions of this chapter are:

1. A novel measurement of the length dependence of minimum eversion pressure;

2. An estimation of static friction of an everting tube over a working channel without a force sensor with an error of 31%;

3. A measurement of minimum eversion force with a force sensor;

4. Estimation of dynamic friction of an everting tube over a working channel with a force sensor; and

5. Measurement of the effects of lubricant on the static and dynamic friction between an everting tube and a working channel.

Chapter 4

DESIGN EVOLUTION OF AN EMERGENCY AIRWAY DEVICE

Research Aim 3: Design an emergency airway device that can reliably deploy into the airway and provide a channel for rescue breaths.

4.1 Introduction

Airway Management is critical to patient survival in cases of cardiac arrest, drug overdose, and trauma. In the US, Emergency Medical Services (EMS) responded to nearly 150,000 reported cases of Out of Hospital Cardiac Arrest (OHCA) in 2021 [74]. In more than 40% of these cases a bystander initiated CardioPulmonary Resuscitation (CPR), but over 90% of all cases resulted in death. According to paramedics interviewed in King County (Washington, USA), a patient will likely die due to cardiac arrest when an advanced emergency airway is not established, even in cases of resuscitation [75]. Airway injuries are also the 2nd highest cause of fatalities in US combat, demonstrating an additional demand for airway management devices in out-of-hospital trauma scenarios [76].

Commercial devices for advanced airway management include EndoTracheal Intubation (ETI) tubes and supraglottic airway devices such as Laryngeal Mask Airways (LMA's), CombiTubes, and I-Gels. ETI is considered the most effective method for establishing a patent airway as it seals inside the trachea, although it requires the most experience to operate [76]. For example, performing advanced life support as a paramedic in Seattle, Washington requires 2150 hours of training over the course of 2 years [77]. Improper use of such devices can lead to severe injuries including throat lacerations, spinal cord injuries, and in severe cases even death [78, 79]. There are currently no emergency airway management options that

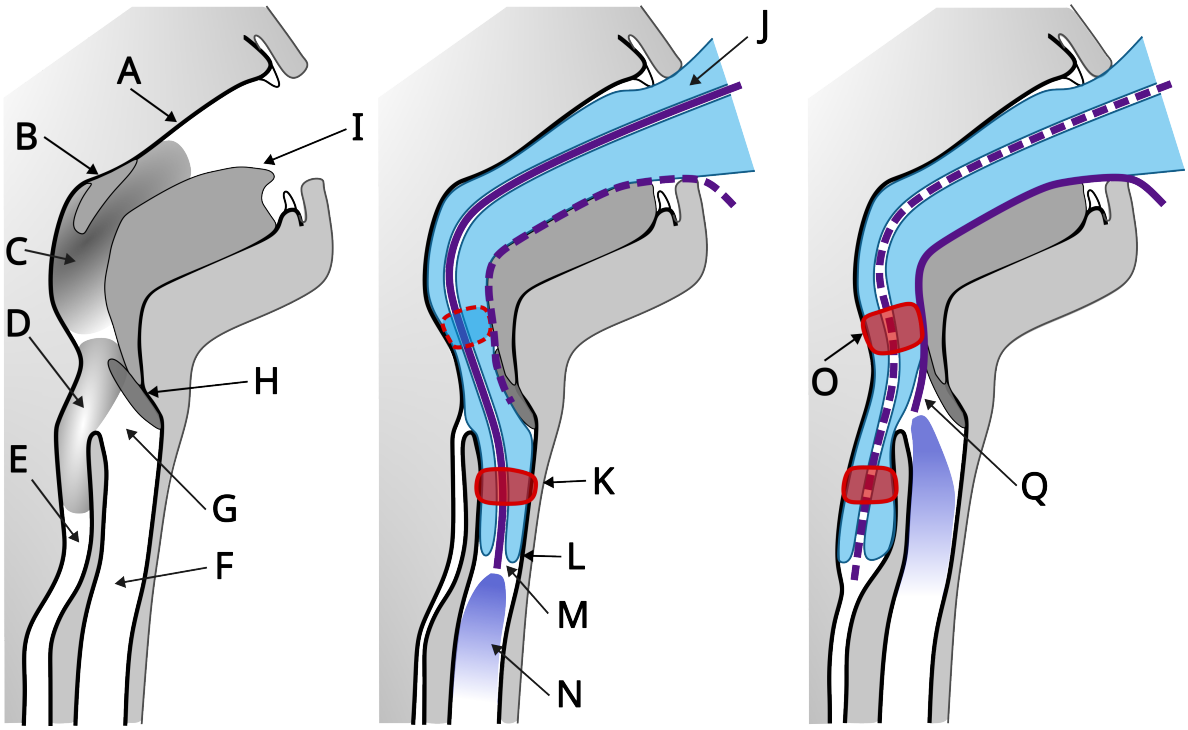

Figure 4.1: Everting Airway Device deployment concept. *Left*: Select anatomy of the airway: (**A**)- soft palate, (**B**)- uvula, (**C**)- oropharynx, (**D**)- hypopharynx, (**E**)- esophagus, (**F**)- trachea, (**G**)- larynx, (**H**)- epiglottis, and (**I**)- tongue. *Center*: Tracheal deployment of the Airway Device. Air pressure within the device (**J**) has grown the tube through the throat and deployed the *distal sealing cuff* (**K**). Once the device tip is deployed into the trachea at (**L**), the distal cuff inflates to allow for breathing air from the *central air line* (**M**) to inflate the lungs (**N**). *Right*: In the case of esophageal deployment, the distal cuff and the *proximal sealing cuff* (**O**) are inflated before providing breathing air through the *side air line* (**Q**).

can be operated by inexperienced personnel.

An Emergency Airway Device (EAD) that can be operated by users with little to no training has been proposed in Hwee et al.[57] and O'Connor et al.[58]. This chapter summarizes and expands on that work in order to outline the design goals and improvements made throughout the development process. The EAD concept takes advantage of the mechanical intelligence and minimal interaction forces of soft everting tube robots, sometimes called vine robots [4], in order to achieve a safe device that can be easy to use.

4.1.1 Airway Devices

Medical personnel use emergency airway devices to establish a stable breathing tube between the lungs and the outside of the body; the related anatomy is detailed in Figure 4.1. As mentioned, the gold standard for establishing an airway is with an ETI. Before inserting an ETI into the body, the patient's neck is extended to align the mouth with the trachea [80]. A hooked device with illuminated tip, called a laryngoscope blade, is then used to hold the tongue against the lower jaw, keep the epiglottis depressed, and expose the true vocal cords between which the ETI is intended to be inserted. The ETI is then manually inserted past the blade and into the trachea. Once in place, a sealing cuff is inflated with air from a syringe in order to prevent breathing air from escaping back through the mouth or into the esophagus and stomach. The ETI can then be attached to a manually activated resuscitation bag or mechanical ventilator to provide breaths.

LMA and CombiTube devices provide a less reliable airway, but are sometimes preferred in emergency situations. An LMA is inserted into the throat so that the mask feature is placed in the hypopharynx and can be inflated to create a seal around the opening of the trachea. The CombiTube is similarly inserted into the throat and can be sealed with inflating cuffs above and below the larynx or within the trachea, allowing for a successful airway in the case of non-tracheal deployment. Both the CombiTube and LMA require significant insertion forces and can be dangerous for the patient and difficult to use effectively [81]. We believe that there is a need for a reliable and safe emergency airway device that can be used by minimally trained bystanders.

4.1.2 Robot Assisted Intubation

Several robot-assisted ETI systems have been developed. The Kepler Intubation System (KIS) uses a commercial laryngoscope mounted on a robot arm to perform teleoperated intubation [82]. An initial study of the KIS resulted in a 91% success rate in a clinical test. Remote Robot-Assisted Intubation System (RRAIS) is an over-the-mouth device for intubation

that utilizes an endoscope to provide video feedback to its expert teleoperator [83]. RRAIS was slower to intubate porcine test subjects but held a higher success rate than manual laryngoscopy. The Robotic Endoscope-Automated via Laryngeal Imaging for Tracheal Intubation (REALITI) system partially automates the ETI procedure [84]. This system utilizes computer vision to identify the glottic entrance and automatically orients an endotracheal tube towards its geometric center using an actuator around the tube. Results showed that the REALITI system could assist non-medical professionals in performing laryngoscopy. While these systems made large strides to automate the intubation process, they largely depend on bulky, expensive, and specialized equipment or a highly trained teleoperator, limiting their widespread use for out-of-hospital emergencies.

4.1.3 Vine Robots and Eversion

Vine robots are a form of soft robots that grow via tip eversion, where inverted material is pulled from inside the tube and flipped inside out due to internal fluid pressure [4] (Figure 4.3). Growth via shape-conforming tip extension allows the soft robot body to move along the path of least resistance, passively navigating over, around, and through obstacles. These soft robots can also travel through constrictions that are smaller than their nominal body diameter. The stationary soft body tube also limits the shear contact forces between the tube and its environment. Everted tubes have been proposed for sensitive medical applications such as endovascular surgery [85], mammary gland cancer diagnosis [30, 63], and catheterization of brain ventricles [9].

Many vine robots are constructed from inexpensive Low Density PolyEthylene (LDPE) plastic tubing available on long reels, also called poly tubing, or from nylon fabric coated in either Thermoplastic Polyurethane (TPU) or silicone [66]. Welding of elements within or to the body of the tube is common for achieving pre-determined shapes or actuation elements. Polytubing can be welded with heating elements [86], often with linear, clamping sealing elements [30], while coated nylon fabric is often welded with silicone adhesive [87, 88].

Figure 4.2: *Left*: Commercial Airway Management Trainer from Laerdal Medical (Norway). *Right*: Advanced Joint Airway Management System (AJAMS) components from the University of Washington.

4.1.4 Airway Training Phantoms

In order to evaluate the performance of the EAD in a lab setting, a benchtop model of the airway with realistic anatomy and mechanical response can help optimize the design prior to cadaver or animal model testing. While there is an array of commercial systems for intubation training, such as those in Figure 4.2, many are not based on patient DICOM imaging datasets, resulting in general or non-human appearing trainers. Many phantoms are made of stiff materials that are not indicative of human tissue [89]. Furthermore, detailed analysis of EAD deployment is aided by transparency along the airway and the ability to integrate sensing into the setup. For the developments in this paper, custom phantoms are designed specifically for the goals of each design phase. The ultimate goal before in vivo testing is a state of the art, soft tissue airway trainer followed by cadaver testing.

4.1.5 An Everting Airway Device

In this chapter, we will describe the operating concept of the everting Emergency Airway Device as well as the designs and performance of each of the three device prototypes to

date: EAD-1 [57], EAD-2 [58], and the most recent prototype, EAD-3. The next section provides an overview of the ideal design of a commercial EAD as well as the performance characteristics to be optimized. Sections 4.3 and 4.4 summarize the previous designs and detail key results that were used as benchmarks during subsequent development. An updated EAD-3 prototype, a novel manufacturing method for everting tube robots, and EAD-3's performance are presented in Section 4.5. Finally, future development directions of the EAD are discussed in section 4.6.

4.2 Device Concept

The everting Emergency Airway Device is an everting vine robot that deploys into the airway to allow for reliable delivery of assistive breaths. The ultimate design for the EAD would allow for portable use outside of hospital to provide a patient with an emergency airway until arrival at a hospital. Growth via tip extension would eliminate shear force exerted on the throat due to insertion, which is a marked improvement over market airway devices. The passive navigation behavior of a vine robot would also allow the device to be used by individuals who are not trained medical professionals, similar to the accessibility of Automatic Emergency Defibrillators (AED). In order to be an effective lifesaving device, the EAD must: (1) reliably deploy into the airway at pressures comparable to other airway devices on the market; (2) provide adequate airway sealing; (3) support the delivery of airway breaths; and (4) be portable for out-of-hospital use.

To ensure a high airway success rate on first use, a key feature for our device is the ability to establish an airway when deployed into both the esophagus and the trachea. In order to achieve this, the EAD concept features two sealing cuffs and two parallel breath delivery tubes, much like a CombiTube. If the tube deploys into the esophagus, a side air delivery tube could deliver air to the trachea with the proximal cuff providing airway sealing to prevent air from escaping through the mouth or nose and the distal cuff sealing off the esophagus preventing the entry of air into the stomach and aspiration. If deployed into the trachea, a central air delivery tube would supply breaths with a distal cuff sealing the tracheal

Table 4.1: Evaluation Tests for EAD Prototypes

Metric	EAD-1	EAD-2	EAD-3
Everting Pressure	✓	✓	✓
Everting Forces			✓
Airway Sealing	✓	✓	
Burst Pressure		✓	✓
Deployment Success Rate	✓		✓

opening. The intended deployment location of the device is demonstrated in Figure 4.1. The air delivery channels can be integrated into the body of the tube, deploying with device eversion (Figure 4.3). Like an ETI, once the EAD is deployed the breathing channels can be connected to a bag valve resuscitator or emergency ventilator.

4.2.1 Performance Criteria

In order to meet the requirements described above, the following metrics are used to test the performance of the EAD prototypes. Table 4.1 summarizes the development focus and characteristics measured during each prototype stage.

Everting Pressure: Everting tubes rely on pressure within the tube to grow, and below a certain pressure, the tube will remain static. The minimum pressure required to grow depends primarily on: the area at the front of the tube, the material thickness, and the shape of the path [4]. Since this pressure may be exerted on the anatomy of the throat, it should be kept within a safe range.

Everting Forces: While eversion does not transmit shear force along the airway, the EAD can still apply forces against parts of the anatomy if the natural shape of the tube differs from the airway. These forces are related to the tube's shape and the pressure within, and they can be compared to the insertion forces of commercial devices. Minimizing these forces will result in less risk to the patient.

Airway Sealing: Breathing air pressure from resuscitation devices [90] can range from 17 cmH_2O to to well over the recommended peak of 40 cmH_2O [91]. In order to isolate

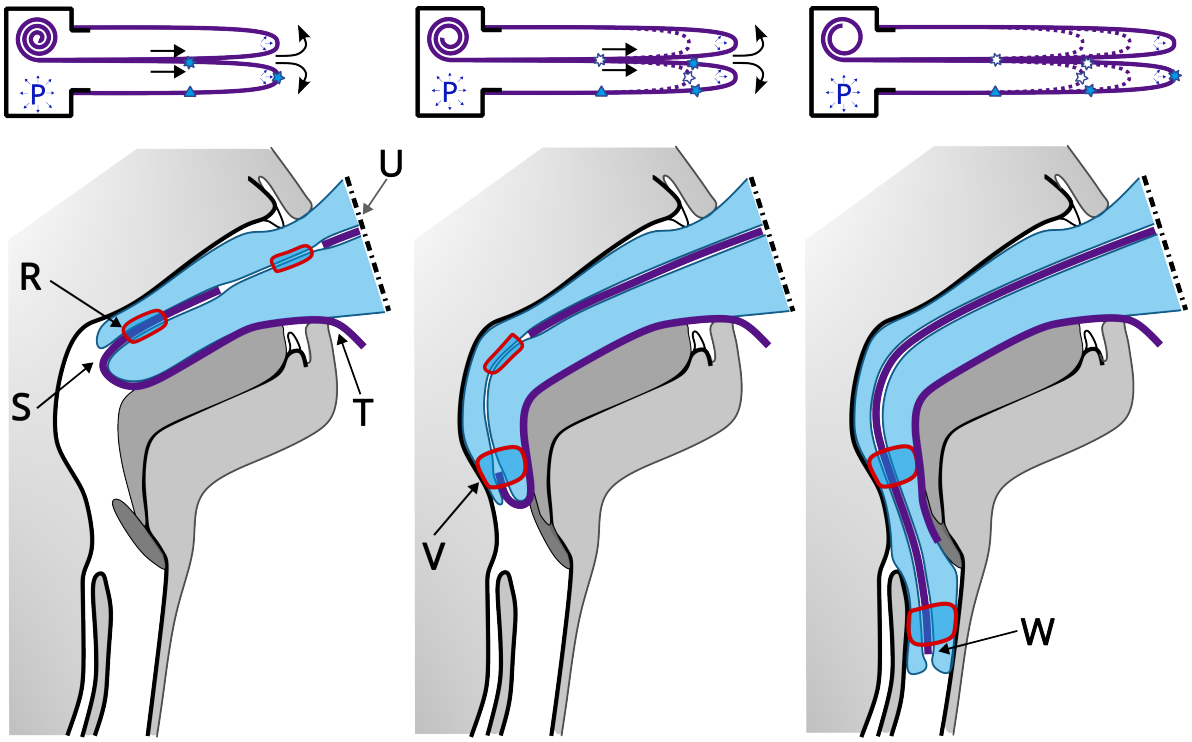

Figure 4.3: Eversion process for tracheal deployment. *Above*: An example of eversion growth from left to right. Pressure (**P**) within the base of the device causes material from the reel to travel to the front and evert to the outside of the growing tube. *Left*: The airway device has grown into the mouth. The proximal sealing cuff (**R**) is still within the device body and will be everted from the growing tip (**S**) before the end of the side air channel, which will remain on the outside of the device body (**T**) for possible connection to the breathing circuit. All of the everting body material passes from the pressurized device vessel at the exit point (**U**). *Center*: The proximal sealing cuff has been everted (**V**) and the end of the side air channel is about to evert. *Right*: The tube has grown into the trachea and everted the distal sealing cuff while the central air channel is about to evert (**W**).

breathing air flow to the lungs, it is required to provide a seal at the airway against the surrounding anatomy. Like eversion pressure, this pressure must be kept within safe limits. The quality of the seal can be measured by the ratio of the maximum pressure built up within the sealed area over the pressure applied to the sealing element. Ideally, this value is 1/1. The upper limit of sealing pressure for commercial intubation devices is 140 cmH_2O: above this limit, reduction in blood flow can cause ischemia in the surrounding tissue [92].

Burst Pressure: Minimizing eversion pressure by reducing material thickness risks lowering the burst pressure of the tube to within the operating region of tube pressures. A burst during deployment would represent a failure to intubate and, worse, could risk patient injury and asphyxiation. A burst pressure safety factor can be calculated by dividing the burst pressure of the tube by the eversion pressure required for full deployment.

Deployment Success Rate: As an emergency life-saving device, the EAD should fully deploy to an effective configuration in 100% of attempts. It is also very important for deployment to happen quickly, as the healthy brain can start to suffer from hypoxia in less than 5 minutes [93].

4.3 Prototype EAD-1

The primary goals of the EAD-1 prototype were to: 1 - investigate the general system design of the dual-deploying concept and 2 - explore the use of everting elastic elements to seal an airway. The outcome of this work was a proof of concept system for an EAD along with a series of experimental evaluations to determine the feasibility of EAD concept.

4.3.1 System Design

The EAD-1 prototype [57] consisted of 3 components. The first is the everting tube that will deploy into the patients mouth towards the airway. The tube is housed on a reel within the eversion base, which acts as a pressure vessel to propel tube growth. Finally, a pneumatic control system provides the pressure differential within the base to grow the tube and seal it in the airway after deployment. A soft silicone phantom was constructed to mimic the shape

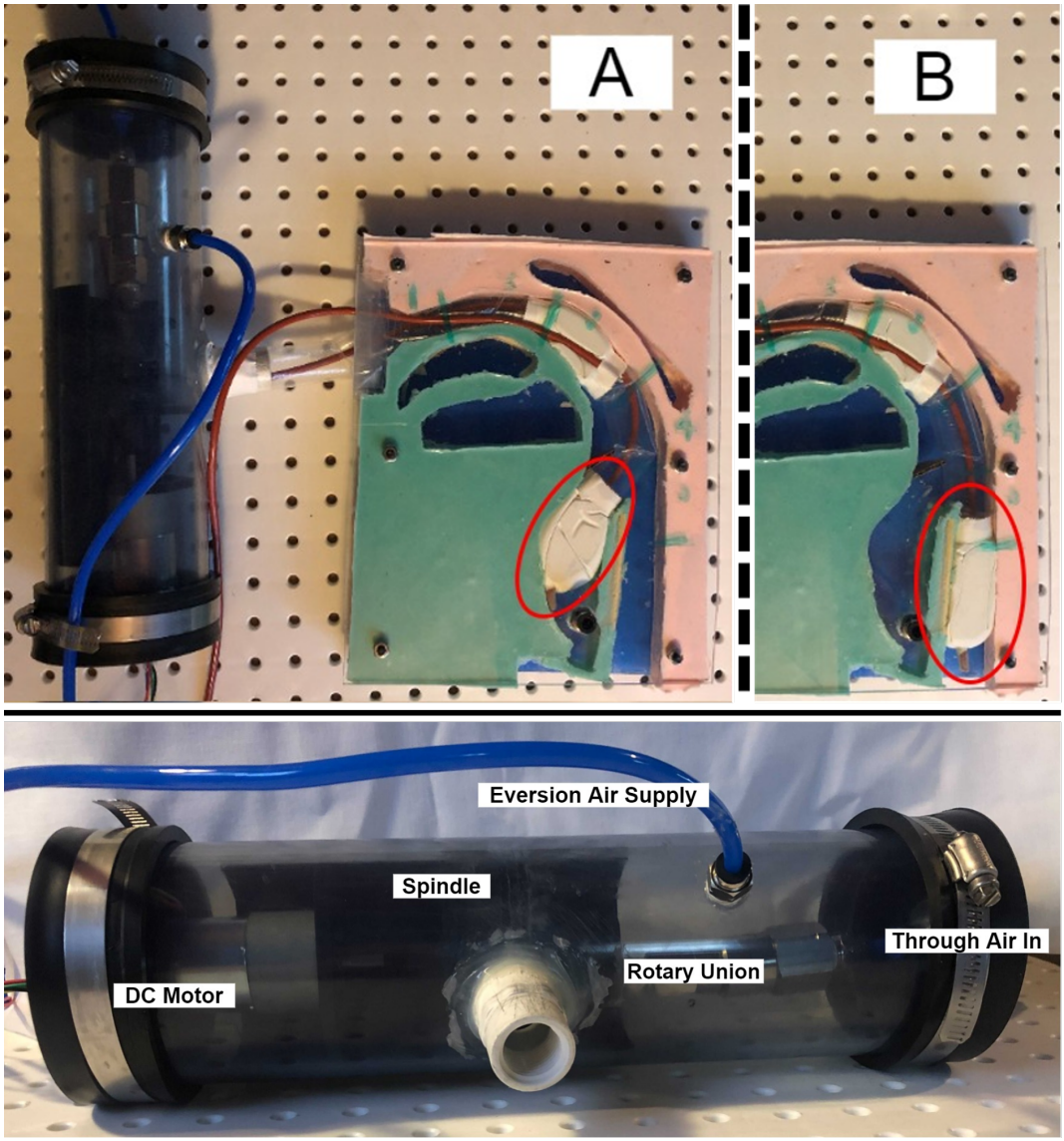

Figure 4.4: *Above*: Deployment of EAD-1. (**A**) Tube in trachea. (**B**) Tube in esophagus. *Below*: Motor controlled rotary eversion assembly with rotary union for external access to internal lumen. The spindle is mounted on bearings and also referred to as a reel.

and behavior of the airway.

The everted tube body is composed of:

- **Soft Body Tube** - thin LDPE tubing (ULINE), 1" (25 mm) diameter and 2mil (0.05mm) wall thickness;
- **Semi-Rigid Air Delivery Tube** - 3mm ID x 4mm OD latex tubing (Uxcell); and
- **Airway Sealing Balloons** - 9" (230 mm) latex balloons fixed to the soft body tube with J&J Waterproof tape.

A rotary eversion base (Figure 4.4) was adapted from `vinerobots.org` and by Hawkes et al. [62]. The soft robot body was spooled onto a reel and could be released at a constant rate by a DC motor. The reel has a through-hole allowing the Semi-Rigid Air Delivery Tube to be routed out of the pressure vessel. It is connected to a pneumatic rotary union (Mosmatic, Bristol, WI) to prevent airline kinking during reel rotation.

Pneumatic pressure is supplied by a 12V DC peristaltic pump with a manual pressure regulator (Omega, AR91-015) and a 2L pneumatic tank to act as a pressure filter. Pressure is measured with a gauge pressure transducer (Honeywell, SSCDANN150PG2A3).

4.3.2 Anatomy Phantom

A CT scan of a healthy teenage male was used to construct a simplified airway phantom (Figure 4.5). The 2x scaled airway phantom with a constant depth of 2 cm was cast using an outline of the airway. It was scaled to match the size of commercially available 2.54cm diameter tubing such that the anatomy and tube had roughly the same cross-sectional area. Silicone rubbers with durometers 20 and 15 were used (Mold Max 20 and Mold Star 15) to simulate the soft tissues of the airway. Air pockets were left in the phantom to approximate highly compliant tissues. The upper esophageal sphincter was modeled as open and does not reflect the normally closed nature of the esophagus. A single DOF epiglottis was modeled

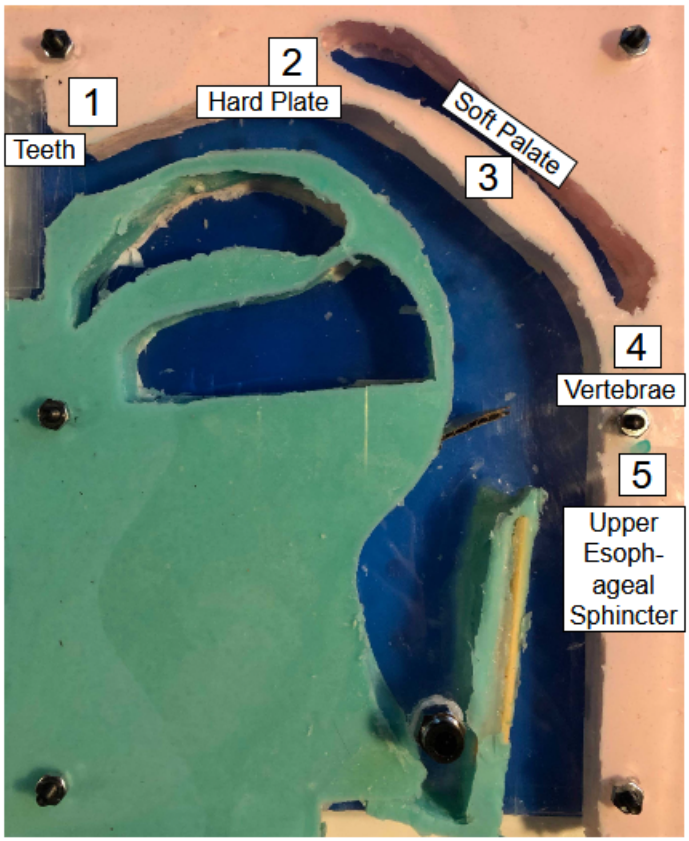

Figure 4.5: Scaled (2X) airway phantom with key anatomical areas highlighted. Hollow pockets in the silicone are included to simulate highly compliant areas of soft palate and tongue. A hinged flap simulates the epiglottis that covers the trachea during eating and drinking.

using a torsion spring to approximate the torque, 6 N-mm, required to depress the epiglottis [94].

4.3.3 Evaluation

Five tube configurations were constructed with different combinations of the features of the EAD concept. For brevity, this chapter will concentrate on the plain LDPE tube of Configuration 0 and the fully featured Configuration 4 with dual sealing balloons and air delivery channels.

Everting Pressure

The pressure required to evert the EAD-1 system was measured in both a clear, straight pipe and while deploying in the airway phantom. System pressure was manually increased until eversion started and was increased whenever growth stopped. The pipe, seen in Figure 4.6, had a diameter 45% larger than the inelastic LDPE tubing so that eversion was generally unobstructed while also constraining the growth of the elastic elements. The EAD-1 required 220 cmH_2O to evert in the straight pipe. While much of the resistance to growth was the friction within the reel and rotary union, the sealing balloons also introduced friction and required a significant amount of pressure to evert and continue growth, almost 100 cmH_2O more to grow than a plain tube. A representative time series plot of pressure data during eversion of a plain tube can be seen in Figure 4.8.

Within the airway phantom, a plain LDPE tube was everted without attachment to the reel in order to determine the pressure needed to grow past key anatomy. The pressure to evert to final deployment was 179 cmH_2O. Few of the trials resulted in successful deployment in the airway phantom and all successful deployments were in the esophagus. Growth was often unable to navigate past the soft palette without excessive pressure. During additional experiments with the fully featured EAD-1, air leaks at the balloon-tube seams hampered the tube's ability to fully deploy.

Airway Sealing

Measurement of airway sealing was performed in the same pipe as the straight eversion pressure test. Pneumatic connectors embedded in the pipe allowed for sensing the pressure supplied by each of the breathing channels. With the EAD-1 fully deployed into the pipe, the pressure within the everted tube body acted as a sealing pressure between the elastic sealing cuffs and the rigid pipe. To determine the sealing ratio along a range of sealing pressures, the internal pressure was set to a testing value before applying pressure from a separate source through one of the breathing channels. The breathing pressure was increased

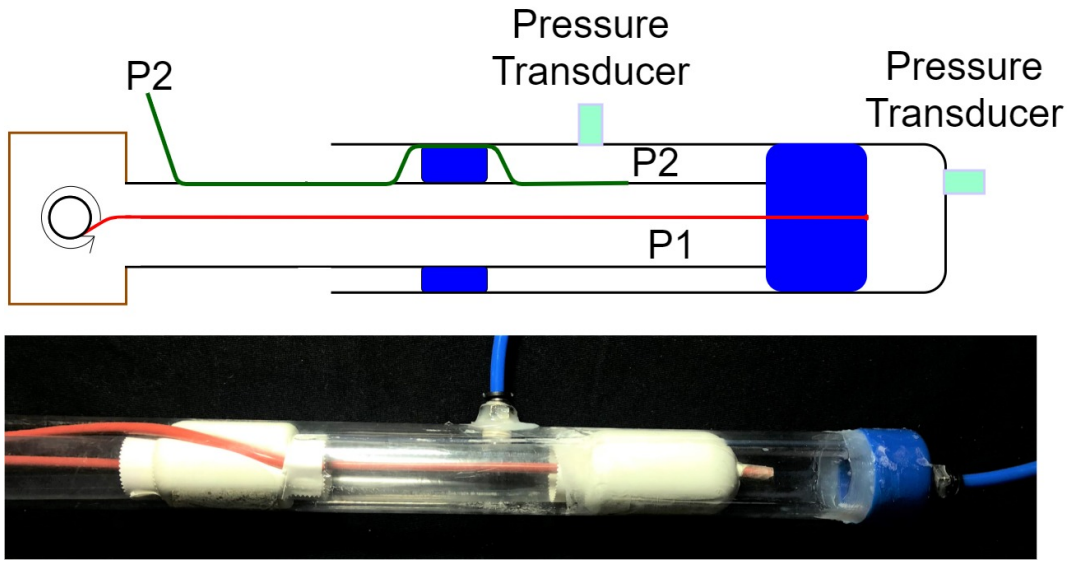

Figure 4.6: Free eversion and seal evaluation of EAD-1 within a clear, rigid tube. *Above*: Schematic of EAD-1 evaluation. *Below*: Clear rigid tube with EAD-1 deployed. The red tubes within the clear tube are the central and side breathing air channels. For EAD-2 testing, breathing pressure was introduced through the pressure transducer connections.

until the pressure sensors stopped registering an increase, indicating leakage. The EAD-1 prototype maintained a 1:1 sealing ratio from 30 to 140 cmH_2O, as seen in Figure 4.7.

4.4 Prototype EAD-2

While the EAD-1 successfully demonstrated the EAD concept by integrating everting tubes, dual elastic sealing cuffs, and air delivery channels, the prototypes needed manufacturing improvement and were not tested with an anatomically accurate airway phantom. EAD-2 development [58] focused on new construction techniques and experiments in a clinically accurate rigid airway phantom, with the aim of demonstrating safe and reliable airway deployment and sealing.

While concentrating on novel construction techniques, it was deemed prudent to limit the feature set of EAD-2. The primary difference from EAD-1 was the lack of breathing channels and the associated reel and rotary union. These features could be redesigned to fit

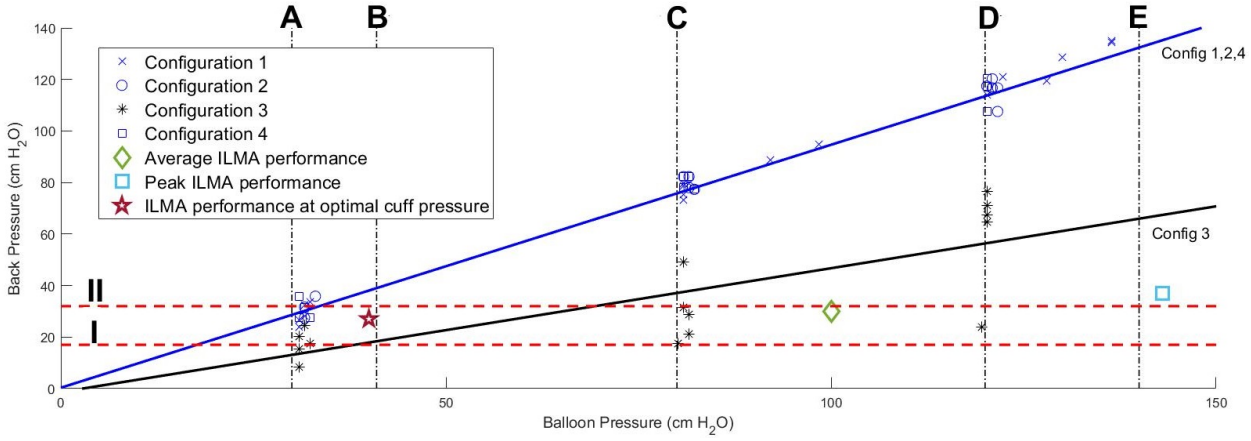

Figure 4.7: Sealing pressure of balloon configurations. Vertical bars indicate key mucosal pressure thresholds: **A**- optimal cuff pressure[92]; **B**- tracheal capillary perfusion pressures[95]; **C**- mucosal pressure at which pharyngeal capillaries collapse-[92]; **D**- advisable cuff pressure for LMA/ILMA-; and **E**- mucosal pressure at which pharyngeal mucosal perfusion stops, the patient is now at risk of ischemia. Horizontal lines represent performance of manual devices[90, 96]. **I**- peak AWP supplied by Bag-Valve-Mask. **II**- peak Airway Pressure (AWP) supplied through a ventilator.

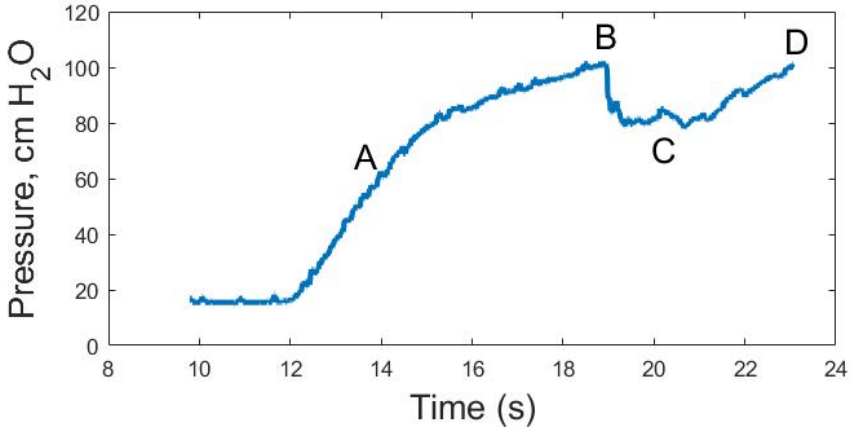

Figure 4.8: Representative time series pressure data of an everting tube. **A**- tube pressurizing (L = 0). **B**- static friction in spindle (L = 0), **C**- eversion begins, tube lengthens at constant pressure. **D**- tube is fully deployed and re-pressurizes to set point.

new tube constructions. Without the reel, the tubes under test were placed inverted into a simple pressure vessel and everted with pressure from the same regulator as EAD-1. EAD-2 tubes were also designed to fully evert, and thus do not have tails within the center running back to the pressure vessel.

4.4.1 Everting Tube Manufacturing

The everted tube bodies were composed of Thermoplastic PolyUrethane (TPU) sheets. TPU is used as the primary testing material due to its high elasticity, abrasion and acid resistance, flexibility, and sealing abilities [97]. It is also common for use in medical device applications such as in catheters and tubing [98]. These mechanical properties of TPU are important when considering the complicated geometry of throat, potential exposure to stomach acid, and abrasion exposure from teeth that the everting tube could encounter. Constructing from sheets allows for application-specific shapes and mixing of material thicknesses in one robot body. Crucially, heat sealing of TPU is more controllable than LDPE, which tends to melt and create holes quickly. Sheet-based construction also allow for investigation into optimal use of fin and lap seal (Figure 4.9); lap seals have been described as advantageous for strength without minimal decrease to tube compliance [87].

TPU sheets of 0.1 and 0.05 mm thicknesses (Plastic Film Corp. TPU-79000250, TPU-78000450M) were sealed into tubes using a 5mm heat seal roller (American International Electric, RS1) at 177°C. Unlike a clamping heat sealer[30], the roller allows for short seams and concave paths. The tubes were sealed by wrapping the sheet around a strip of thermally resistant silicone with a sheet of parchment paper between the plastic and the heat roller. The silicone layer insulates the back side of the TPU from being sealed while also conforming to the surface of the roller, ensuring a distributed seal, while the parchment paper prevents the plastic from sealing with the silicone. Longitudinal seals between sheets were either fin sealed or lap sealed (Figure 4.9). The EAD-2 tubes were manufactured to a diameter of 20 mm to be more comparable to the diameter of the human throat than EAD-1.

Like the development of EAD-1, several configurations of EAD-2 were produced to inves-

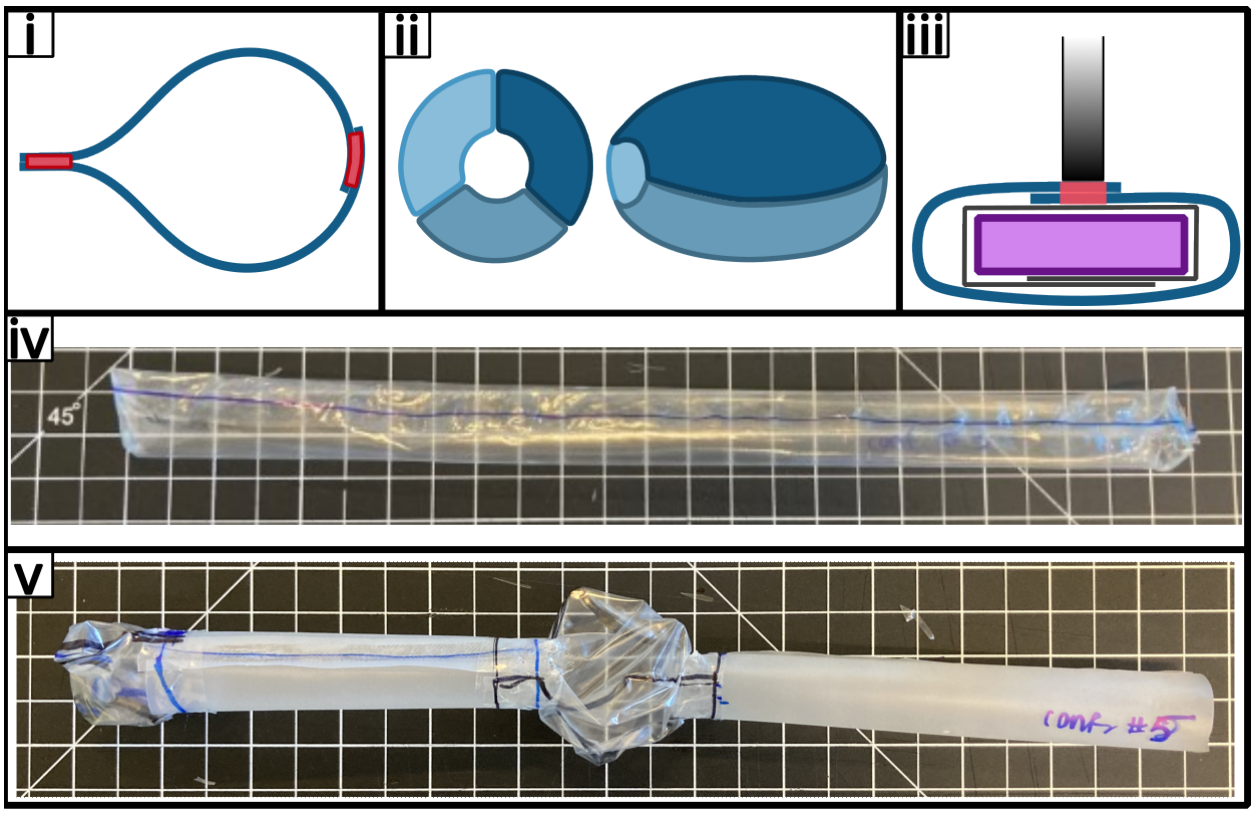

Figure 4.9: Tube construction methods. (***i***): Example fin seal (left) and lap seal (right). (***ii***): Front and side views of 3-piece sealing cuff. Each section is an identical circle. The material at the center opening is lap sealed to the main tube body, as seen in ***v***. (***iii***): Heated roller sealing of a lap seal. TPU is wrapped around an insulated core of parchment paper and silicone rubber (purple). The heated roller (black) is rolled along the length of the seal. (***iv***): Configuration 3 with thin TPU and lap seal. (***v***): Configuration 5 with thicker TPU body and thin TPU cuffs. The body sections are connected with narrow material to prevent elongation of the body during cuff inflation. (This paper considers Config. 6 with thin TPU body and cuffs.)

tigate design choices and feature construction. Of the seven configurations that were tested, this paper will focus on the following configurations because they demonstrated the most promise with lower eversion pressures:

- Config. 3 - Thin Lap: 0.05mm TPU with lap seal,
- Config. 6 - Thin w/ Cuffs: 0.05mm TPU with lap seal and 0.05mm sealing cuffs, and
- Config. 7 - Thin Curved: 0.05mm TPU with fin seals and 115° curve to mimic the shape of the airway phantom.

The cuffs on Config. 6 were designed with inspiration from the CombiTube device and were constructed from sheets cut into 51 mm and 25 mm circles. These circles were derived from measurements of cuff inflation at 12 mL for the distal cuff and 50-75 mL for the proximal cuff [99]. Three circular sheets were patchwork sealed in a sphere formation with a heat roller (Figure 4.9-ii), leaving a hole at the top and bottom that was the same diameter as the tube. To prevent the elastic elongation at the cuffs during growth seen with EAD-1, two longitudinal 6mm-wide strips were left in the main body tube underneath the spherical cuffs. Use of TPU instead of latex balloons as sealing cuffs contributes to a more predictable deployment, as the balloons required significant pressure buildup and resulted in very fast eversion after balloon deployment. Sizing the volume of the sealing cuffs to be larger than the throat and trachea should ensure a reliable seal.

4.4.2 Anatomy Phantom

MRI and CT imaging was previously used to collect 3D tissue data of a standard patient's anatomy for AJAMS [100]. The required airway structures for EAD testing were identified and converted to 3D anatomical structures. The airway phantom included accurate anatomy including teeth, mouth, pharynx, larynx, esophagus, and trachea (Figure 4.10). The phantom was bisected one centimeter past the midline sagittal plane prior to being 3D printed (Prusa

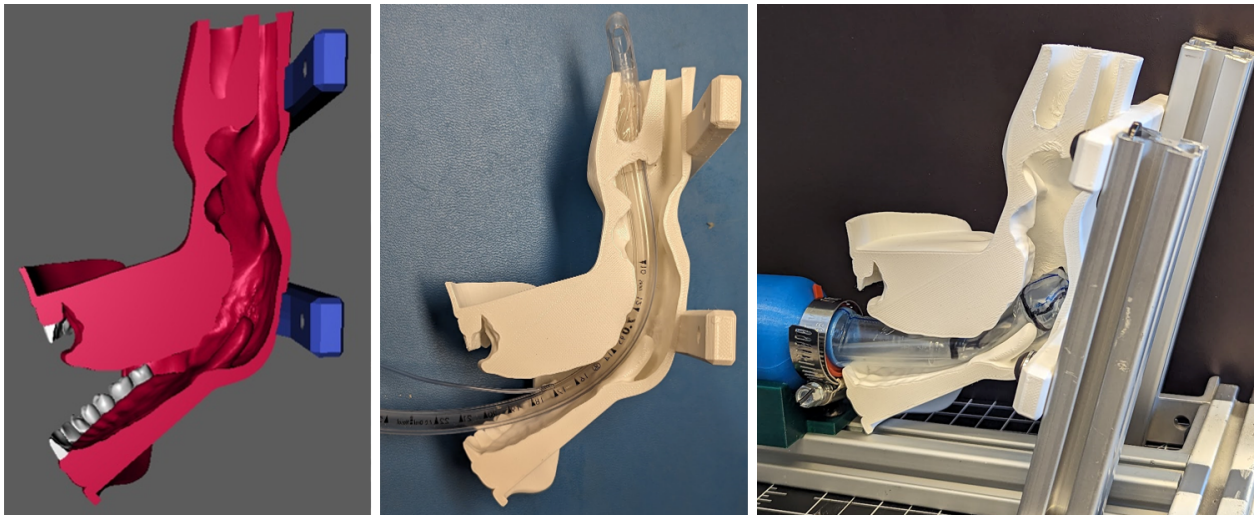

Figure 4.10: Bisected, patient-specific airway phantom used to test the everting emergency airway device. *Left*: Isolation of the essential anatomy from design models of the male AJAMS model. *Center*: Rigid printed airway phantom used in airway tests with clinical endotracheal intubation tube. *Right*: Phantom with plain tube everting past the uvula.

i3Mk3) in PLA. This bisection maintains most of the cross sectional area and features of the airway while allowing visualization of tube growth. The positioning of the anatomy is the natural resting pose of the scanned human, and not in the straighter airway pose that EMT's will try to achieve for ET intubation. The epiglottis was not included in the printed model so that initial investigations of device shape and airway sealing could be investigated without the challenge of compensating for a soft and reactive epiglottis.

Everting Pressure

The everting pressures for EAD-2 were collected using the same procedure as EAD-1, with a 23mm straight pipe and the new AJAMS-derived aiwary anatomy phantom. The plain thin tube, Config. 3, had a straight eversion pressure of 74 cmH_2O, and the addition of cuffs in Config. 6 required 89 cmH_2O. In the airway phantom, Config. 6 required 323 cmH_2O and the curved design without cuffs, Config. 7, required 126 cmH_2O.

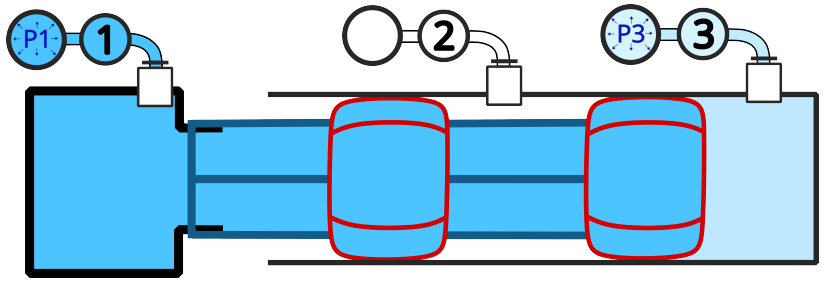

Figure 4.11: Straight airway sealing setup for EAD-2. Unlike EAD-1, EAD-2 did not include breathing channels, and simulated breathing pressure was supplied externally. Note: EAD-2 was not everted from a reel, and does not have the "tail" seen between the tube tip and the reel as in the top of Figure 4.3.

Airway Sealing

The same pipe with pneumatic connectors that was used for EAD-1's airway sealing was used to test airway sealing of EAD-2. Since EAD-2 did not have breathing channels, breathing air pressure was simulated by attaching a pressure source and sensor to the connections of the pipe, as seen in Figure 4.11. Thus, sealing pressure could be maintained in the EAD-2 Config. 6 body while an independent breathing pressure could be increased within a sealed chamber of the pipe until a steady state was achieved. With sealing pressures ranging from 90 to 150 cmH_2O, the sealing ratio was 1.3:1. Below this range, sealing required a much higher relative pressure. It was noted that small leaks in the seams between TPU sheets were present and may have decreased the airway sealing performance. In order to seal the peak recommended ventilation pressure of 40 cmH_2O, a cuff pressure of 52 cmH_2O would be required, which is below the level that could cause of pharyngeal capillary collapse [92].

Burst Pressure

After all other testing was complete, the burst pressure was assessed by freely everting Config. 3 in free space and increasing the air pressure until the tube burst. The peak airway pressure attained was 360 cmH_2O, 4.9 times its average eversion pressure.

4.5 Prototype EAD-3

The development of EAD-2 resulted in a promising advance in the EAD manufacturing process and also uncovered the advantages of shaping a tube for the airway. As shown in [9], pre-shaping an everting tube can greatly reduce the pressure to evert and the force applied on the surrounding tissue. Since the new manufacturing methods of EAD-2 allowed for easy prototyping of tubes with complex shapes, it was decided to focus on the effects of pre-shaping on eversion pressure, eversion forces, and the ability to reliably deploy into the trachea. With very high tracheal deployment success, a commercial EAD could be simplified to a single sealing cuff and central air channel. With the focus on deployment, the EAD-3 prototypes did not include sealing cuffs.

4.5.1 Manufacturing

While the EAD-2 manufacturing method opened new possibilities in everting tube construction, it was time consuming and still prone to over- or under-heating the seals. Inspired by a semi-autonomous method for creating small, straight everting tubes with stepper motors and a clamping heat sealer [30], a method was devised to use a 3D printer (Prusa i3Mk3) to seal two sheets of TPU together with the desired tube outline (Figure 4.12. Similar methods have been used for creating soft robots using 3D printers, with mixed success, [101] and welding with laser cutters [102], and recently, laser welding has been specifically studied for everting tubes [103]. Our method involves sandwiching two sheets of TPU between two sheets of parchment paper and fixing the stack to the print bed with magnets after the printer has completed bed level calibration. The tube outline is designed as a shape with 0.4mm height and sliced to print with PLA. The printer was set move at 10 mm/s at 215° C extruder and 60° C bed temperature. During printing, the extruder tip contacts the material stack and effectively seals the TPU sheets with a strong, uniform seam.

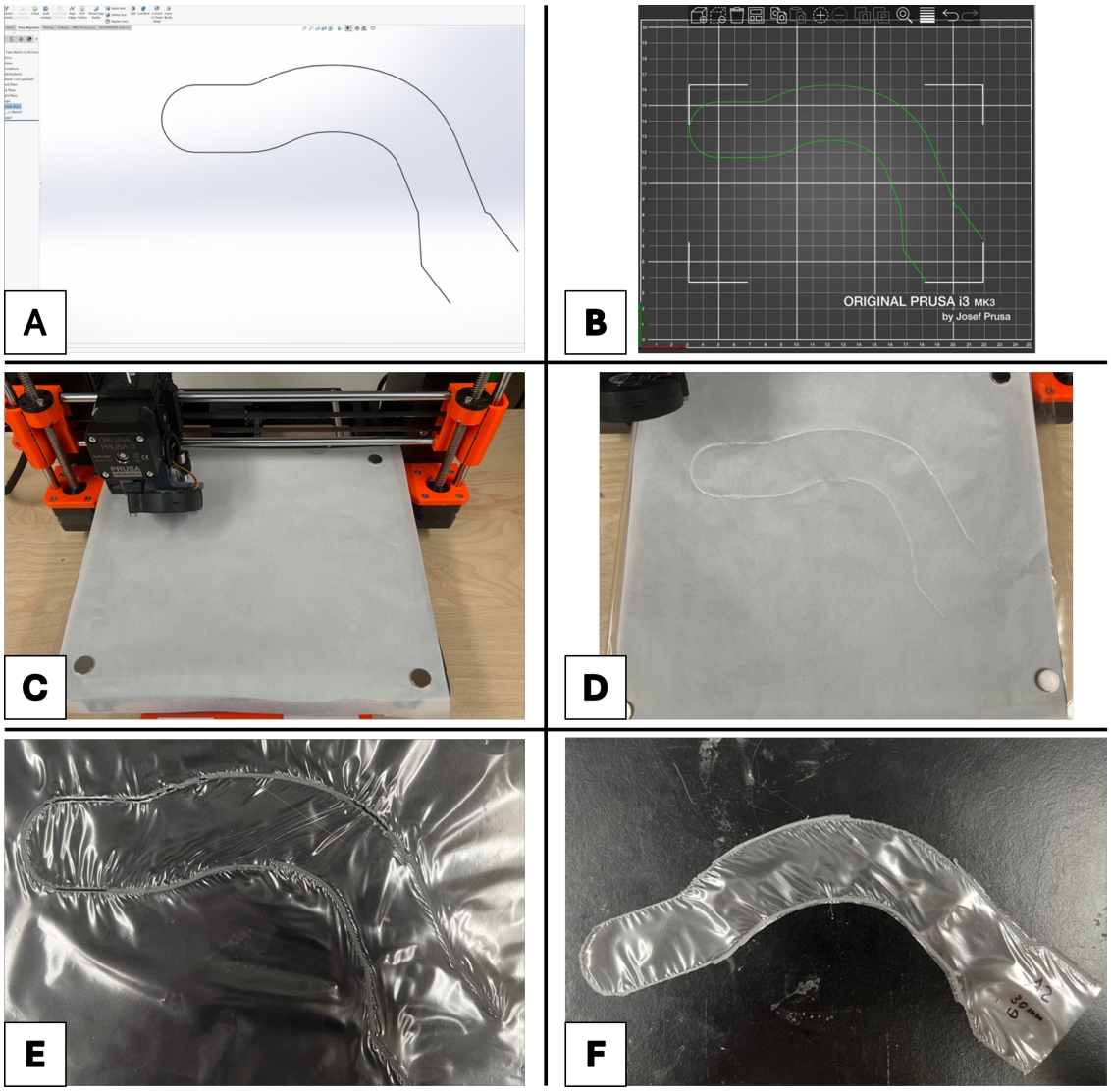

Figure 4.12: EAD-3 manufacturing process. **A**: Outline of desired seam in CAD. **B**: STL file of outline imported into PrusaSlicer. **C**: Sheets of TPU sandwiched between parchment paper on Pruska MKS3+. **D**: Sealing path of tube shape. **E**: Sealed tube before cutting. **F**: New tube after excess material is cut away.

4.5.2 Anatomy Phantom and Pre-Curved Tubes

To study the deployment characteristics of EAD-3, a simplified 2.5D version of the earlier AJAMS-derived phantom was created from its airway outline (Figure 4.13). A minor change was made to slightly widen the distal end of the trachea channel, but not the larynx, so that both the trachea and esophagus had equal widths, which allowed for easier comparisons of everting pressure. The phantom was covered with a thin sheet of clear polycarbonate and then mounted to an ATI Axia80-M8 6-axis force/torque sensor. The serial output for the force sensor was collected synchronously with the air pressure data using a python script.

A simple curved tube was designed to mimic the shape of the phantom airway through the trachea (Figure 4.13). It was discovered that a constant tube diameter of 13 mm would easily fit within the phantom without being oversized. A straight control tube was designed with the same width. The straight and curved tubes can be seen in Figure 4.14.

4.5.3 Evaluation

The study of deployment characteristics was extended to investigate the effects of the angle of tube insertion. It is important to know if there is an optimal insertion angle for either of the tube designs, or if either of the designs has only a small region of acceptable alignment. The force sensor was mounted on top of a base with mounting holes that allowed for rotation in 15° increments about a point near the center of the mouth opening with a range of ±30°.

Everting Pressure

An electro-pneumatic digital air pressure regulator (SMC ITV2010-04N2N4) was used to increment the system pressure by 14 cmH_2O with the push of a button. Starting at an insertion angle of 0°, each tube was mounted to the eversion base, and after a short calibration pause, pressure was increased until eversion began. Pressure was increased after growth pauses until the tube was fully deployed or a maximum pressure of 250 cmH_2O was reached. After 5 trials at 0° with a curved and straight tube, the phantom was rotated and the process

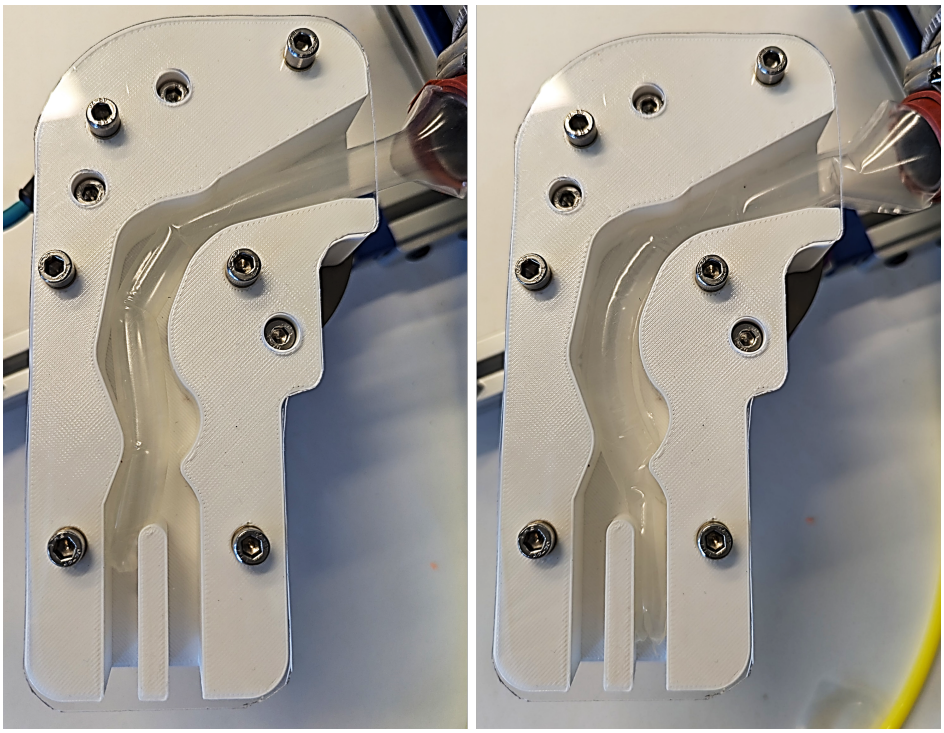

Figure 4.13: Deployment of a straight tube into the esophagus (left) and a curved tube deployed into the trachea (right) in the EAD-3 airway phantom. The phantom is mounted to the XY plane of an ATI force sensor and the assembly is capable of rotating ±30◦ about a point near the center of the mouth with the Z axis pointed towards the reader.

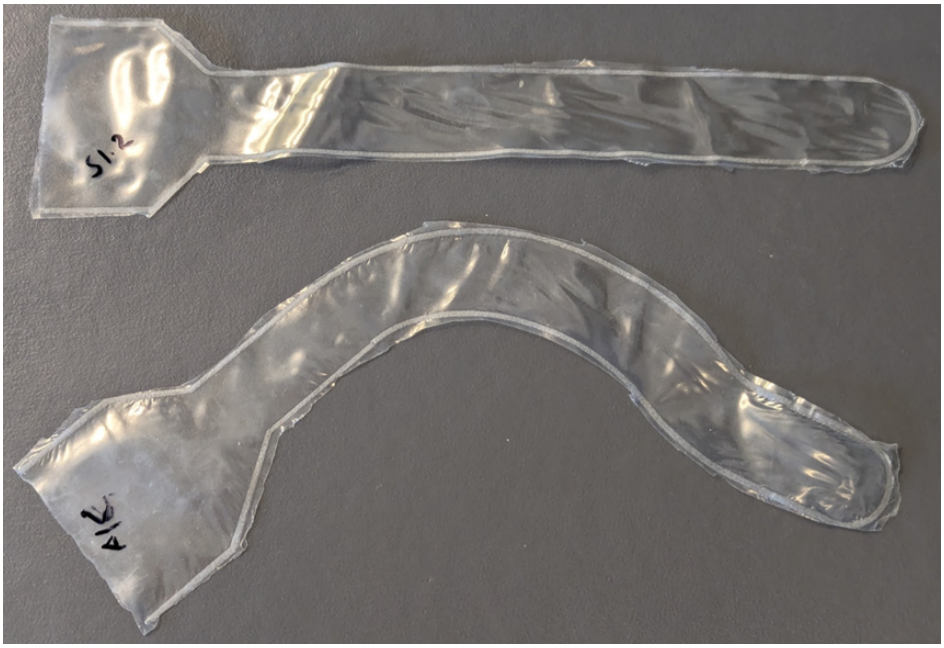

Figure 4.14: EAD-3 straight control tube (above) and curved tube (below) designed to deploy to the trachea.

repeated. After testing up to ±30°, a final set of 5 trials was completed at 0°. With a total of 30 trials for each tube, there was a noticeable decrease in everting pressure due to wear from the first set at 0° to the second set. The decrease in pressure per trial was fit using a linear function and then applied to all of the eversion pressure data in order to make a wear-compensated comparison between trials. The decrease in everting pressure was found to be 1.3 cmH_2O and 3.4 cmH_2O per trial for the curved and straight tubes respectively.

The maximum, wear-compensated pressures needed to fully deploy each tube can be seen in Figure 4.15. The curved tube exhibited a clear relationship with changing insertion angle, but the magnitude was fairly small and the average pressure for all trials was 111 cmH_2O, with the minimum at 0°. The straight tube exhibited a less clear relationship with higher ranges of everting pressures, averaging to 179 $cmH_2O$with a minimum at 30°.

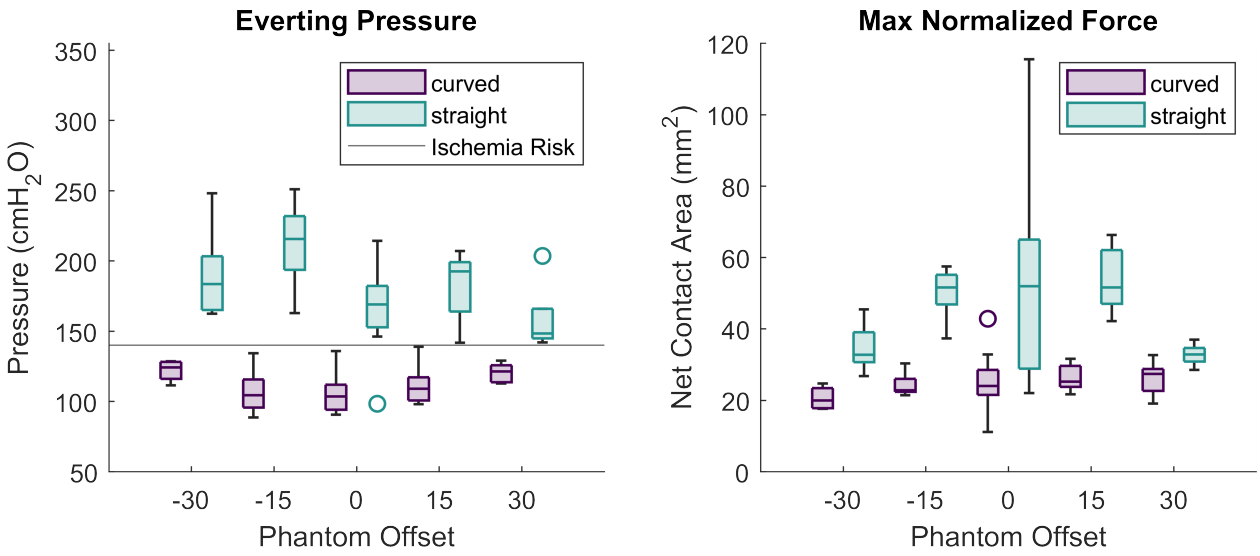

Figure 4.15: Maximum everting pressure (*left*) and normalized max force (*right*) during phantom deployment. The everting pressure is the pressure that was required to fully deploy a tube within the airway phantom. The magnitude of force is represented by the net area of contact between the tube and the anatomy. A higher area will apply more force per unit pressure.

Everting Forces

The norm of forces on the phantom recorded during everting pressure trials give an estimate of the effects that tube shape have on the force applied to the tissue of the airway during deployment. Since there is a significant difference in the pressures applied during the straight and curved tube trials, it is expected that the applied force will be proportional. However, by dividing the maximum force in each trial by the pressure in the system at the time of that force reading, a normalized metric of area units is calculated. This area is effectively the net area in contact with the phantom. Figure 4.15 shows a considerable difference between the contact areas of the two tube designs. At the same pressure, the straight tube will apply more force on the tissue than the curved tube. This effect compounds with the increased pressure required to deploy the straight tube.

A commercial AED will likely be operated at a constant pressure that will reliably deploy the tube. Since the everting pressure trials do not occur at a constant pressure throughout, the maximum force during these trials is not a true reflection of the forces during clinical deployment. To determine maximum forces during nominal deployment, a new set of tubes was deployed 3 times each at 0° with a pressure 25% higher than their average everting pressures. The average maximum force applied by the curved tube was 0.26 N at 140 cmH_2O, and the straight tube applied 1.25 N at 225 cmH_2O.

Burst Pressure

After everting 30 times each during the everting pressure trials, the two tubes were gradually pressurized until bursting. Both the curved and straight tubes achieved a maximum pressure of 323 cmH_2O before bursting at the seam near the corner where the tube reduces in diameter from the eversion base. With the lower everting pressure, the burst safety factor for the curved tube is 2.9.

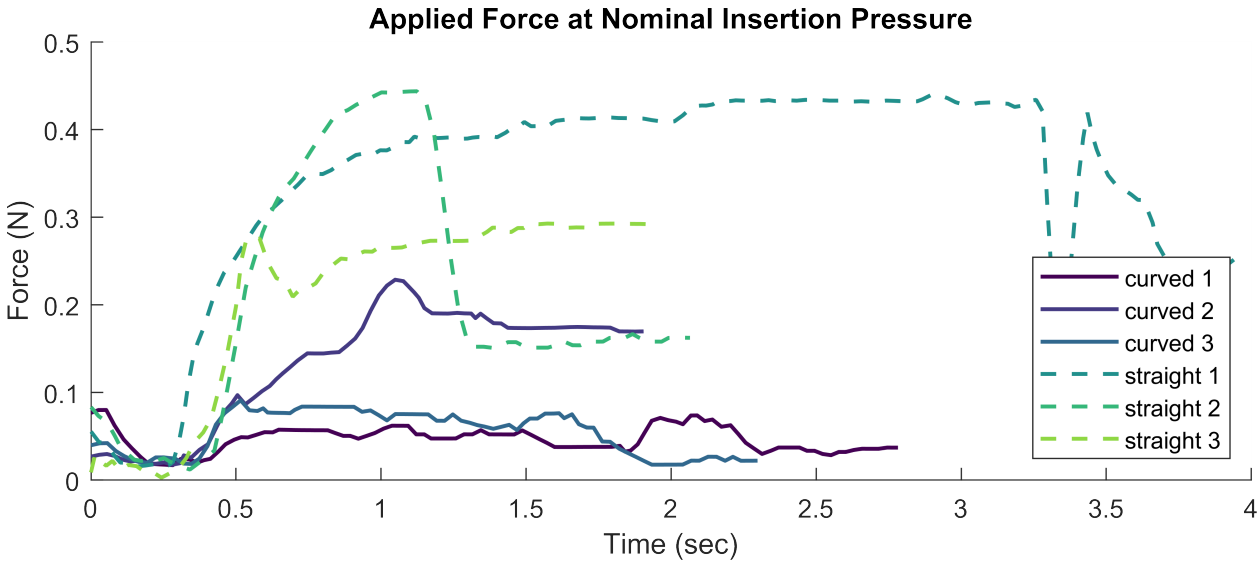

Figure 4.16: Norm of XY force during everting forces trials at constant pressure.

Deployment Success

At the end of each everting pressure and force trial, the final deployed position was recorded. All 66 trials resulted in full deployment in the trachea or esophagus. Nearly all straight tubes achieved esophageal deployment, and some deployed into the trachea. The specific rates for tracheal deployment can be seen in Table 4.2 and the most common deployments can be seen in Figure 4.4. The average deployment time for each tube in the constant-pressure everting forces trials was under 3 seconds.

4.6 Discussion

Each step in the EAD development has shown improvement in manufacturing techniques and nearly all performance metrics. Table 4.3 summarizes the most relevant comparisons between EAD prototypes and commercial devices. The following sections will detail these comparisons.

Table 4.2: Instances of Tracheal Deployment During Everting Pressure Trials

Offset	**Tracheal Deployment Rate**		**Trials Per Tube**
	Straight	**Curved**	
-30	0%	100%	5
-15	20%	100%	5
0	10%	100%	10
15	0%	100%	5
30	0%	100%	5

Table 4.3: Comparison of Commercial and EAD Devices

Metric	**Comm.**	**EAD-1**	**EAD-2**	**EAD-3**
Insertion Pressure (cmH2O)	714-1326	179	126	111
Insertion Forces (N)	20-39			0.25
Airway Sealing Ratio	1.54	1.0	1.3	
Burst Pressure Safety Factor			4.7	2.9
Deployment Success	0-100%	Low		66/66

4.6.1 Everting Pressure

The everting pressure for tubes without sealing elements or reel friction are reported in Table 4.3, and show a downward trend. Generally, identical tubes of smaller diameters require higher pressure to evert, but the EAD designs required less pressure with smaller diameters. This is likely due to improved manufacturing and pre-shaping the tubes to the anatomy. The air pockets in the silicone phantom were particularly difficult to navigate for the straight EAD-1 prototype. Since the risk of ischemia is primarily associated with prolonged pressure on the anatomy, this level (140 cmH_2O) is a reasonable magnitude for eversion design.

In a study of intubation in Laerdal manikins, the average pressure applied on the tissues of the upper airway by anaesthesiologists with the tip of laryngoscope blades ranged from 714-1326 cmH_2O [104]. As the laryngoscope is a key step for gold standard intubation with an ETI, the EAD has the potential to pose significantly less risk of airway trauma during emergencies.

4.6.2 Everting Forces

In the same study comparing laryngoscope forces [104], the forces applied on the anatomy were about 100 times those measured with EAD-3. While this is a promising comparison, the EAD-3 test for eversion forces measured only the resultant force from all distributed contact between the tube and the phantom. The laryngoscope study measured force applied with a specific area at the tip of the blade. A more apt future comparison would involve distributed pressure or force sensing along the everting tube or within sensitive areas of the airway phantom. Another useful metric for understanding the forces of everting tubes is the force at the tip of the tube: the curved tube everting pressure multiplied by the area of the tube tip gives a force of 5.7 N.

4.6.3 Airway Sealing

While the airway sealing ratio of EAD-2 was not as effective as EAD-1, it was still more efficient than the most optimal performance of an Intubating LMA (ILMA) as reported in [95]. An elastic sealing cuff may be the most effective in EAD testing, but the challenges of sealing multiple materials and controlling the eversion properties have been difficult to overcome. The sealing ratios of the ILMA are plotted in Figure 7 of the EAD-1 study [57] and were measured during human trials with sensorized sealing cuffs.

4.6.4 Burst Pressure

The EAD-3 prototype achieved a burst pressure safety factor close to that of EAD-2 after 30 trials. It is reasonable to believe that the EAD-3 safety factor would improve with less wear and with wider curve radii at corners. However, as more features are added to the EAD-3 design and as more difficult airways are attempted, everting pressure may rise, so careful attention should be paid to the burst safety factor.

4.6.5 Deployment Success

Improvements in manufacturing and the easier to navigate rigid airway phantom led to 100% deployment success with EAD-3 regardless of tube shape or angular alignment. EAD-3's ability to navigate with a wide range of angular alignment shows promise for being able to successfully deploy in real-life scenarios with varying users and patient anatomy. While the curved tube was able to quickly and reliably deploy within the trachea of the airway phantom, more varied testing is required to determine if the Combitube-like dual deployment strategy can be abandoned in favor of a simpler trachea-only design. Another key limitation of the EAD-3 deployment test is the lack of a flexible and reactive epiglottis, which could prevent some deployment into the trachea.

4.6.6 Future Work

Each of the pilot studies of the EAD-1 and -2 prototypes have been performed with limited, painstakingly manufactured prototypes. As customizable everting tube production becomes more time efficient with the introduction of 3D printer sealing, testing of more copies and more configurations is possible. While the size of tubes created with this method is limited to the bed size, future work is underway to try to use 3D printers with a conveyor belt bed that achieves an "infinite z" axis.

The sealing cuffs of EAD-2 Config. 6 required significantly higher eversion pressure within the airway phantom compared to the plain Config. 3. A key challenge for future designs will be the optimal design of sealing cuffs. The sealing cuffs of EAD-2 have 3D features, so further innovation is required to use the 2D sealing methods of EAD-3.

Additional future work involves significant focus on each of the requirements and metrics discussed above. Re-integration of the airway channels will require sufficiently low airway resistance for breathing air delivery while maintaining deployment performance. Higher fidelity soft tissue models, such as those of the AJAMS trainer, will be required to more accurately understand the behavior of the EAD in a human airway.

4.7 Conclusion

The iterations of the EAD concept have shown promise for every proposed performance metric in addition to introducing several novel manufacturing techniques for everting tube robots. Recent experiments have also replicated the interaction force advantages of pre-shaped everting tubes in addition to investigating the deployment success rate under angular misalignment. While there remains considerable development before clinical trials and commercialization, there is promise in the EAD approach for enabling minimally trained bystanders to establish airways in emergencies.

Chapter 5
CONCLUSION

This dissertation encompasses an effort to understand how everting tubes behave and how those behaviors can be used and adapted for future applications. Academic interest in everting tubes has grown significantly since this work began, and there remains a lot of enthusiasm for the potential applications of this technology. The Emergency Airway Device detailed in Chapter 4 has proven through multiple iterations of development and testing to be a promising approach to a real-world problem. The specific contributions of this work to the understanding and application of everting tube robots are:

1. A description of reel-based position error during dynamic tube growth and experimentally proven solution for reducing this error;

2. A real time, mm-scale position sensing design for tube tip estimation using a Time of Flight sensor and PTFE adjunct;

3. An extended everting tube growth model that accounts for physical reel characteristics;

4. A novel measurement of the length dependence of minimum eversion pressure;

5. Estimation of static and dynamic friction coefficients for an everting tube gorwing over a working channel;

6. A series of prototypes for an everting Emergency Airway Device that have the capacity to meet functional and clinical requirements for commercial deployment; and

7. Description of several novel ways of prototyping and manufacturing everting tubes from plain sheets of plastic.

Future work informed by this thesis may seek to understand more about how the properties of the mechanical and pneumatic components within the everting robot system affect the dynamics of eversion. For instance, Chapter 2 found that the air flow available to the everting tube was insufficient to sustain the rate of growth at the required pressure. As yet, there are no proposed models for eversion that account for the flow of air into the system. In Chapter 3, a length dependency to minimum eversion force is measured but a cause is not definitively identified. While [4] presents an explanation for length dependence, more robust analysis of the phenomena is warranted.

The analysis techniques of Chapter 3 should be replicated in order to evaluate material combinations that may be relevant for medical applications. These experiments should also be extended to evaluate methods for reducing the friction between an everting introducer and a working channel. The feedback control system developed for these experiments is also capable of investigations into pressure-based feedforward or feedback control experiments.

While development of the EAD for commercial distribution will continue, there is also great potential in the 3D printer-based manufacturing technique for everting tubes. Early prototypes constructed with this technique have shown that mixing of materials thicknesses can influence pressure-dependent behavior, much like the pneumatic muscles of other soft robots. With the ability to prototype new everting tube designs within minutes, it will be much easier to explore exciting new designs for everting tubes.

5.1 Published Work

1. Andrew Lewis, Joel Hwee, Grace O'Connor, Alex Gong, Daniel M. Burke, Randall A. Bly, Kris S. Moe, Waleed M. Abuzeid, Eric Seibel, and Blake Hannaford. Design evolution of an emergancy airway device. *Journal of Medical Robotics Research*, 2024. Under Review

2. Andrew Lewis, Eric Seibel, and Blake Hannaford. Using friction to improve growth estimation of reel-mounted everting robots. *In Preparation*, 2024

3. Andrew Lewis and Blake Hannaford. Characterizing an everting tube's working channel friction. *In Preparation*, 2024

4. Grace O'Connor, Andrew **Lewis**, Alex Gong, Daniel Burke, and Blake Hannaford. Manufacturing and design improvements of an everting airway device prototype. In *2024 International Symposium on Medical Robotics (ISMR)*, pages 1–7, 2024

5. Pengcheng Chen, Nicole M Gunderson, Andrew Lewis, Jason R Speich, Michael P Porter, and Eric J Seibel. Enabling rapid and high-quality 3d scene reconstruction in cystoscopy through neural radiance fields. In *Medical Imaging 2024: Image-Guided Procedures, Robotic Interventions, and Modeling*, volume 12928, pages 350–359. SPIE, 2024

6. Allison Raines, Andrew Lewis, Joel Hwee, and Blake Hannaford. Inferring environmental interactions of soft everting robots from acoustic signals. In *2023 IEEE International Conference on Soft Robotics (RoboSoft)*, pages 1–6. IEEE, 2023

7. Chen Gong, Yaxuan Zhou, Andrew Lewis, Pengcheng Chen, Jason R Speich, Michael P Porter, Blake Hannaford, and Eric J Seibel. Real-time camera localization during robot-assisted telecystoscopy for bladder cancer surveillance. *Journal of Medical Robotics Research*, 2022

8. Pengcheng Chen, Chen Gong, Andrew **Lewis**, Yaxuan Zhou, Seyed Mohammad, Mohaghegh Poor, Blake Hannaford, and Eric J Seibel. Real-time flexible endoscope navigation within bladder phantom having sparse non-distinct features is enhanced with robotic control. In *SPIE Medical Imaging*, page [**Best Student Paper Finalist**], San Diego, CA, USA, 2022. SPIE

9. Andrew **Lewis***, Chen Gong*, Yaxuan Zhou, Pengcheng Chen, Michael P Porter, Blake Hannaford, and Eric J Seibel. Real Time Localization of Cystoscope Angulation in 2D Bladder Phantom for Telecystoscopy. In *International Symposium on Medical Robotics (ISMR)*, page [**Best Paper award**], Atlanta, GA, USA, 2021. IEEE

10. Joel Hwee, Andrew **Lewis**, Allison Raines, and Blake Hannaford. Kinematic modeling of a soft everting robot from inflated beam theory. In *2023 IEEE International Conference on Soft Robotics (RoboSoft)*, pages 1–6. IEEE, 2023

11. Joel Hwee, Andrew **Lewis**, Randall A Bly, Kris S Moe, and Blake Hannaford. An Everting Emergency Airway Device. In *International Symposium on Medical Robotics*, Atlanta, GA, USA, 2021. IEEE

12. Muneaki Miyasaka, Mohammad Haghighipanah, Yangming Li, Joseph Matheson, Andrew **Lewis**, and Blake Hannaford. Modeling Cable-Driven Robot With Hysteresis and Cable – Pulley Network Friction. *IEEE/ASME Transactions on Mechatronics*, 25(2):1095–1104, 2020

13. Yun-hsuan Su, Adnan Munawar, Anton Deguet, Andrew **Lewis**, Kyle Lindgren, Yangming Li, Russell H Taylor, Gregory S Fischer, Blake Hannaford, Peter Kazanzides, and A Background. Collaborative Robotics Toolkit (CRTK): Open Software Framework for Surgical Robotics Research. In *IEEE International Conference on Robotic Computing (IRC)*, pages 48–55, Taichung, Taiwan, 2020

14. Andrew **Lewis**, David Drajeske, John Raiti, Angelique Berens, Jacob Rosen, and Blake Hannaford. RAVEN-S: Design and Simulation of a Robot for Teleoperated Microgravity Rodent Dissection under Time Delay. In *Proceedings - IEEE International Conference on Robotics and Automation*, pages 11332–11337, 2020

15. Yangming Li, Shuai Li, David Caballero, Muneaki Miyasaka, Andrew **Lewis**, and Blake

Hannaford. Improving control precision and motion adaptiveness for surgical robot with recurrent neural network. In *IEEE International Conference on Intelligent Robots and Systems*, volume 2017-Septe, pages 3538–3543, Vancouver, BC, Canada, 2017. IEEE

16. Muneaki Miyasaka, Joseph Matheson, Andrew **Lewis**, and Blake Hannaford. Measurement of the Cable-Pulley Coulomb and Viscous Friction for a Cable-Driven Surgical Robotic System. *2015 IEEE/RSJ International Conference on Intelligent Robots and Systems (IROS)*, pages 804–810, 2015

17. Homa Alemzadeh, Daniel Chen, Andrew **Lewis**, Zbigniew Kalbarczyk, and Ravishankar Iyer. Systems-Theoretic Safety Assessment of Robotic Telesurgical Systems Systems-theoretic Safety Assessment of Robotic Telesurgical Systems. In *SAFECOMP*, 2015

18. Deanna Glassman, Lee White, Andrew **Lewis**, Hawkeye King, Alicia Clarke, Thomas Glassman, Bryan Comstock, Blake Hannaford, and Thomas S Lendvay. Raven surgical robot training in preparation for da vinci. *Studies in health technology and informatics*, 196:135–41, 2014

19. Andrew **Lewis** and Blake Hannaford. Dynamically evaluated gravity compensation for the RAVEN surgical robot. In *2014 IEEE International Conference on Robotics and Automation (ICRA)*, pages 2534–2539. IEEE, may 2014

20. Daniel Jones, Andrew **Lewis**, and Gregory S. Fischer. Development of a standalone surgical haptic arm. *Proceedings of the Annual International Conference of the IEEE Engineering in Medicine and Biology Society, EMBS*, pages 2136–2139, 2011

21. Brandon Ingram, Daniel Jones, Andrew **Lewis**, Matthew Richards, Charles Rich, and Lance Schachterle. A Code of Ethics For Robotics Engineers. In *ACM/IEEE international conference on Human-robot interaction*, pages 103–104. ACM, 2010

BIBLIOGRAPHY

[1] Simon DiMaio, Mike Hanuschik, and Usha Kreaden. The da vinci surgical system. In Jacob Rosen, Blake Hannaford, and Richard M. Satava, editors, *Surgical Robotics: Systems Applications and Visions*, pages 199–217. Springer US, Boston, MA, 2011.

[2] Audrey Lee, Turner S Baker, Joshua B Bederson, and Benjamin I Rapoport. Levels of autonomy in FDA-cleared surgical robots: a systematic review. *npj Digital Medicine*, 2024.

[3] Pierre E. Dupont, Bradley J. Nelson, Michael Goldfarb, Blake Hannaford, Arianna Menciassi, Marcia K. O'Malley, Nabil Simaan, Pietro Valdastri, and Guang Zhong Yang. A decade retrospective of medical robotics research from 2010 to 2020. *Science Robotics*, 6(60), 2021.

[4] Elliot W. Hawkes, Laura H. Blumenschein, Joseph D. Greer, and Allison M. Okamura. A soft robot that navigates its environment through growth. *Science Robotics*, 2(8):1–8, 2017.

[5] Panagiotis Polygerinos, Nikolaus Correll, Stephen A. Morin, Bobak Mosadegh, Cagdas D. Onal, Kirstin Petersen, Matteo Cianchetti, Michael T. Tolley, and Robert F. Shepherd. Soft Robotics: Review of Fluid-Driven Intrinsically Soft Devices; Manufacturing, Sensing, Control, and Applications in Human-Robot Interaction, dec 2017.

[6] L. P. Jentoft, Y. Tenzer, D. Vogt, Jia Liu, R. J. Wood, and R. D. Howe. Flexible, stretchable tactile arrays from mems barometers. In *2013 16th International Conference on Advanced Robotics (ICAR)*, pages 1–6, Nov 2013.

[7] Mark Runciman, Ara Darzi, and George P. Mylonas. Soft Robotics in Minimally Invasive Surgery. *Soft Robotics*, 6(4):423–443, aug 2019.

[8] Laura H. Blumenschein, Allison M. Okamura, and Elliot W. Hawkes. Modeling of Bioinspired Apical Extension in a Soft Robot. In *Conference on Biomimetic and Biohybrid Systems*, pages 522–531, Stanford, CA, USA, 2017. Springer.

[9] Patrick Slade, Alex Gruebele, Zachary Hammond, Michael Raitor, Allison M. Okamura, and Elliot W Hawkes. Design of a Soft Catheter for Low-Force and Constrained Surgery. In Nihon Robotto Gakkai, editor, *IEEE/RSJ International Conference on Intelligent Robots and Systems*, pages 174–180, 2017.

[10] Nathaniel Agharese, Tyler Cloyd, Laura H Blumenschein, Michael Raitor, Elliot W Hawkes, Heather Culbertson, and Allison M Okamura. HapWRAP: Soft Growing Wearable Haptic Device. In *IEEE International Conference on Robotics and Automation (ICRA)*, Brisbane, QLD, Australia, 2018. IEEE.

[11] Laura H. Blumenschein, Nathan S. Usevitch, Brian H. Do, Elliot W. Hawkes, and Allison M. Okamura. Helical actuation on a soft inflated robot body. In *IEEE International Conference on Soft Robotics (RoboSoft)*, pages 245–252, Livorno, Italy, 2018. IEEE.

[12] Laura H Blumenschein, Lucia T Gan, Jonathan A Fan, Allison M Okamura, and Elliot W Hawkes. A Tip-Extending Soft Robot Enables Reconfigurable and Deployable Antennas. *IEEE Robotics and Automation Letters*, 3(2):949–956, 2018.

[13] Nicholas D Naclerio, Christian M Hubicki, Yasemin Ozkan Aydin, Daniel I Goldman, and Elliot W Hawkes. Soft Robotic Burrowing Device with Tip-Extension and Granular Fluidization. In *IEEE/RSJ International Conference on Intelligent Robots and Systems (IROS)*, 2018.

[14] A Sadeghi, A Tonazzini, L Popova, and B Mazzolai. Robotic Mechanism for Soil Penetration Inspired by Plant Root. In *IEEE International Conference on Robotics and Automation (ICRA)*, pages 3457–3462, Karlsruhe, Germany, 2013. IEEE.

[15] Ali Sadeghi, Alice Tonazzini, Liyana Popova, and Barbara Mazzolai. A novel growing device inspired by plant root soil penetration behaviors. *PLoS ONE*, 9(2), feb 2014.

[16] Emanuela Del Dottore, Alessio Mondini, ALi Sadeghi, Virgilio Mattoli, and Barbara Mazzolai. Circumnutations as a penetration strategy in a plant-root-inspired robot. In *2016 IEEE International Conference on Robotics and Automation (ICRA)*, pages 4722–4728, Stockholm, Sweden, 2016.

[17] Joseph D Greer, Laura H Blumenschein, Allison M Okamura, and Elliot W Hawkes. Obstacle-Aided Navigation of a Soft Growing Robot. In *IEEE International Conference on Robotics and Automation (ICRA)*, pages 4165–4172, Brisbane, QLD, Australia, 2018. IEEE.

[18] Joseph D. Greer, Tania K. Morimoto, Allison M. Okamura, and Elliot W. Hawkes. A Soft, Steerable Continuum Robot That Grows via Tip Extension. *Soft Robotics*, 6(1):95–108, 2019.

[19] Ryuma Niiyama, Xu Sun, Cynthia Sung, Byoungkwon An, Daniela Rus, and Sangbae Kim. Pouch motors: Printable soft actuators integrated with computational design. *Soft Robotics*, 2(2):59–70, jun 2015.

[20] Haitham El-Husseiny, Usman Mehmood, Zain Mehdi, Sang-Goo Jeong, Muhammad Usman, Elliot W. Hawkes, Allison M. Okamura, and Jee-Hwan Ryu. Development and Evaluation of an Intuitive Flexible Interface for Teleoperating Soft Growing Robots. In *IEEE/RSJ International Conference on Intelligent Robots and Systems (IROS)*, pages 4995–5002, Madrid, Spain, 2018. IEEE.

[21] P. Berthet-Rayne, K. Leibrandt, G. Gras, P. Fraisse, A. Crosnier, and G. Yang. Inverse kinematics control methods for redundant snakelike robot teleoperation during minimally invasive surgery. *IEEE Robotics and Automation Letters*, 3(3):2501–2508, July 2018.

[22] Margaret M. Coad, Laura H. Blumenschein, Sadie Cutler, Javier A. Reyna Zepeda, Nicholas D. Naclerio, Haitham El-Hussieny, Usman Mehmood, Jee-Hwan Ryu, Elliot W. Hawkes, and Allison M. Okamura. Vine Robots: Design, Teleoperation, and Deployment for Navigation and Exploration. *IEEE Robotics and Automation Magazine*, pages 1–9, 2019.

[23] Margaret M Coad, Rachel P Thomasson, Laura H Blumenschein, Nathan S Usevitch, Elliot W Hawkes, and Allison M Okamura. Retraction of Soft Growing Robots without Buckling. *Submitted*, 2019.

[24] Stephen B. Leighton and William H. Boyd. Everting Tube Device with Relative Advance Control, 1982.

[25] Benjamin B. Stanley and Katheen S. Collins. The toposcopic through-lumen everting catheter to facilitate dilation of severe strictures of the gastrointestinal tract. *Gastrointestinal Endoscopy*, 32(1):33–35, 1986.

[26] Steven R Bacich, Laguna Niguel, Keith Tholin, and Gary M Woker. METHOD OF DELIVERING A SUBSTANCE TO A FALLOPLAN TUBE, 1994.

[27] A. C. Pearlstone, E. S. Surrey, and J. F. Kerin. The linear everting catheter: A nonhysteroscopic, transvaginal technique for access and microendoscopy of the fallopian tube. *Fertility and Sterility*, 58(4):854–857, 1992.

[28] Kou Sueoka, Hironori Asada, Shinichi Tsuchiya, Noriko Kobayashi, Masako Kuroshima, and Yasunori Yoshimura. Falloposcopic tuboplasty for bilateral tubal oc-

clusion. A novel infertility treatment as an alternative for in-vitro fertilization? *Human Reproduction*, 13(1):71–74, 1998.

[29] Gautam N. Allahbadia and Rubina Merchant. Fallopian tube recanalization: Lessons learnt and future challenges. *Women's Health*, 6(4):531–549, 2010.

[30] Pierre Berthet-Rayne, S. M.Hadi Sadati, Georgios Petrou, Neel Patel, Stamatia Giannarou, Daniel Richard Leff, and Christos Bergeles. Mammobot: A miniature steerable soft growing robot for early breast cancer detection. *IEEE Robotics and Automation Letters*, 6(3):5056–5063, 2021.

[31] Árpád R. Takács, Dénes Nagy, Imre J. Rudas, and Tamás Haidegger. Origins of surgical robotics: From space to the operating room. *Acta Polytechnica Hungarica*, 13(1):13–30, 2016.

[32] Robert J III Webster, Noah J Cowan, Gregory Chirikjian, and Allison M Okamura. Nonholonomic Modeling of Needle Steering. *The International Journal of Robotics Research (IJRR)*, 25(5/6), 2006.

[33] Robert J. Webster and Bryan A. Jones. Design and kinematic modeling of constant curvature continuum robots: A review. *International Journal of Robotics Research*, 29(13):1661–1683, 2010.

[34] Jessica Burgner-Kahrs, D. Caleb Rucker, and Howie Choset. Continuum Robots for Medical Applications: A Survey. *IEEE Transactions on Robotics*, 31(6):1261–1280, dec 2015.

[35] D.I.K. Fielding, F. Bashirzadeh, J.H. Son, M. Todman, A. Chin, L. Tan, K. Steinke, M.N. Windsor, and A.W. Sung. First Human Use of a New Robotic-Assisted Fiber Optic Sensing Navigation System for Small Peripheral Pulmonary Nodules. *Respiration*, 98(2):142–150, 2019.

[36] Chauncey F Graetzel, Alexander Sheehy, and David P Noonan. Robotic bronchoscopy drive mode of the Auris Monarch platform. In *International Conference on Robotics and Automation (ICRA)*, pages 3895–3901, Montreal, Montreal, Canada, 2019. IEEE.

[37] Amir Degani, Howie Choset, Brett Zubiate, Takeyoshi Ota, and Marco Zenati. Highly Articulated Robotic Probe for Minimally Invasive Surgery. In *IEEE International Conference on Robotics and Automation (ICRA)*, Orlando, FL, USA, 2006. IEEE.

[38] Thomas Rösch, Andreas Adler, Heiko Pohl, Elke Wettschureck, Martin Koch, Bertram Wiedenmann, and Nicolas Hoepffner. A motor-driven single-use colonoscope controlled with a hand-held device: a feasibility study in volunteers. *Gastrointestinal Endoscopy*, 67(7):1139–1146, jun 2008.

[39] JS Engelsgjerd and CM Deibert. Cystoscopy, Jan 2020.

[40] Rebecca L Siegel, Kimberly D Miller, Hannah E Fuchs, and Ahmedin Jemal. Cancer Statistics, 2021. *CA: a cancer journal for clinicians*, 71(1):7–33, jan 2021.

[41] Matthew Mossanen and John L Gore. The burden of bladder cancer care: direct and indirect costs. *Current opinion in urology*, 24(5):487–491, sep 2014.

[42] Karim Chamie, Mark S. Litwin, Jeffrey C. Bassett, Tiimothy J. Daskivitch, Julie Lai, Jan M. Hanley, Badrinth R. Konety, Christopher S. Saigal, and The Urologic Diseases in America Project. RECURRENCE OF HIGH-RISK BLADDER CANCER: A POPULATION-BASED ANALYSIS. *Cancer*, 119(17):3219–3227, 2014.

[43] National Comprehensive Cancer Network. Bladder Cancer (Version 4.2021). url = https://www.nccn.org /professionals/physician_gls/pdf/bladder.pdf.

[44] Brent K Hollenbeck, Rodney L Dunn, Zaojun Ye, and John M Hollingsworth. Delays in Diagnosis and Bladder Cancer Mortality. *Cancer*, pages 5235–5242, 2010.

[45] American Urological Association. The State of the Urology Workforce and Practice in the United States. Technical report, American Urology Association, 2019.

[46] Eric M Pauli, Randy S Haluck, Barry Fell, and Jason Moore. Tubular Locomotion and Positioning Using Tip Eversion for Endoscopy. *Journal of Medical Devices*, 14(June):1–5, 2020.

[47] Anthony N. Kalloo, Vikesh K. Singh, Sanjay B. Jagannath, Hideaki Niiyama, Susan L. Hill, Cheryl A. Vaughn, Carolyn A. Magee, and Sergey V. Kantsevoy. Flexible transgastric peritoneoscopy: A novel approach to diagnostic and therapeutic interventions in the peritoneal cavity. *Gastrointestinal Endoscopy*, 60(1):114–117, jul 2004.

[48] Jaques Marescaux and Francesco Rubino. Transcontinental robot-assisted remote telesurgery, feasibility and potential applications. *Annals of Surgery*, 235(4):487–492, 2006.

[49] Lonny Yarmus, Jason Akulian, Momen Wahidi, Alex Chen, Jennifer P Steltz, Sam L Solomon, Diana Yu, Fabien Maldonado, Jose Cardenas-Garcia, Daniela Molena, et al. A prospective randomized comparative study of three guided bronchoscopic approaches for investigating pulmonary nodules: the precision-1 study. *Chest*, 157(3):694–701, 2020.

[50] Nima Sarli, Giuseppe Del Giudice, Smita De, Mary S. DIetrich, Stanley Duke Herrell, and Nabil Simaan. Preliminary Porcine in Vivo Evaluation of a Telerobotic System for Transurethral Bladder Tumor Resection and Surveillance. *Journal of Endourology*, 32(6):516–522, 2018.

[51] Nima Sarli, Giuseppe Del Giudice, Smita De, Mary S. Dietrich, S. Duke Herrell, and Nabil Simaan. TURBot: A system for robot-assisted transurethral bladder tumor resection. *IEEE/ASME Transactions on Mechatronics*, 24(4):1452–1463, 2020.

[52] Richard J Hendrick, Christopher R Mitchell, S Duke Herrell, and Robert J Webster Iii. Hand-held transendoscopic robotic manipulators: A transurethral laser prostate surgery case study. *The International Journal of Robotics Research*, 34(13):1559–1572, 2015.

[53] Anton Wong, YC Phan, Helen Thursby, and Wasim Mahmalji. The First UK Experience with Single-use Disposable Flexible Cystoscopes: An In-depth Cost Analysis, Service Delivery and Patient Satisfaction Rate with Ambu® aScope™ 4 Cysto. *Journal of Endoluminal Endourology*, 4(1):e29–e44, apr 2021.

[54] Jonathan N Rubenstein, Maurice Garcia, Affonso H L A Camargo, Andrew B Joel, and Marshall L Stoller. Novel Everting Urologic Access Sheath : Decreased Axial Forces during Insertion. *J Endourol.*, 19(10):1216–1220, 2005.

[55] Jamie Luong, Paul Glick, Aaron Ong, Maya S. DeVries, Stuart Sandin, Elliot W. Hawkes, and Michael T. Tolley. Eversion and retraction of a soft robot towards the exploration of coral reefs. *RoboSoft 2019 - 2019 IEEE International Conference on Soft Robotics*, pages 801–807, 2019.

[56] Margaret M. Coad, Laura H. Blumenschein, Sadie Cutler, Javier A. Reyna Zepeda, Nicholas D. Naclerio, Haitham El-Hussieny, Usman Mehmood, Jee-Hwan Ryu, Elliot W. Hawkes, and Allison M. Okamura. Vine robots. *IEEE Robotics & Automation Magazine*, 27(3):120–132, 2020.

[57] Joel Hwee, Andrew Lewis, Randall A. Bly, Kris S. Moe, and Blake Hannaford. An everting emergency airway device. In *2021 International Symposium on Medical Robotics (ISMR)*, pages 1–7, 2021.

[58] Grace O'Connor, Andrew **Lewis**, Alex Gong, Daniel Burke, and Blake Hannaford. Manufacturing and design improvements of an everting airway device prototype. In *2024 International Symposium on Medical Robotics (ISMR)*, pages 1–7, 2024.

[59] Barbara Mazzolai, Nabil Derbel, Mattia Gazzola, Laura H Blumenschein, Margaret M Coad, David A Haggerty, Allison M Okamura, and Elliot W Hawkes. Design, Modeling, Control, and Application of Everting Vine Robots. *Frontiers in Robotics and AI — www.frontiersin.org*, 1:548266, 2020.

[60] Allison Raines, Andrew Lewis, Joel Hwee, and Blake Hannaford. Inferring environmental interactions of soft everting robots from acoustic signals. In *2023 IEEE International Conference on Soft Robotics (RoboSoft)*, pages 1–6, 2023.

[61] Hideyuki Tsukagoshi, Nobuyuki Arai, Ichiro Kiryu, and Ato Kitagawa. Smooth Creeping Actuator by Tip Growth Movement Aiming for Search and Rescue Operation. In *IEEE International Conference on Robotics and Automation (ICRA)*, Shanghai, China, 2011. IEEE.

[62] Elliot W. Hawkes, Laura H. Blumenschein, Joseph D. Greer, and Allison M. Okamura. Supplementary Materials - A soft robot that navigates its environment through growth. *Science Robotics*, 2(8), jul 2017.

[63] Carmen Larrea, Pierre Berthet-Rayne, S. M.Hadi Sadati, Daniel Richard Leff, Christos Bergeles, and Ioannis Georgilas. Growing Robotic Endoscope for Early Breast Cancer Detection: Robot Motion Control. *Towards Autonomous Robotic Systems Conference (TAROS) Citing*, 13054 LNAI:391–401, 2021.

[64] Cédric Girerd, Anna Alvarez, Elliot W Hawkes, and Tania K Morimoto. Material Scrunching Enables Working Channels in Miniaturized Vine-Inspired Robots. *IEEE TRANSACTIONS ON ROBOTICS*, 40:2024, 2024.

[65] David A. Haggerty, Nicholas D. Naclerio, and Elliot W. Hawkes. Characterizing environmental interactions for soft growing robots. In *2019 IEEE/RSJ International Conference on Intelligent Robots and Systems (IROS)*, pages 3335–3342, 2019.

[66] Joel Hwee, Andrew Lewis, Allison Raines, and Blake Hannaford. Kinematic modeling of a soft everting robot from inflated beam theory. In *2023 IEEE International Conference on Soft Robotics (RoboSoft)*, pages 1–6, 2023.

[67] Joseph D Greer, Laura H Blumenschein, Ron Alterovitz, Elliot W Hawkes, and Allison M Okamura. Robust navigation of a soft growing robot by exploiting contact with the environment. *The International Journal of Robotics Research*, 39(14):1724–1738, 2020.

[68] Margaret M. Coad, Rachel P. Thomasson, Laura H. Blumenschein, Nathan S. Usevitch, Elliot W. Hawkes, and Allison M. Okamura. Retraction of soft growing robots without buckling. *IEEE Robotics and Automation Letters*, 5(2):2115–2122, 2020.

[69] Panagiotis Vartholomeos, Zicong Wu, Hadi Sadati, and Christos Bergeles. Lumped parameter dynamic model of an eversion growing robot: Analysis, simulation and experimental validation. In *IEEE International Conference on Robotics and Automation (ICRA)*, 2024.

[70] Ji Hun Kim, Jaehyung Jang, Sang Min Lee, Sang Goo Jeong, Yong Jae Kim, and Jee Hwan Ryu. Origami-inspired New Material Feeding Mechanism for Soft Growing Robots to Keep the Camera Stay at the Tip by Securing its Path. *IEEE Robotics and Automation Letters*, 6(3):4592–4599, jul 2021.

[71] James A Lockhart. An Analysis of Irreversible Plant Cell Elongation. *J. Theoret. Biology*, 8(2):264–275, 1965.

[72] P. B. Green, R. O. Erickson, and J. Buggy. Metabolic and Physical Control of Cell Elongation Rate. *Plant Physiology*, 47(3):423–430, 1971.

[73] H. Olsson, K. J. Åström, C. Canudas De Wit, M. Gäfvert, and P. Lischinsky. Friction Models and Friction Compensation. *European Journal of Control*, 4(3):176–195, jan 1998.

[74] Connie W. Tsao, Aaron W. Aday, Zaid I. Almarzooq, Cheryl A.M. Anderson, Pankaj Arora, Christy L. Avery, Carissa M. Baker-Smith, Andrea Z. Beaton, Amelia K. Boehme, Alfred E. Buxton, Yvonne Commodore-Mensah, Mitchell S.V. Elkind, Kelly R. Evenson, Chete Eze-Nliam, Setri Fugar, Giuliano Generoso, Debra G. Heard, Swapnil Hiremath, Jennifer E. Ho, Rizwan Kalani, Dhruv S. Kazi, Darae Ko, Deborah A. Levine, Junxiu Liu, Jun Ma, Jared W. Magnani, Erin D. Michos, Michael E. Mussolino, Sankar D. Navaneethan, Nisha I. Parikh, Remy Poudel, Mary Rezk-Hanna, Gregory A. Roth, Nilay S. Shah, Marie-Pierre St-Onge, Evan L. Thacker, Salim S. Virani, Jenifer H. Voeks, Nae-Yuh Wang, Nathan D. Wong, Sally S. Wong, Kristine Yaffe, and Seth S. Martin. Heart disease and stroke statistics—2023 update: A report from the american heart association. *Circulation*, 147(8):e93–e621, 2023.

[75] Joel Hwee. *Modeling and Applications of Everting Vine Robots*. Ms thesis, University of Washington, Seattle, WA, June 2021. Available at `https://digital.lib.washington.edu/researchworks/handle/1773/47649`.

[76] Megan B. Blackburn, Michael D. April, Derek J. Brown, Robert A. DeLorenzo, Kathy L. Ryan, August N. Blackburn, and Steven G. Schauer. Prehospital airway procedures performed in trauma patients by ground forces in Afghanistan. *The journal of trauma and acute care surgery*, 85(1S Suppl 2):S154–S160, 2018.

[77] University of washington paramedic training program curriculum. https://www.uwpmt.org/public/program-curriculum. Accessed: November 14, 2023.

[78] Abdelfattah A. Touman and Grigoris K. Stratakos. Long-Term Complications of Tracheal Intubation. *Tracheal Intubation*, 2018.

[79] M. Chandler. Tracheal intubation and sore throat: A mechanical explanation. *Anaesthesia*, 57(2):155–161, 2002.

[80] David M Gnugnoli, Abhishek Singh, and Katherine Shafer. *EMS Field Intubation*. StatPearls Publishing, 2023.

[81] Pavel Michalek, William Donaldson, Eliska Vobrubova, and Marek Hakl. Complications associated with the use of supraglottic airway devices in perioperative medicine. *BioMed Research International*, 2015, 2015.

[82] T. M. Hemmerling, R. Taddei, M. Wehbe, C. Zaouter, S. Cyr, and J. Morse. First robotic tracheal intubations in humans using the Kepler intubation system. *British Journal of Anaesthesia*, 2012.

[83] Hongbo Wang, Massimo Totaro, and Lucia Beccai. Toward Perceptive Soft Robots: Progress and Challenges, sep 2018.

[84] P. Biro, P. Hofmann, D. Gage, Q. Boehler, C. Chautems, J. Braun, D. R. Spahn, and B. J. Nelson. Automated tracheal intubation in an airway manikin using a robotic endoscope: a proof of concept study. *Anaesthesia*, page anae.14945, jan 2020.

[85] Mingyuan Li, Rosario Obregon, Jeremy J. Heit, Alexander Norbash, Elliot W. Hawkes, and Tania K. Morimoto. Vine catheter for endovascular surgery. *IEEE Transactions on Medical Robotics and Bionics*, 3(2):384–391, 2021.

[86] Joseph D. Greer, Tania K. Morimoto, Allison M. Okamura, and Elliot W. Hawkes. Series pneumatic artificial muscles (spams) and application to a soft continuum robot. In *2017 IEEE International Conference on Robotics and Automation (ICRA)*, pages 5503–5510, 2017.

[87] Nicholas D. Naclerio and Elliot W. Hawkes. Simple, low-hysteresis, foldable, fabric pneumatic artificial muscle. *IEEE Robotics and Automation Letters*, 5(2):3406–3413, 2020.

[88] Alexander M. Kübler, Cosima du Pasquier, Andrew Low, Betim Djambazi, Nicolas Aymon, Julian Förster, Nathaniel Agharese, Roland Siegwart, and Allison M. Okamura. A comparison of pneumatic actuators for soft growing vine robots, 2023.

[89] Jeongmin Ock, Eunhye Gwon, Daeyoung Kim, Sangbin Kim, and Namkug Kim. Patient-specific and hyper-realistic phantom for an intubation simulator with a replaceable difficult airway of a toddler using 3D printing. *Sci Rep*, 10(1):1, 2020.

[90] Hartmut Ocker, Volker Wenzel, Peter Schmucker, and Volker Dörges. Effectiveness of various airway management techniques in a bench model simulating a cardiac arrest patient. *Journal of Emergency Medicine*, 20(1):7–12, 2001.

[91] Mohamed Turki, Michael P Young, Scott S Wagers, and Jason HT Bates. Peak pressures during manual ventilation. *Respiratory Care*, 50(3):340–344, 2005.

[92] Joseph Brimacombe, Christian Keller, and Fritz Pühringer. Pharyngeal Mucosal Pressure and Perfusion . *Anesthesiology*, 91(6):1661–1661, 1999.

[93] Andrew B Lumb and Caroline R Thomas. *Nunn's Applied Respiratory Physiology eBook: Nunn's Applied Respiratory Physiology eBook*. Elsevier Health Sciences, 2020.

[94] Mitsuhiro Kano, Yoshinaka Shimizu, Keisuke Okayama, Toshirou Igari, and Masayoshi Kikuchi. A morphometric study of age-related changes in adult human epiglottis using quantitative digital analysis of cartilage calcification. *Cells Tissues Organs*, 180(2):126–137, 2005.

[95] Christian Keller and Joseph Brimacombe. Pharyngeal Mucosal Pressures, Airway Sealing Pressures, and Fiberoptic Position with the Intubating versus the Standard Laryngeal Mask Airway. *Anesthesiology*, 90(4):1001–1006, apr 1999.

[96] Bernd E. Winkler, Ralf M. Muellenbach, Thomas Wurmb, Manuel F. Struck, Norbert Roewer, and Peter Kranke. Passive continuous positive airway pressure ventilation dur-

ing cardiopulmonary resuscitation: a randomized cross-over manikin simulation study. *Journal of Clinical Monitoring and Computing*, 31(1):93–101, 2017.

[97] Kayvon Modjarrad and Sina Ebnesajjad. *Handbook of Polymer Applications in Medicine and Medical Devices*. William Andrew, 2014.

[98] Medical device solutions - Lubrizol. `https://www.lubrizol.com/-/media/Lubrizol/Health/Literature/Medical-Device-TPU-Product-Guide.pdf`. Accessed: November 14, 2023.

[99] E. B. Liem. Combitube intubation. `http://vam.anest.ufl.edu/airwaydevice/combitube/index.html`, 2006. Accessed: November 14, 2023 from University of Florida Department of Anesthesiology, Center for Simulation, Advanced Learning and Technology, Virtual Anesthesia Machine Web Site.

[100] David Hananel, Daniel Silverglate, Daniel Burke, Ben Riggs, Jack Norfleet, and Robert M. Sweet. The advanced modular manikin open source platform for healthcare simulation. *Military Medicine*, 186(Supplement_1):49–57, 2021.

[101] Thane Hunt. Easy cnc heat sealer, 2022. `https://hackaday.io/project/183836-easy-cnc-heat-sealer/details`, Accessed: June 2, 2024.

[102] Amir Ali Amiri Moghadam, Seyedhamidreza Alaie, Suborna Deb Nath, Mahdie Aghasizade Shaarbaf, James K Min, Simon Dunham, and Bobak Mosadegh. Laser cutting as a rapid method for fabricating thin soft pneumatic actuators and robots. *Soft Robot.*, 5(4):443–451, August 2018.

[103] Brandon Saldarriaga Fajardo, Carlo Seneci, Hadi Sadati, Zicong Wu, Kawal Rhode, and Christos Bergeles. Co2 laser welding of low-density polyethylene for soft linear eversion robot fabrication. In *IEEE 20th International Conference on Automation Science and Engineering (CASE)*, 2024.

[104] M Carassiti, R Zanzonico, S Cecchini, S Silvestri, R Cataldo, and FE Agrò. Force and pressure distribution using macintosh and glidescope laryngoscopes in normal and difficult airways: a manikin study. *British journal of anaesthesia*, 108(1):146–151, 2012.

[105] Andrew Lewis, Joel Hwee, Grace O'Connor, Alex Gong, Daniel M. Burke, Randall A. Bly, Kris S. Moe, Waleed M. Abuzeid, Eric Seibel, and Blake Hannaford. Design evolution of an emergancy airway device. *Journal of Medical Robotics Research*, 2024. Under Review.

[106] Andrew Lewis, Eric Seibel, and Blake Hannaford. Using friction to improve growth estimation of reel-mounted everting robots. *In Preparation*, 2024.

[107] Andrew Lewis and Blake Hannaford. Characterizing an everting tube's working channel friction. *In Preparation*, 2024.

[108] Pengcheng Chen, Nicole M Gunderson, Andrew Lewis, Jason R Speich, Michael P Porter, and Eric J Seibel. Enabling rapid and high-quality 3d scene reconstruction in cystoscopy through neural radiance fields. In *Medical Imaging 2024: Image-Guided Procedures, Robotic Interventions, and Modeling*, volume 12928, pages 350–359. SPIE, 2024.

[109] Allison Raines, Andrew Lewis, Joel Hwee, and Blake Hannaford. Inferring environmental interactions of soft everting robots from acoustic signals. In *2023 IEEE International Conference on Soft Robotics (RoboSoft)*, pages 1–6. IEEE, 2023.

[110] Chen Gong, Yaxuan Zhou, Andrew Lewis, Pengcheng Chen, Jason R Speich, Michael P Porter, Blake Hannaford, and Eric J Seibel. Real-time camera localization during robot-assisted telecystoscopy for bladder cancer surveillance. *Journal of Medical Robotics Research*, 2022.

[111] Pengcheng Chen, Chen Gong, Andrew **Lewis**, Yaxuan Zhou, Seyed Mohammad, Mohaghegh Poor, Blake Hannaford, and Eric J Seibel. Real-time flexible endoscope nav-

igation within bladder phantom having sparse non-distinct features is enhanced with robotic control. In *SPIE Medical Imaging*, page [**Best Student Paper Finalist**], San Diego, CA, USA, 2022. SPIE.

[112] Andrew **Lewis***, Chen Gong*, Yaxuan Zhou, Pengcheng Chen, Michael P Porter, Blake Hannaford, and Eric J Seibel. Real Time Localization of Cystoscope Angulation in 2D Bladder Phantom for Telecystoscopy. In *International Symposium on Medical Robotics (ISMR)*, page [**Best Paper award**], Atlanta, GA, USA, 2021. IEEE.

[113] Joel Hwee, Andrew **Lewis**, Allison Raines, and Blake Hannaford. Kinematic modeling of a soft everting robot from inflated beam theory. In *2023 IEEE International Conference on Soft Robotics (RoboSoft)*, pages 1–6. IEEE, 2023.

[114] Joel Hwee, Andrew **Lewis**, Randall A Bly, Kris S Moe, and Blake Hannaford. An Everting Emergency Airway Device. In *International Symposium on Medical Robotics*, Atlanta, GA, USA, 2021. IEEE.

[115] Muneaki Miyasaka, Mohammad Haghighipanah, Yangming Li, Joseph Matheson, Andrew **Lewis**, and Blake Hannaford. Modeling Cable-Driven Robot With Hysteresis and Cable – Pulley Network Friction. *IEEE/ASME Transactions on Mechatronics*, 25(2):1095–1104, 2020.

[116] Yun-hsuan Su, Adnan Munawar, Anton Deguet, Andrew **Lewis**, Kyle Lindgren, Yangming Li, Russell H Taylor, Gregory S Fischer, Blake Hannaford, Peter Kazanzides, and A Background. Collaborative Robotics Toolkit (CRTK): Open Software Framework for Surgical Robotics Research. In *IEEE International Conference on Robotic Computing (IRC)*, pages 48–55, Taichung, Taiwan, 2020.

[117] Andrew **Lewis**, David Drajeske, John Raiti, Angelique Berens, Jacob Rosen, and Blake Hannaford. RAVEN-S: Design and Simulation of a Robot for Teleoperated Micro-

gravity Rodent Dissection under Time Delay. In *Proceedings - IEEE International Conference on Robotics and Automation*, pages 11332–11337, 2020.

[118] Yangming Li, Shuai Li, David Caballero, Muneaki Miyasaka, Andrew **Lewis**, and Blake Hannaford. Improving control precision and motion adaptiveness for surgical robot with recurrent neural network. In *IEEE International Conference on Intelligent Robots and Systems*, volume 2017-Septe, pages 3538–3543, Vancouver, BC, Canada, 2017. IEEE.

[119] Muneaki Miyasaka, Joseph Matheson, Andrew **Lewis**, and Blake Hannaford. Measurement of the Cable-Pulley Coulomb and Viscous Friction for a Cable-Driven Surgical Robotic System. *2015 IEEE/RSJ International Conference on Intelligent Robots and Systems (IROS)*, pages 804–810, 2015.

[120] Homa Alemzadeh, Daniel Chen, Andrew **Lewis**, Zbigniew Kalbarczyk, and Ravishankar Iyer. Systems-Theoretic Safety Assessment of Robotic Telesurgical Systems Systems-theoretic Safety Assessment of Robotic Telesurgical Systems. In *SAFECOMP*, 2015.

[121] Deanna Glassman, Lee White, Andrew **Lewis**, Hawkeye King, Alicia Clarke, Thomas Glassman, Bryan Comstock, Blake Hannaford, and Thomas S Lendvay. Raven surgical robot training in preparation for da vinci. *Studies in health technology and informatics*, 196:135–41, 2014.

[122] Andrew **Lewis** and Blake Hannaford. Dynamically evaluated gravity compensation for the RAVEN surgical robot. In *2014 IEEE International Conference on Robotics and Automation (ICRA)*, pages 2534–2539. IEEE, may 2014.

[123] Daniel Jones, Andrew **Lewis**, and Gregory S. Fischer. Development of a standalone surgical haptic arm. *Proceedings of the Annual International Conference of the IEEE Engineering in Medicine and Biology Society, EMBS*, pages 2136–2139, 2011.

[124] Brandon Ingram, Daniel Jones, Andrew **Lewis**, Matthew Richards, Charles Rich, and Lance Schachterle. A Code of Ethics For Robotics Engineers. In *ACM/IEEE international conference on Human-robot interaction*, pages 103–104. ACM, 2010.

Appendix A

PRESSURE CONTROL CIRCUIT AND SOFTWARE

A.1 Pressure Control Circuit

In order to provide current-controlled input to the high side control input of the digital pressure controller of Chapter 3, an NPN transistor was used to switch an external voltage supply based on the PWM output of the Arduino. A PNP transistor was added in order use a higher driving voltage for pressure control current. The schematic can be seen in Figure A.1, the component values in Table A.1 and the circuit as built in Figure A.2.

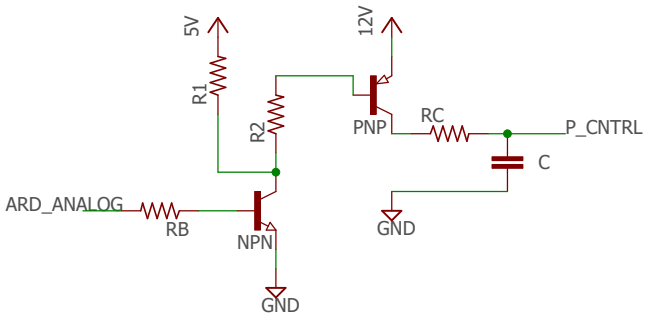

Figure A.1: Schematic for arduino-based current control of variable pressure regulator.

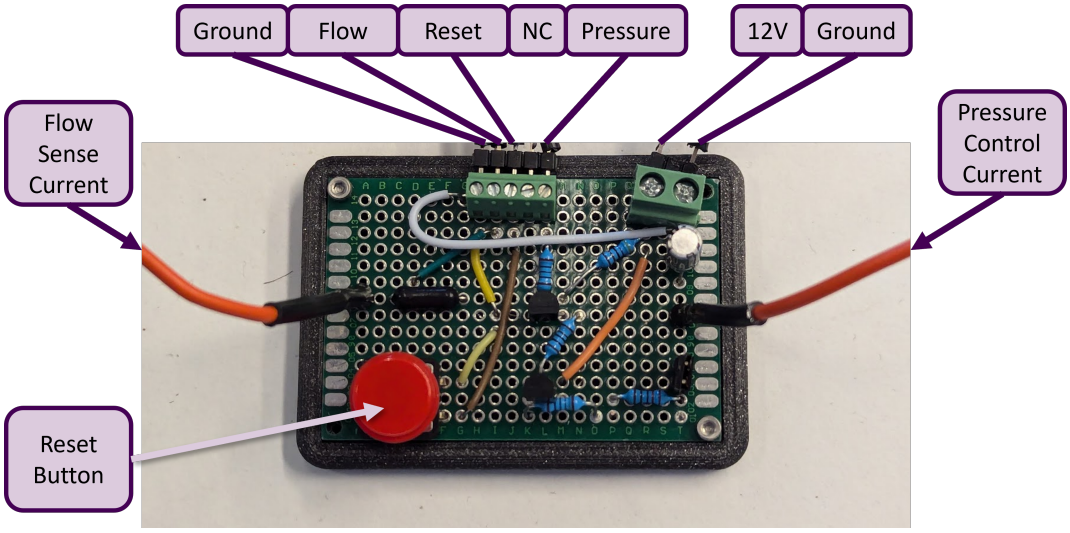

Figure A.2: Protoboard layout for current-controlled pressure regulator, digital reset button, and flow sensor interface.

Table A.1: Component Values for Pressure Control Circuit

R_B	100 Ω
R_1	4.7k Ω
R_2	1k Ω
R_C	330 Ω
C	47-100 μF

A.2 Pressure Increment Code

```
/*
   Program to step through pressure settings and send serial data over USB
    for storage.

   Encoder code derived from:
   https://github.com/davidjabon/LS7366


   Pressure code derived from:
```

```
9       Basic test of the Qwiic MicroPressure Sensor
    By: Alex Wende
11    SparkFun Electronics
    Date: July 2020
13 */
#include <LS7366.h>
15 #include <SPI.h>
#include <Wire.h>
17 #include <SparkFun_MicroPressure.h>

19 #define LED_PIN           7
#define FLOW_SENSE        A0
21 #define BUTTON_1          5
#define BUTTON_RESET      8
23 #define PRESSURE_CTRL     6
#define MIN_P_CNTRL       21  // 51 = 1V --> 4mA at 250 Ohm
25 #define MAX_P_CNTRL       235 // 51 = 1V --> 4mA at 250 Ohm
#define P_STEP            10
27 // #define PRESSURE_CHARACTERIZE

29 #define STEP_TIME         10000000

31 LS7366 myLS7366(10);  //10 is the Uno chip select pin.

33 char sync_button_pin = 5;

35 /*
    Initialize Constructor
37    Optional parameters:
     - EOC_PIN: End Of Conversion (defualt: -1)
39     - RST_PIN: Reset (defualt: -1)
     - MIN_PSI: Minimum Pressure (default: 0 PSI)
41     - MAX_PSI: Maximum Pressure (default: 25 PSI)
```

```
*/
//SparkFun_MicroPressure mpr(EOC_PIN, RST_PIN, MIN_PSI, MAX_PSI);
SparkFun_MicroPressure mpr; // Use default values with reset and EOC pins
    unused

unsigned long time_start;
char pressure_connected = 1;

int incomingByte = 0;

void setup() {
  pinMode(LED_PIN, OUTPUT);
  pinMode(FLOW_SENSE, INPUT);
  pinMode(BUTTON_1, INPUT);
  pinMode(BUTTON_RESET, INPUT_PULLUP);
  Wire.begin();
  Serial.begin(115200);

  myLS7366.write_mode_register_0(FILTER_1 | DISABLE_INDX | FREE_RUN |
   QUADRX4);
  myLS7366.write_mode_register_1(NO_FLAGS | EN_CNTR | BYTE_4 );
  myLS7366.clear_counter();
  myLS7366.clear_status_register();
  myLS7366.write_data_register(4);

    /* The micropressure sensor uses default settings with the address 0
   x18 using Wire.
    The mircropressure sensor has a fixed I2C address, if another address
   is used it
    can be defined here. If you need to use two micropressure sensors, and
    your
    microcontroller has multiple I2C buses, these parameters can be
   changed here.
```

```
69      E.g. mpr.begin(ADDRESS, Wire1)
        Will return true on success or false on failure to communicate. */
71    if (!mpr.begin())
      {
73      Serial.println("Cannot connect to MicroPressure sensor.");
        pressure_connected = 0;
75      //while(1);
      }
77
//    delay(1);
79    time_start = micros();

81  }

83  long reelEncPos  = -999;

85  void loop() {
      static signed long newReelEncPos;
87    static char sync = 0;
      static double pressure = 0;
89    static char sendMsg = 0;
      static char newData = 0;
91    static char streamData = 0;
      static char streamBatch = 0;
93    static double batchLabel = 0;
      static int batchCount = 0;
95    static unsigned long readTime;
      static int sync_button = 0;
97    static int sync_button_last = 0;
      static int reset_button = 0;
99    static int reset_button_last = 0;
      static unsigned long last_msg_time  = micros();
101   static char sync_state = 0;
```

```
103  static int p_cntrl_read;
     static int p_cntrl_set = MIN_P_CNTRL;
105
     static int flow_val;
107
     unsigned long time_now = micros();
109
     static unsigned long last_step_time = time_now;
111

113  //read sensor data at a reasonable rate
     if (micros() - last_msg_time > 20000 - 10600) { //2500 should be 400 Hz
115                                                  //22700 should be 44 Hz

117
       // get sensor time stamp
119    readTime = micros();
       newReelEncPos = myLS7366.read_counter();
121    if (pressure_connected == 1) {
         pressure = mpr.readPressure();
123    }

125    reelEncPos = newReelEncPos;
       sync_button = digitalRead(sync_button_pin);
127    reset_button = !digitalRead(BUTTON_RESET); // wired with opposite
      logic

129    flow_val = analogRead(FLOW_SENSE);

131    if (p_cntrl_set < MIN_P_CNTRL)
       p_cntrl_set = MIN_P_CNTRL;
133
```

```
    // increment pressure setting if signaled
135 if (sync_button == 1 && sync_button_last == 0){
      p_cntrl_set += P_STEP;
137   if (p_cntrl_set > MAX_P_CNTRL)
        p_cntrl_set = MAX_P_CNTRL;
139   if (p_cntrl_set < MIN_P_CNTRL)
        p_cntrl_set = MIN_P_CNTRL;
141 }

143 // reset pressure setting if signaled
    if (reset_button == 1 && reset_button_last == 0){
145     p_cntrl_set = MIN_P_CNTRL;
    }
147
    analogWrite(PRESSURE_CTRL, p_cntrl_set);
149 sync_button_last = sync_button;
    reset_button_last = reset_button;
151
    newData = 1;
153 }

155 // option to step through pressure settings based on time
#ifdef PRESSURE_CHARACTERIZE
157 if (micros() - last_step_time > STEP_TIME){
      p_cntrl_set += 10;
159   if (p_cntrl_set > MAX_P_CNTRL)
        p_cntrl_set = MIN_P_CNTRL;
161   if (p_cntrl_set < MIN_P_CNTRL)
        p_cntrl_set = MIN_P_CNTRL;
163
      last_step_time = micros();
165 }
#endif
```

```
167
169   // check the serial connection for requests
      if (micros() - last_msg_time > 100) {
171     if (Serial.available() > 0) {
          // read the incoming byte:
173       incomingByte = Serial.read();
          if (incomingByte == '!') sync = 1;
175       if (incomingByte == 'r') sendMsg = 1;
          if (incomingByte == 's') streamData = !streamData;
177       if (incomingByte == 'b') streamBatch = 1;
          if (incomingByte == 'p') p_cntrl_set = MIN_P_CNTRL;
179     }
      }
181
      if (streamData == 1) sendMsg = 1;
183
      if(sync){
185     sync_state = !sync_state;
        digitalWrite(LED_PIN, sync_state);
187   }

189   int batchLimit = 250;
      if (streamBatch == 1){
191     sendMsg = 1;
      }
193   if (batchCount > batchLimit){
        batchCount = 0;
195     streamBatch = 0;
        batchLabel = 0;
197   }

199   if (sendMsg && newData) {
```

```
    last_msg_time = micros();
201     Serial.print(time_now); // time
    Serial.print(" , ");
203     Serial.print(newReelEncPos);  // reel encoder
    Serial.print(" , ");
205     Serial.print(p_cntrl_set);        // pressure controller setting
    Serial.print(" , ");
207     Serial.print(flow_val);        // flow analog
    Serial.print(" , ");
209     Serial.print(pressure, 4);       // pressure
    Serial.print(" , ");
211     Serial.print(int(sync_state));     // synchronization serial return
   from laptop
    Serial.print(" , ");
213     Serial.print(sync_button);     // go button
    Serial.print(" , ");
215     Serial.println(reset_button);     // reset button

217     if(streamBatch) batchCount++;;

219     sendMsg = 0;
    newData = 0;
221     sync = 0;
  }
223
  sync = 0;
225 }
```

Listing A.1: PressureIncrement.ino

A.3 Autonomous Eversion State Machine Code

```
2 /*
```

```
   Program to automatically step through pressure settings and send serial
    data over USB for storage for Chapter 3 experiments.

   Encoder code derived from:
   https://github.com/davidjabon/LS7366

   Pressure code derived from:
     Basic test of the Qwiic MicroPressure Sensor
   By: Alex Wende
   SparkFun Electronics
   Date: July 2020
*/
#include <LS7366.h>
#include <SPI.h>
#include <Wire.h>
#include <SparkFun_MicroPressure.h>



#define LED_PIN           7
#define FLOW_SENSE        A0
#define BUTTON_1          5
#define BUTTON_RESET      8
#define PRESSURE_CTRL     6
#define MIN_P_CNTRL       21   // 115    // 51 = 1V --> 4mA at 250 Ohm
#define MAX_P_CNTRL       235 // 115    // 51 = 1V --> 4mA at 250 Ohm
#define P_STEP            20

#define STEP_TIME           10000000 / 2
#define MOVEMENT_THRESH      200        // minimum encoder steps for
   determining movement 200 ~~ 1/8"


```

```
34 LS7366 myLS7366(10);  //10 is the Uno chip select pin.

36 char sync_button_pin = 5;

38

/*
40    Initialize Constructor
    Optional parameters:
42     - EOC_PIN: End Of Conversion (defualt: -1)
     - RST_PIN: Reset (defualt: -1)
44     - MIN_PSI: Minimum Pressure (default: 0 PSI)
     - MAX_PSI: Maximum Pressure (default: 25 PSI)
46 */
//SparkFun_MicroPressure mpr(EOC_PIN, RST_PIN, MIN_PSI, MAX_PSI);
48 SparkFun_MicroPressure mpr; // Use default values with reset and EOC pins
    unused

50

unsigned long time_start;
52 char pressure_connected = 1;

54 int incomingByte = 0;

56 void setup() {
  pinMode(LED_PIN, OUTPUT);
58   pinMode(FLOW_SENSE, INPUT);
  pinMode(BUTTON_1, INPUT);
60   pinMode(BUTTON_RESET, INPUT_PULLUP);
  Wire.begin();
62   Serial.begin(115200);

64
```

```
  myLS7366.write_mode_register_0(FILTER_1 | DISABLE_INDX | FREE_RUN |
   QUADRX4);
  myLS7366.write_mode_register_1(NO_FLAGS | EN_CNTR | BYTE_4 );
  myLS7366.clear_counter();
  myLS7366.clear_status_register();
  myLS7366.write_data_register(4);

    /* The micropressure sensor uses default settings with the address 0
   x18 using Wire.
    The mircropressure sensor has a fixed I2C address, if another address
   is used it
    can be defined here. If you need to use two micropressure sensors, and
    your
    microcontroller has multiple I2C buses, these parameters can be
   changed here.
    E.g. mpr.begin(ADDRESS, Wire1)
    Will return true on success or false on failure to communicate. */
  if (!mpr.begin())
  {
    Serial.println("Cannot connect to MicroPressure sensor.");
    pressure_connected = 0;
    //while(1);
  }

//  delay(1);
  time_start = micros();

}


long reelEncPos  = -999;


```

```
void loop() {
  static signed long newReelEncPos;
  static char sync = 0;
  static double pressure = 0;
  static char sendMsg = 0;
  static char newData = 0;
  static char streamData = 0;
  static char streamBatch = 0;
  static double batchLabel = 0;
  static int batchCount = 0;
  static unsigned long readTime;
  static int sync_button = 0;
  static int sync_button_last = 0;
  static int reset_button = 0;
  static int reset_button_last = 0;
  static unsigned long last_msg_time  = micros();
  static char sync_state = 0;

  static int p_cntrl_read;
  static int p_cntrl_set = MIN_P_CNTRL;

  static int flow_val;

  static int initial_growth = 0;
  static int grown = 0;
  static int auto_step = 0;
  static int waiting = 1;
  static int moved = 0;

  static long step_start_encoder = 0;
  static int previous_phase_pressure = MIN_P_CNTRL;

  unsigned long time_now = micros();
```

```
126
    static unsigned long last_step_time = time_now;
128

130 //read sensor data
    if (micros() - last_msg_time > 20000 - 10600) { //2500 should be 400 Hz
132                                                 //22700 should be 44 Hz

134   // get sensor time stamp
      readTime = micros();
136   newReelEncPos = myLS7366.read_counter();
      if (pressure_connected == 1) {
138     pressure = mpr.readPressure();
      }
140
      reelEncPos = newReelEncPos;
142   sync_button = digitalRead(sync_button_pin);
      reset_button = !digitalRead(BUTTON_RESET); // wired with opposite
     logic
144
      flow_val = analogRead(FLOW_SENSE);
146
      if (p_cntrl_set < MIN_P_CNTRL)
148     p_cntrl_set = MIN_P_CNTRL;
      if (p_cntrl_set > MAX_P_CNTRL)
150     p_cntrl_set = MAX_P_CNTRL;

152   analogWrite(PRESSURE_CTRL, p_cntrl_set);
      sync_button_last = sync_button;
154   reset_button_last = reset_button;

156   newData = 1;
    }
```

```
158
  // button logic
160 // reset ends any phase
  if (reset_button){
162   if(initial_growth || auto_step){
      initial_growth = 0;
164   auto_step = 0;
      waiting = 1;
166   }
  }
168 // sync starts initial growth if not grown
  if (sync_button && waiting){
170   if(!grown){
      grown = 1;
172   initial_growth = 1;
      last_step_time = micros();
174   step_start_encoder = reelEncPos;
      p_cntrl_set = MIN_P_CNTRL;
176   waiting = 0;
    }
178 // sync starts auto_step if already grown and not started already
    else if(!auto_step){
180   auto_step = 1;
      p_cntrl_set = previous_phase_pressure;
182 //    p_cntrl_set = MIN_P_CNTRL + P_STEP;
      last_step_time = micros();
184   step_start_encoder = reelEncPos;
      waiting = 0;
186   }

188 }

190 // step time logic
```

```
  if (micros() - last_step_time > STEP_TIME && !waiting){
192       // check to see if grown
//        Serial.println("Step time!");
194       if (reelEncPos < step_start_encoder - MOVEMENT_THRESH){
            // if in initial growth phase, keep growing
196         if(initial_growth){
              last_step_time = micros();
198           step_start_encoder = reelEncPos;
            }
200         // auto_step -> reset pressure, wait for restart
            if(auto_step){
202             moved = 1;
                step_start_encoder = reelEncPos;
204             last_step_time = micros();
            }
206       }
          // no movement, increase
208       else{
            if (moved){
210           waiting = 1;
              auto_step = 0;
212           previous_phase_pressure = p_cntrl_set;
              p_cntrl_set = MIN_P_CNTRL;
214           moved = 0;
            }
216         else if (p_cntrl_set < MAX_P_CNTRL){
              // Serial.println("INCREASING!");
218           p_cntrl_set += P_STEP;
              last_step_time = micros();
220           step_start_encoder = reelEncPos;
            }
222         // reached max pressure, end experiment
            else {
```

```
224           initial_growth = 0;
              auto_step = 0;
226           waiting = 1;
              p_cntrl_set = MIN_P_CNTRL;
228           sync = 1;
            }
230       }
    }
232
  if (waiting){
234   p_cntrl_set = MIN_P_CNTRL;
  }
236
  if (micros() - last_msg_time > 100) {
238   if (Serial.available() > 0) {
        // read the incoming byte:
240     incomingByte = Serial.read();
        if (incomingByte == '!') sync = 1;
242     if (incomingByte == 'r') sendMsg = 1;
        if (incomingByte == 's') streamData = !streamData;
244     if (incomingByte == 'b') streamBatch = 1;
        if (incomingByte == 'p') p_cntrl_set = MIN_P_CNTRL;
246   }
  }
248
  if (streamData == 1) sendMsg = 1;
250
  if(sync){
252   sync_state = !sync_state;
    digitalWrite(LED_PIN, sync_state);
254 }

256 int batchLimit = 250;
```

```
  if (streamBatch == 1){
258   sendMsg = 1;
  }
260 if (batchCount > batchLimit){
    batchCount = 0;
262   streamBatch = 0;
    batchLabel = 0;
264 }

266 if (sendMsg && newData) {
    last_msg_time = micros();
268   Serial.print(time_now); // time
    Serial.print(" , ");
270   Serial.print(newReelEncPos);  // reel encoder
    Serial.print(" , ");
272   Serial.print(p_cntrl_set);        // pressure controller setting
    Serial.print(" , ");
274   Serial.print(flow_val);        // flow
    Serial.print(" , ");
276   Serial.print(pressure, 4);       // pressure
    Serial.print(" , ");
278   Serial.print(int(sync_state));     // synchronization serial return
    Serial.print(" , ");
280   Serial.print(sync_button);     // go button
    Serial.print(" , ");
282   Serial.println(waiting);     // reset button

284   if(streamBatch) batchCount++;;

286   sendMsg = 0;
    newData = 0;
288   sync = 0;
  }
```

```
290
    sync = 0;
292 }
```

Listing A.2: FrictionExpStates.ino